NAVAL POSTGRADUATE SCHOOL

MONTEREY, CALIFORNIA

THESIS

ANALYSIS OF SFMR-DERIVED AND SATELLITE-BASED RAIN RATES OVER THE TROPICAL WESTERN NORTH PACIFIC

by

Ryan S. Willis

March 2010

Thesis Advisor: Patrick A. Harr
Second Reader: Russell L. Elsberry

Approved for public release; distribution is unlimited

THIS PAGE INTENTIONALLY LEFT BLANK

REPORT DOCUMENTATION PAGE		*Form Approved OMB No. 0704–0188*
Public reporting burden for this collection of information is estimated to average 1 hour per response, including the time for reviewing instruction, searching existing data sources, gathering and maintaining the data needed, and completing and reviewing the collection of information. Send comments regarding this burden estimate or any other aspect of this collection of information, including suggestions for reducing this burden, to Washington headquarters Services, Directorate for Information Operations and Reports, 1215 Jefferson Davis Highway, Suite 1204, Arlington, VA 22202–4302, and to the Office of Management and Budget, Paperwork Reduction Project (0704–0188) Washington DC 20503.		
1. AGENCY USE ONLY *(Leave blank)*	**2. REPORT DATE** March 2012	**3. REPORT TYPE AND DATES COVERED** Master's Thesis
4. TITLE AND SUBTITLE Analysis of SFMR-Derived and Satellite-Based Rain Rates over the Tropical Western North Pacific		**5. FUNDING NUMBERS**
6. AUTHOR(S) Ryan S. Willis		
7. PERFORMING ORGANIZATION NAME(S) AND ADDRESS(ES) Naval Postgraduate School Monterey, CA 93943–5000		**8. PERFORMING ORGANIZATION REPORT NUMBER**
9. SPONSORING /MONITORING AGENCY NAME(S) AND ADDRESS(ES) N/A		**10. SPONSORING/MONITORING AGENCY REPORT NUMBER**
11. SUPPLEMENTARY NOTES The views expressed in this thesis are those of the author and do not reflect the official policy or position of the Department of Defense or the U.S. Government. IRB Protocol Number: N/A		
12a. DISTRIBUTION / AVAILABILITY STATEMENT Approved for public release; distribution is unlimited		**12b. DISTRIBUTION CODE** A

13. ABSTRACT (maximum 200 words)

Aircraft-derived rain rates are obtained from the Stepped Frequency Microwave Radiometer (SFMR) operated on WC-130J in tropical cyclones over the western North Pacific during the Tropical Cyclone Structure 2008 (TCS-08) program and the Impact of Typhoons on the Ocean in the Pacific (ITOP) 2010 program. Rain rates from SFMR are compared to rain rates from the Advanced Microwave Scanning Radiometer–EOS (ASMR-E) and the Tropical Rainfall Measuring Mission (TRMM) satellites when the passes occurred within plus-or-minus three hours of the aircraft times. The relative frequency distributions of SFMR-derived rain rates matched the distribution of AMSR-E rain rates over low- to medium rain rates. However, rain rates over 10 mm h^{-1} occurred more frequently in the satellite-based values. Because of the difference between SFMR and AMSR-E rain rates over medium intensities, the two rain rate distributions are found to be statistically different. Similar differences were found in comparisons between SFMR and the TRMM Microwave Imager (TMI)-based rain rates, and in comparisons between TMI and AMSR-E rain rates. Differences between the relative frequencies of rain rates larger than 10 mm h^{-1} resulted in the conclusion that the distributions of SFMR and TMI frequency distributions and AMSR-E and TMI are statistically different.

14. SUBJECT TERMS Tropical Cyclone, Satellite Reconnaissance, Aircraft Reconnaissance, TCS-08, ITOP 2010, Western North Pacific Typhoons, SFMR, AMSR-E, TRMM, Rain Rates		**15. NUMBER OF PAGES** 109
		16. PRICE CODE
17. SECURITY CLASSIFICATION OF REPORT Unclassified	**18. SECURITY CLASSIFICATION OF THIS PAGE** Unclassified	**19. SECURITY CLASSIFICATION OF ABSTRACT** Unclassified	**20. LIMITATION OF ABSTRACT** UU

NSN 7540–01–280–5500

Standard Form 298 (Rev. 2–89) Prescribed by ANSI Std. 239–18

i

THIS PAGE INTENTIONALLY LEFT BLANK

ANALYSIS OF SFMR-DERIVED AND SATELLITE-BASED RAIN RATES OVER THE TROPICAL WESTERN NORTH PACIFIC

Ryan S. Willis
Captain, United States Air Force
B.S., University of Oklahoma, 2005

Submitted in partial fulfillment of the
requirements for the degree of

MASTER OF SCIENCE IN METEOROLOGY

from the

**NAVAL POSTGRADUATE SCHOOL
March 2012**

Author: Ryan S. Willis

Approved by: Patrick A. Harr
Thesis Advisor

Russell L. Elsberry
Second Reader

Wendell Nuss
Chair, Department of Meteorology

THIS PAGE INTENTIONALLY LEFT BLANK

ABSTRACT

Aircraft-derived rain rates are obtained from the Stepped Frequency Microwave Radiometer (SFMR) operated on WC-130J in tropical cyclones over the western North Pacific during the Tropical Cyclone Structure 2008 (TCS-08) program and the Impact of Typhoons on the Ocean in the Pacific (ITOP) 2010 program. Rain rates from SFMR are compared to rain rates from the Advanced Microwave Scanning Radiometer–EOS (ASMR-E) and the Tropical Rainfall Measuring Mission (TRMM) satellites when the passes occurred within plus-or-minus three hours of the aircraft times. The relative frequency distributions of SFMR-derived rain rates matched the distribution of AMSR-E rain rates over low- to medium rain rates. However, rain rates over 10 mm h^{-1} occurred more frequently in the satellite-based values. Because of the difference between SFMR and AMSR-E rain rates over medium intensities, the two rain rate distributions are found to be statistically different. Similar differences were found in comparisons between SFMR and the TRMM Microwave Imager (TMI)-based rain rates, and in comparisons between TMI and AMSR-E rain rates. Differences between the relative frequencies of rain rates larger than 10 mm h^{-1} resulted in the conclusion that the distributions of SFMR and TMI frequency distributions and AMSR-E and TMI are statistically different.

THIS PAGE INTENTIONALLY LEFT BLANK

TABLE OF CONTENTS

LIST OF FIGURES

x

LIST OF TABLES

THIS PAGE INTENTIONALLY LEFT BLANK

LIST OF ACRONYMS AND ABBREVIATIONS

AMSR-E:	Advanced Microwave Scanning Radiometer - EOS
AOR:	Area of Responsibility
CPHC:	Central Pacific Hurricane Center
DoD:	Department of Defense
EOL:	Earth Observing Laboratory
EOS:	Earth Observing Systems
GPROF:	Goddard Profiling
GPS:	Global Positioning System
ITOP:	Impact of Typhoons on the Ocean in the Pacific
JAXA:	Japanese Aerospace Exploration Agency
JTWC:	Joint Typhoon Warning Center
K-S:	Kolmogorow-Smirnov
NASA:	National Aeronautics and Space Administration
NCAR:	National Center of Atmospheric Research
NCEP:	National Center for Environmental Prediction
NHC:	National Hurricane Center
NMFC:	Naval Maritime Forecast Center
NOAA:	National Oceanic and Atmospheric Association
NRL:	Naval Research Laboratory
PR:	Precipitation Radar
Q-Q:	Quantile-Quantile
SFMR:	Stepped Frequency Microwave Radiometer
SSM/I:	Special Sensor Microwave Imager
T-PARC:	THORPEX-Pacific Asian Regional Campaign
TC:	Tropical Cyclone
TCS-08:	Tropical Cyclone Structure 2008
TMI:	TRMM Microwave Imager
TPC / NHC:	Tropical Prediction Center / National Hurricane Center
TRMM:	Tropical Rainfall Measuring Mission
USAF:	U.S. Air Force

THIS PAGE INTENTIONALLY LEFT BLANK

ACKNOWLEDGMENTS

First and foremost, praises to my Heavenly Father for giving me the strength, knowledge, patience, and perseverance to remain strong through this gigantic endeavor in my life. Without His love and blessings, this life and assignment would be nothing.

To my parents, Jim and Jan, thank you for your support and encouragement throughout this assignment. My life and my career is a direct measurement of the skill-sets you taught me. You were behind me and had my back no matter what came my way. I love you both! To my sister, Caleta, I give you thanks and appreciation for constantly showing your love and support during these dark times. You are a tremendous blessing in my life, and I thank God that you are my little sis. I love ya!!

I would like to thank my thesis advisor, Dr. Patrick Harr, for his guidance, encouragement, and patience in this project. Without your wisdom and technical expertise, this project would not have gotten off the ground. To Dr. Russell Elsberry, thank you for the help in editing and suggestions for this project.

A special thanks to Dr. Pete Black, Andy Penny, and Kurt Nielsen. Without all of your skills and meteorological knowledge, this project (currently and in the future) would not have been possible. Thank you for all the help and work that you've done with me.

Finally, to my NPS professors and fellow classmates, thank you for your support, meteorological knowledge, and peer expertise to further not only my life, but yours as well.

THIS PAGE INTENTIONALLY LEFT BLANK

I. INTRODUCTION

A. MOTIVATION

Tropical cyclones (TC) are severe weather phenomena that occur throughout many oceanic regions and often impact shore- and land-based assets. To the general public, TCs can disrupt normal, daily routines because of their high wind speeds, heavy rainfall, localized flooding, and even the possibility of tornadic activity. These conditions usually persist from one or more days, depending on the TC location and translation speed. Tropical cyclones also impact military operations across the globe. Due to the vertical and horizontal scale of a TC (Figure 1), a wide variety of military activities are affected. Therefore, being able to forecast the intensity, path, and translation speed of a TC is an extremely important part of weather support to military operations.

The National Hurricane Center (NHC) and the Central Pacific Hurricane Center (CPHC) are units of the National Centers for Environmental Prediction (NCEP) that operate under the authority of the National Oceanic and Atmospheric Association (NOAA). The primary mission of the NHC is to save lives, mitigate property loss, and improve economic efficiency by issuing the best watches, warnings, forecasts, and analyses of hazardous tropical weather and by increasing understanding of these hazards (NHC 2011). The NHC area of responsibility (AOR) for tropical weather covers the North Atlantic, Gulf of Mexico, the Caribbean Sea, as well as the eastern North Pacific to 140° W. The CPHC primary mission is the same as the NHC, and their AOR covers the region from the Equator to 30° N and between 140° W and 180° E.

The Joint Typhoon Warning Center (JTWC) area of responsibility covers the western Pacific and Indian oceans. It is a jointly manned U.S. Air Force/Navy organization under the operational command of the Commanding Officer, Naval Maritime Forecast Center (NMFC), Pearl Harbor, Hawaii (JTWC 2010). The JTWC primary mission is very similar to the NHC. However, JTWC is primarily concerned with Department of Defense (DoD) assets throughout their area of responsibility. Unlike

the NHC, there is no operational aircraft reconnaissance program to gather in situ measurements of TC location and intensity within the JTWC area of responsibility (Havel 2009).
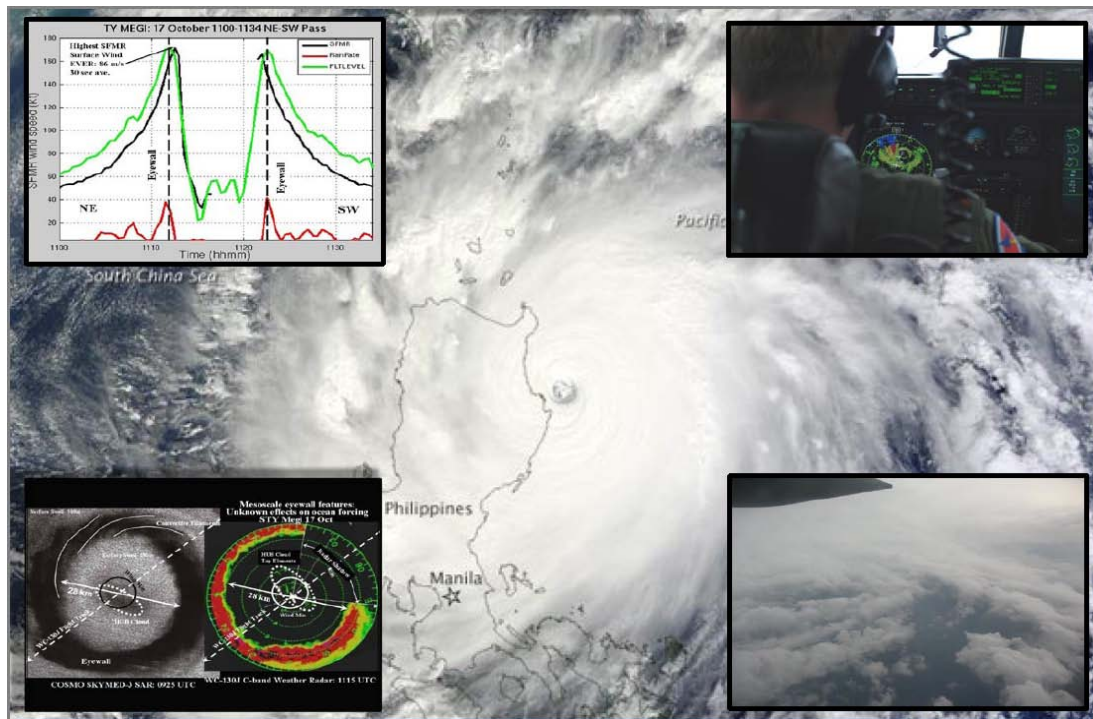
Figure 1.   MODIS 1 km visible image of Typhoon Megi on 10 Oct 2010 (Courtesy of NASA Earth Observatory website). Inset images provided by Dr. Peter Black, NRL Monterey (top left and lower left), Richard Ballucanag (top right), and Matthew Kucas (lower right).

Utilizing a wide range of remote sensing platforms and numerical weather prediction models, operational centers such as NHC and JTWC produce real-time TC analysis and forecasts of TC track and intensity. Because of the lack of an aircraft reconnaissance over the JTWC AOR, satellite observing platforms are the primary source of reconnaissance observations. These platforms have been operational for many years and newer technologies have been built upon algorithms and research that have been developed in recent years. Many algorithms have been developed and tested over the Atlantic basin where aircraft reconnaissance data provide observations for verification of

satellite-based measurements. However, recent field programs conducted over the western North Pacific have provided an opportunity to examine satellite- and aircraft-based observations of TC characteristics in the Pacific Ocean basin.

In this project, aircraft-derived rain rates are examined in relation to satellite-based rain rates. The aircraft observations were obtained during the THORPEX-Pacific Asian Regional Campaign/Tropical Cyclone Structure-08 (T-PARC/TCS-08) and the Impact of Typhoons on the Ocean in the Pacific (ITOP) 2010 programs. An additional goal of this project is to verify algorithms used to define rain rates measured by aircraft.

The instruments onboard the aircraft and the remote-sensing platforms are described in Chapter II. The results of the comparisons between each data source are presented in Chapter III. In addition, several comparisons are made between remote-sensing algorithms and measuring techniques.

B.   BACKGROUND INFORMATION

A number of previous studies have shown that certain atmospheric parameters (i.e., surface winds, rain rates) measured by aircraft instruments can be used to significantly improve the accuracy and forecast of TCs within the Atlantic basin (Uhlhorn et al. 2007). However, few studies have been conducted to examine these same atmospheric parameters over the tropical western North Pacific.

C.   FIELD CAMPAIGNS

The observations used in this study were gathered by the U.S. Air Force (USAF) 53rd Weather Reconnaissance Squadron (Hurricane Hunters) WC-130Js over the western North Pacific during two deployments in support of the T-PARC/TCS-08 and ITOP 2010 field experiments. Both field campaigns utilized a multitude of aircraft assets, including the Naval Research Laboratory (NRL) WP-3. These aircraft carried a large array of onboard instruments, which included the Stepped Frequency Microwave Radiometer (SFMR), which is the primary aircraft-based instrument to be examined in this project. Further information concerning this platform will be provided in Chapter II.

1.   T-PARC/TCS-08

The T-PARC/TCS-08 was part of a multinational field campaign that was designed to examine the entire life cycle of TCs over the western North Pacific to better understand and predict tropical cyclones from formation, intensification, and structure change (Elsberry and Harr 2008). The T-PARC/TCS-08 campaign was conducted from late July through early October 2008. During the T-PARC/TCS-08 campaign, scientists and technicians monitored and tracked multiple TCs throughout the western North Pacific. Four storms that occurred during the T-PARC/TCS-08 field programs were selected for this study (Table 1).

Table 1.   Named storms in which data were collected during T-PARC/TCS-08 campaigns. The storm number and dates of first and last warning issued are based on the JTWC best-track data (From JTWC 2008).

TCS - 08			
Storm Name	**Storm Number**	**Date of First Warning Issued**	**Date of Last Warning Issued**
TY Nuri	13W	16 Aug 2008	22 Aug 2008
TY Sinlaku	15W	08 Sep 2008	20 Sep 2008
TY Hagupit	18W	17 Sep 2008	24 Sep 2008
TY Jangmi	19W	23 Sep 2008	30 Sep 2008

2.   ITOP 2010

The ITOP 2010 experiment addressed the ocean response to typhoons in the western North Pacific Ocean and specific scientific questions concerning the formation/dissipation of TCs, ocean/atmospheric boundary layer interactions, and typhoon forecasting techniques (Pun et al. 2011). Two WC-130J aircraft were operated during ITOP 2010. The field campaign was conducted from early August through late

October. As with T-PARC/TCS-08, a number of TCs were tracked and studied throughout the western North Pacific. Three storms were selected for this study (Table 2).

Table 2.   Named storms in which data were collected during ITOP 2010. Storm number and data of first and last warnings are from the JTWC best-track data (From JTWC 2010).

ITOP 2010			
Storm Name	**Storm Number**	**Date of First Warning Issued**	**Date of Last Warning Issued**
TY Fanapi	12W	14 Sep 2010	20 Sep 2010
TY Malakas	13W	19 Sep 2010	25 Sep 2010
TY Megi	15W	12 Oct 2010	23 Oct 2010

D.   DOD BENEFITS

This study seeks to examine whether remotely-sensed rain rates from the SFMR and space-based platforms can produce improved TC-related rain rate detection for military significant areas (e.g., Japan, Korea, and the Philippines). Additionally, comparisons between aircraft- and satellite-based rain rates will be used to validate each measurement system. Validation of remotely-sensed rain rates will allow for improved analyses of TC structure.

THIS PAGE INTENTIONALLY LEFT BLANK

II. METHODOLOGY

A. OBSERVING SYSTEMS

The objective of this thesis is to compare rain rate measurements from the SFMR to known, highly accepted rain rate measurements from space-based, remote-sensing platforms. Because the WC-130J aircraft were operating over the open ocean, no land-based radar systems were available to provide the necessary observations for comparison. Even though the Special Sensor Microwave Imager (SSM/I) has been a proven data source of rain rate measurements, the horizontal resolution is 12.5 km at 85GHz (NRL 2011). Because the SFMR has a spatial resolution of approximately 1.5 km (Jiang et al. 2006), the SSM/I satellite was not used in this study. Rather, rain rate measurements from the Earth Observing Systems (EOS) were chosen as the control precipitation measurements. The Tropical Rainfall Measuring Mission (TRMM) has two rain rate sensors that have a horizontal resolution of 5.0 km (NASA 2011b). The Aqua satellite, which has a single rain rate sensor that has six feedhorns to measure different frequencies, has horizontal resolutions from 5.4 km to 54 km (NASA 2011d).

1. SFMR

The original concept of the SFMR was developed and built in 1978 by the National Aeronautics and Space Administration (NASA) Langley Research Center (Harrington 1980). The development was based on previous studies that had shown passive microwave emissions from the sea surface are strongly correlated with wind speed. The "stepping" procedure that was required for estimating the surface wind speed in hurricanes by correcting for rain-induced effects in the measurements, thus enabling the recovery of rain rates (Uhlhorn and Black 2003). Further research showed that by utilizing a combination of frequencies and new calibration algorithms, more accurate wind speed measurements could be collected during TC flights. These improvements were done in combination with comparisons to Global Positioning System (GPS)

dropwindsonde observations for derivation of the new SFMR algorithms. The improved remote-sensing algorithm provided more accurate ground-truth data (Uhlhorn et al. 2007) for wind speeds and rain rates.

The SFMR observations are available at 1-second, 10-second, and 30-second intervals. To match the horizontal resolutions of the TRMM PR and AMSR-E footprints, information concerning the SFMR beam width, half-power angle, instantaneous illuminated footprint diameter, and aircraft distance traveled is considered (Figure 2). Based on the flight and instrument characteristics, the 30-second data are the best fit for comparison with the 5 km satellite footprints. However, the SFMR spot size is an oval shape rather than circular. Therefore, the width of the SFMR footprint is smaller than the satellite footprint, which may introduce some errors in representation of the spatial region that is being remotely sensed (P. Black 2012, personal communication).

The SFMR datasets were quality-controlled at the Naval Postgraduate School and archived at the National Center of Atmospheric Research (NCAR) Earth Observing Laboratory (EOL). As part of the SFMR database, quality-control flags are assigned to define data that meet accuracy parameters for inclusion for further analysis.

d = H*tan(𝒜/2)   𝒜 = beamwidth, i.e. 24 deg, H = RA, radar altitude, i.e. 3-, 10-km

L = GS*tbar   L = distance plane travels in averaging time, tbar; GS = aircraft ground speed

𝓁 = L + 2d   𝓁 = total along track illumination distance
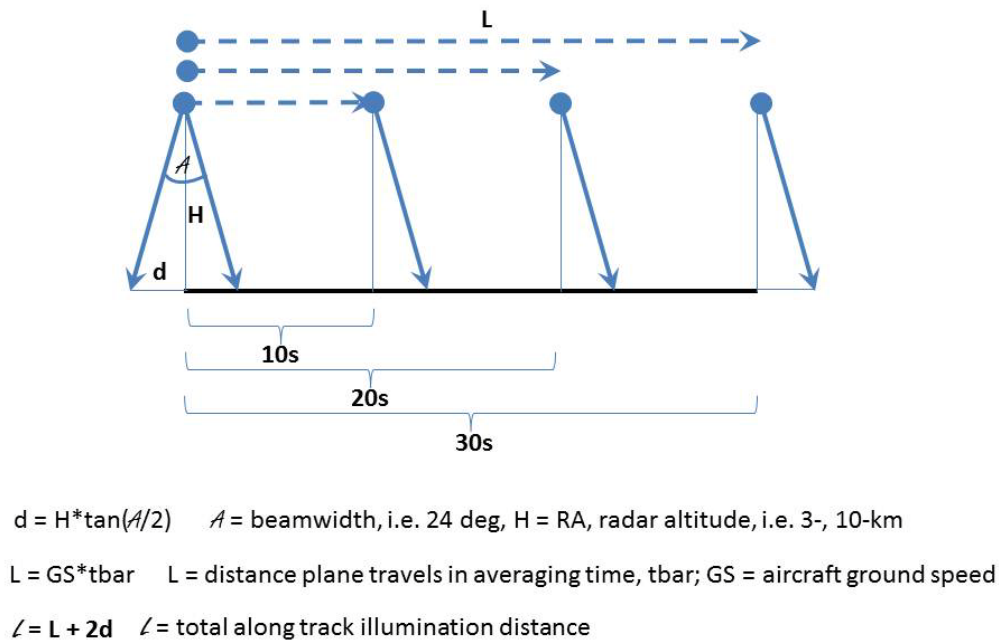
Figure 2.   Footprint geometry for the SFMR (From P. Black 2012, personal communication).

The surface wind measurements from the SFMR are used to define the current intensity of the storm (Figure 3). In operational deployments over the North Atlantic, the data are transmitted to the Tropical Prediction Center/National Hurricane Center (TPC/NHC). The agencies use the data to help forecast the storm track and intensity. Additionally, SFMR-derived rain rates provide some details on storm structure (Figure 3).
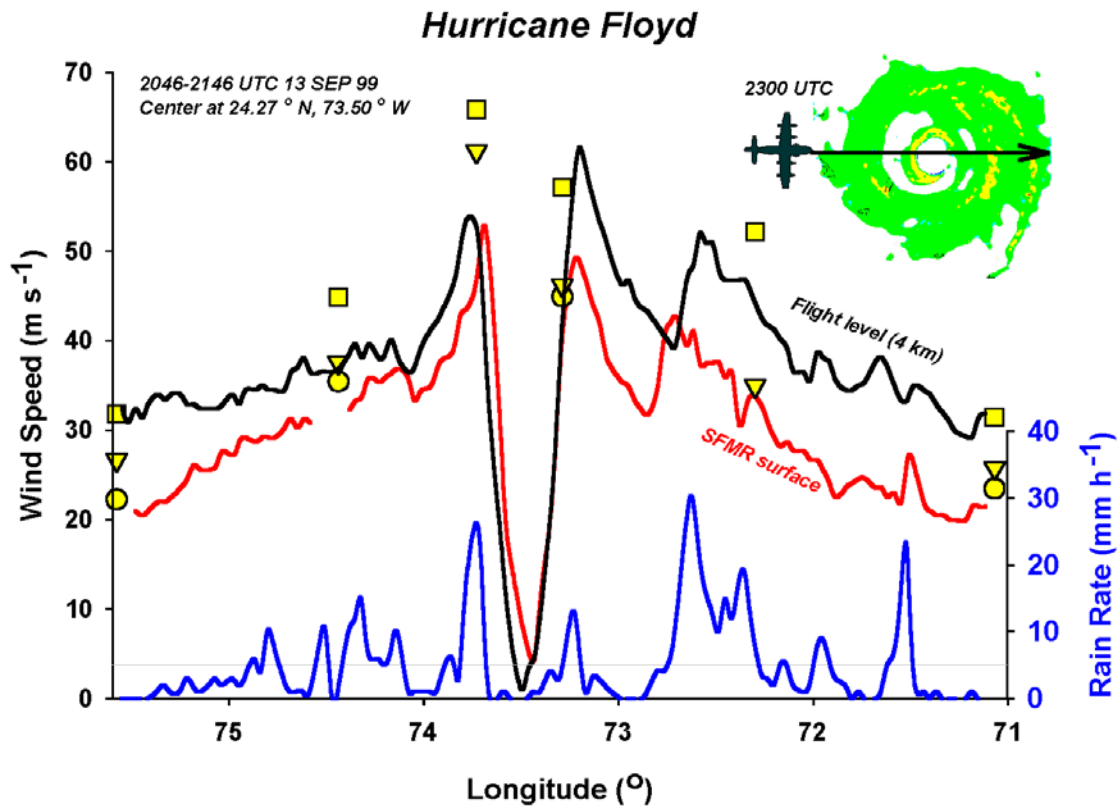
Figure 3.   Surface wind speed (m s^{-1}, red line) as measured by the SFMR during a west-to-east pass across Hurricane Floyd (1999) when it was a Category 4 hurricane east of Miami. The wind speeds (m s^{-1}) at flight level are defined by the black line and the SFMR-measured surface rain rate (mm h^{-1}) is given by the blue line. The yellow markers are dropwindsonde wind speeds (m s^{-1}) from flight level down to the surface. (Image available from http://www.aoml.noaa.gov/hrd/floyd_sfmr.html)

2.   TRMM

The TRMM satellite was launched into orbit in 1997 and its ongoing mission objective is to measure precipitation over the tropical and subtropical regions of the atmosphere. The satellite utilizes multiple sensors to gather information from the atmosphere. The TRMM Microwave Imager (TMI) and the Precipitation Radar (PR) provide precipitation measurements.

a.   TMI

The TMI sensor was built on the same technology in the SSM/I precipitation measurement capabilities. However, many improvements were made to allow for a higher spatial resolution and better quality data to be calculated. One note of interest is that the TMI additionally measures the 10.7 GHz channel, which provides a more linear response for the high rain rates common in tropical rainfall (NASA 2011a). The TMI sensor has a circular horizontal resolution of 5.1 km at 85.5 GHz with a swath path of 878 km (NASA 2011b) (Figures 4 and 5). Although the resolution is much higher than the SSM/I, the TMI is based upon the same technology as the SSM/I. The TMI utilizes microwave radiation readings, brightness temperatures, and input from other sensors to calculate the precipitation measurements.

b.   PR

The PR sensor was hailed as the first spaceborne instrument designed to provide three-dimensional maps of storm structure (NASA 2011c). The TRMM PR is an active phased-array radar that scans and receives data through direct precipitation measurements. It utilizes known rain rate detection from previous research with the already existent land-based radar network. However, because of the sensor being an active radar instrument, it must also account for known errors that are attributed to weather radar detection. These errors can include rain attenuation (Olsen et al. 1978), nonuniform beam filling (Durden et al. 1998), and the necessary information to properly encode the algorithms needed to calculate the required data (Iguchi et al. 2000). However, because of the known properties of rain rate detection from radar through drop

size distribution and Z-R relationships (Jorgensen and Willis 1982), it can provide measurements at a high vertical resolution. The PR sensor has a circular horizontal resolution of 5.0 km (Figure 4) and a swath width of 247 km (NASA 2011b) (Figures 4 and 5). Even though the TMI and PR have the same horizontal resolution, it appears the PR sensor has an advantage as it directly senses the precipitation measurements, which is why the PR sensor was chosen for use in this thesis project.
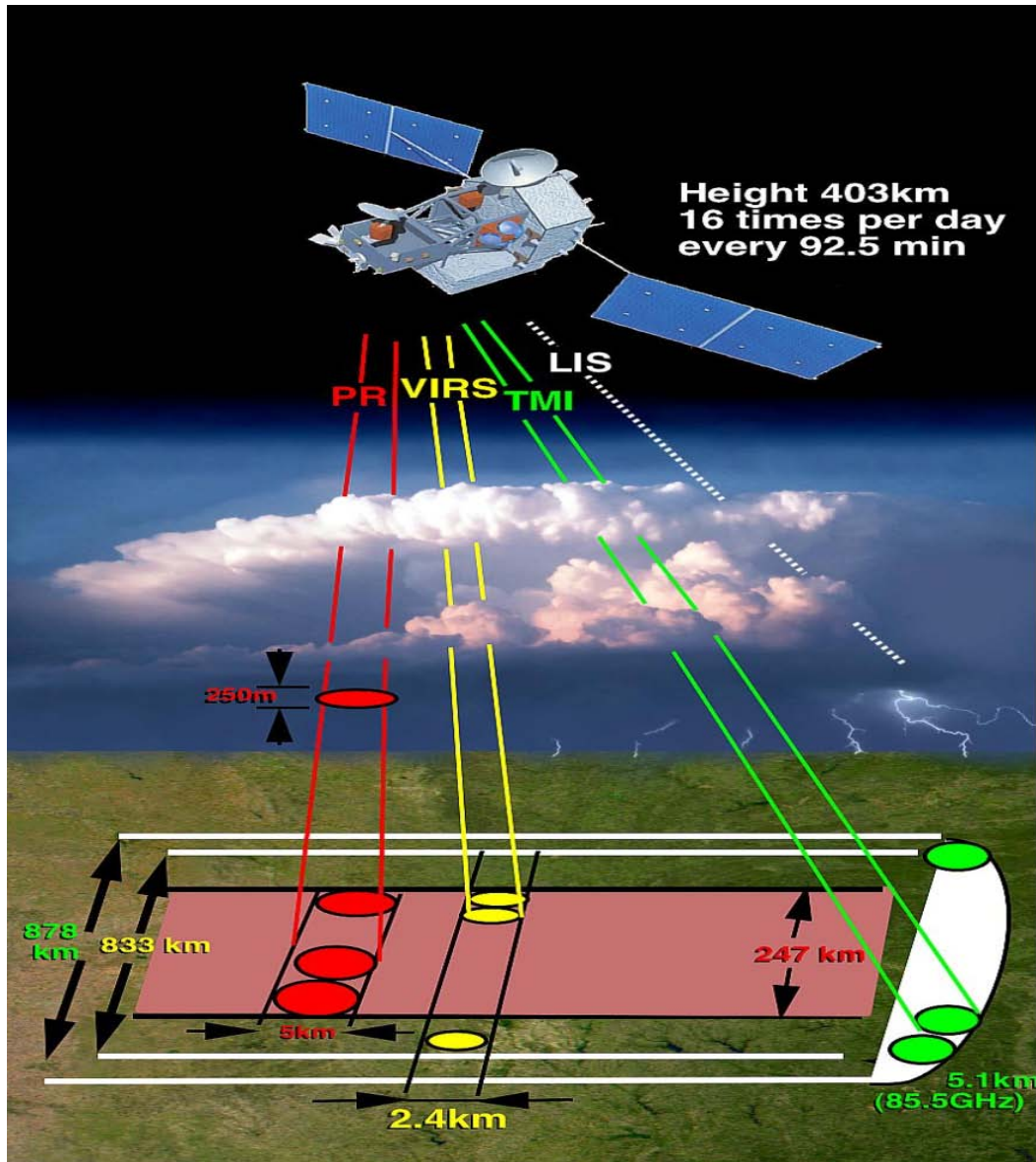
Figure 4.   Overview of the TRMM instrument package spatial coverage. The TMI sensor coverage is shown in green, while the PR sensor coverage is shown in red. (Image available from http://trmm.gsfc.nasa.gov/overview_dir/background.html)
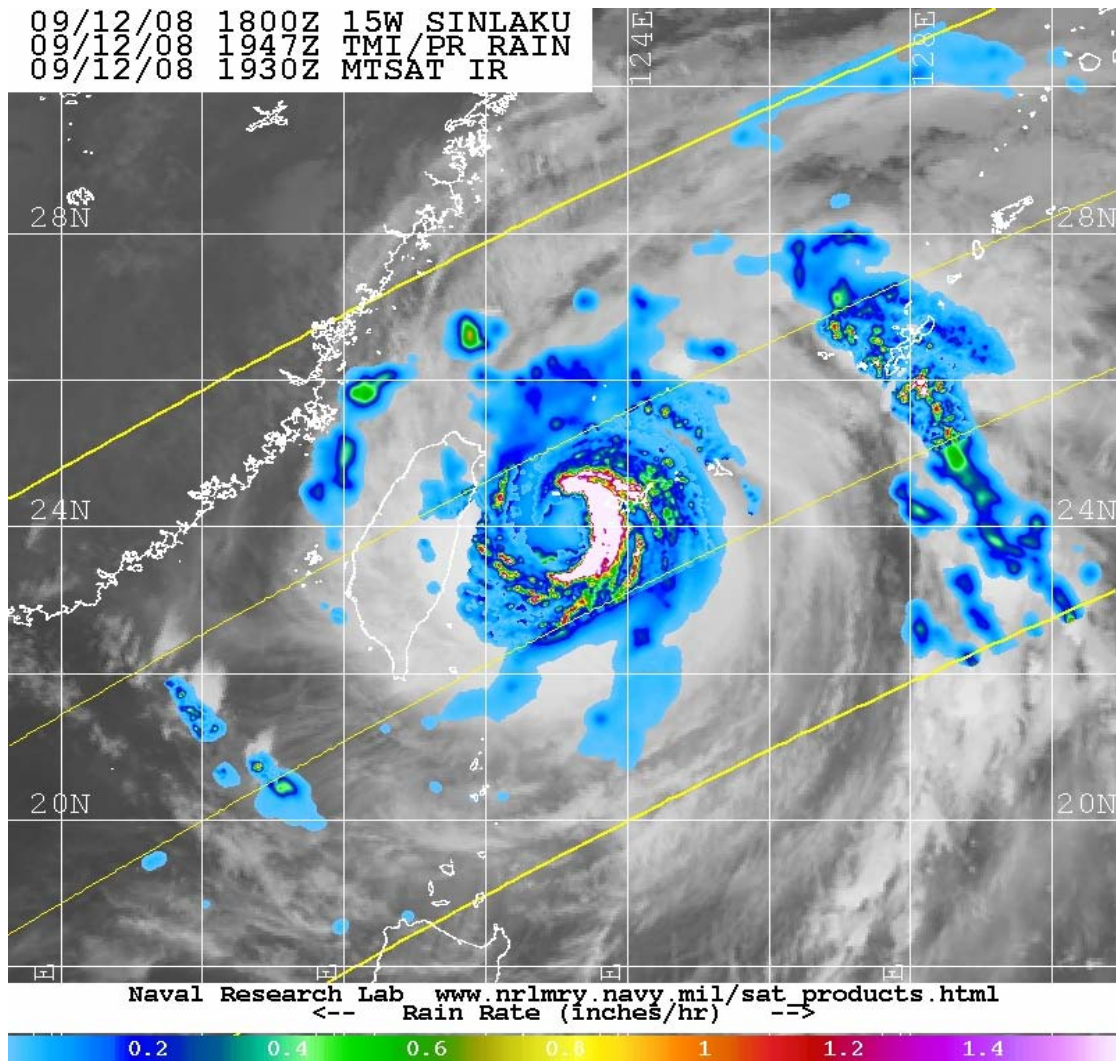
Figure 5.   A TRMM TMI and PR rain rate (mm h^{-1}) pass over TY Sinlaku at 1947 UTC 12 Sep 2008. Note the wider swath is for the TMI and the smaller swath is for the PR data (Image available from http://www.nrlmry.navy.mil/TC.html).

c.   TRMM Database

The TRMM PR data were obtained from a web-based data archive as described in Jiang et al. (2011). The database contains TRMM PR data binned into six geographic regions and includes the entire lifetime of the TRMM satellite. Within each region and year, the Jiang et al. database contains a listing of all named tropical cyclones and has all TRMM passes that occurred for a particular tropical cyclone. A valuable

aspect of this TRMM data base is that extensive quality control measures had been applied. All TRMM passes that corresponded to the named storms in Tables 1 and 2 were accessed for this analysis.

3. Aqua

The Aqua satellite was launched in 2002 with an objective to collect information on the Earth water cycle. Specific parameters include evaporation from the oceans, water vapor in the atmosphere, clouds, precipitation, soil moisture, sea ice, land ice, and snow cover on the land and ice (NASA 2011d).

a. AMSR-E

The primary instrument that measures precipitation is the Advanced Microwave Scanning Radiometer–EOS (AMSR-E). The AMSR-E is a passive microwave radiometer that operates on the same premise as the TMI to remotely sense brightness temperatures at different frequencies. The AMSR-E has horizontal and vertical polarizations for all frequencies. As with other passive microwave sensors, the AMSR-E utilizes the Goddard Profiling (GPROF) algorithm to retrieve rain rate measurements based on the different frequencies. Since the TMI also utilizes this algorithm, this allows for an equivalent comparison for each sensor. However, the AMSR-E has a global coverage similar to the SSM/I (Wilheit et al. 2003), which means the AMSR-E has a more robust spatial coverage than the TMI. The AMSE-E sensor has an oval-shaped footprint of 4.5 km by 6 km at 89 GHz (Figure 6) with a swath width of 1445 km (JAXA 2011) (Figure 7), which is larger than the swath of the TMI. Therefore, this thesis uses the AMSR-E data as the second choice for rain rate measurements.
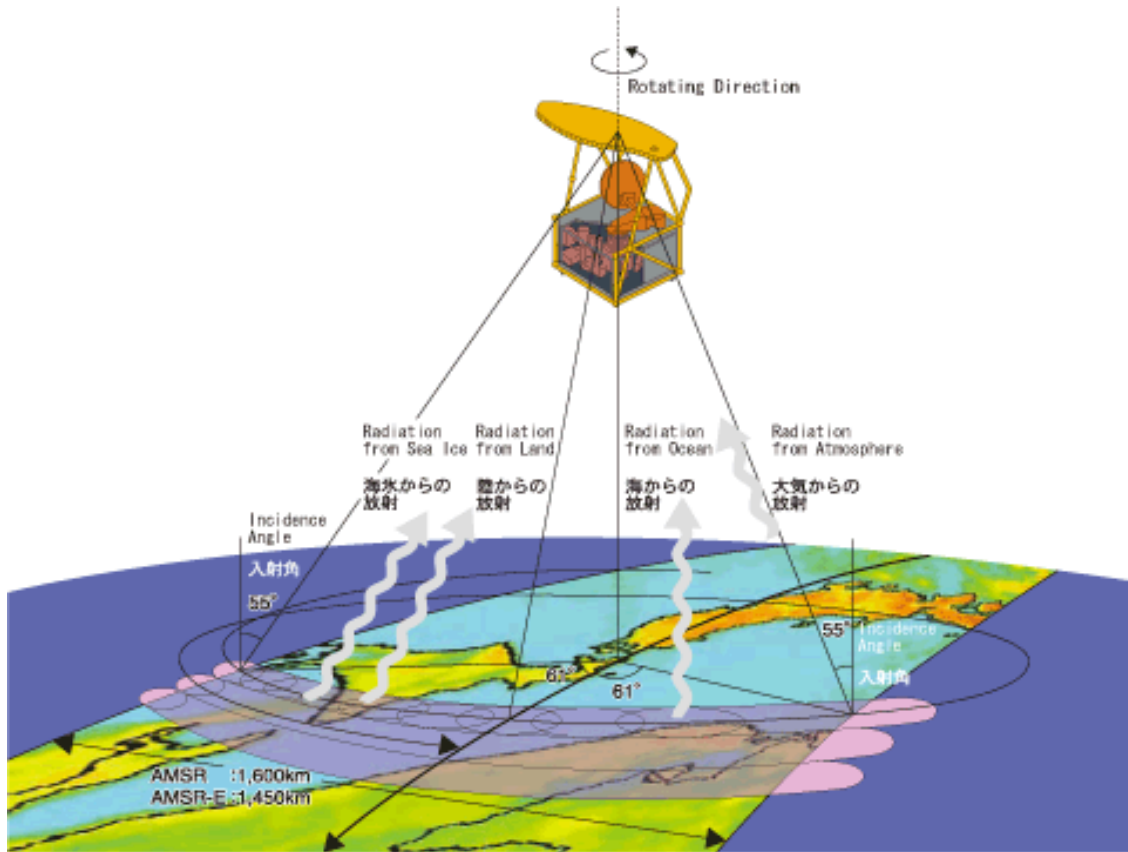
Figure 6.　　　Overview of the AMSR-E instrument spatial coverage (JAXA 2011).

b.　　AMSR-E Database

The source for AMSR-E data was the Japanese Aerospace Exploration Agency (JAXA) AMSR-E Typhoon Database (JAXA 2012). The database is structured similar to the TRMM database (i.e., region, year, named storm). Rather than having all products available in one data file, the precipitation measurements were placed in a separate data file. Unlike the TRMM data, the AMSRE-E data were not extensively quality controlled for missing data so this task was required before inclusion in the analysis. All AMSR-E passes that corresponded to the named storms in Tables 1 and 2 were available for analysis.

14
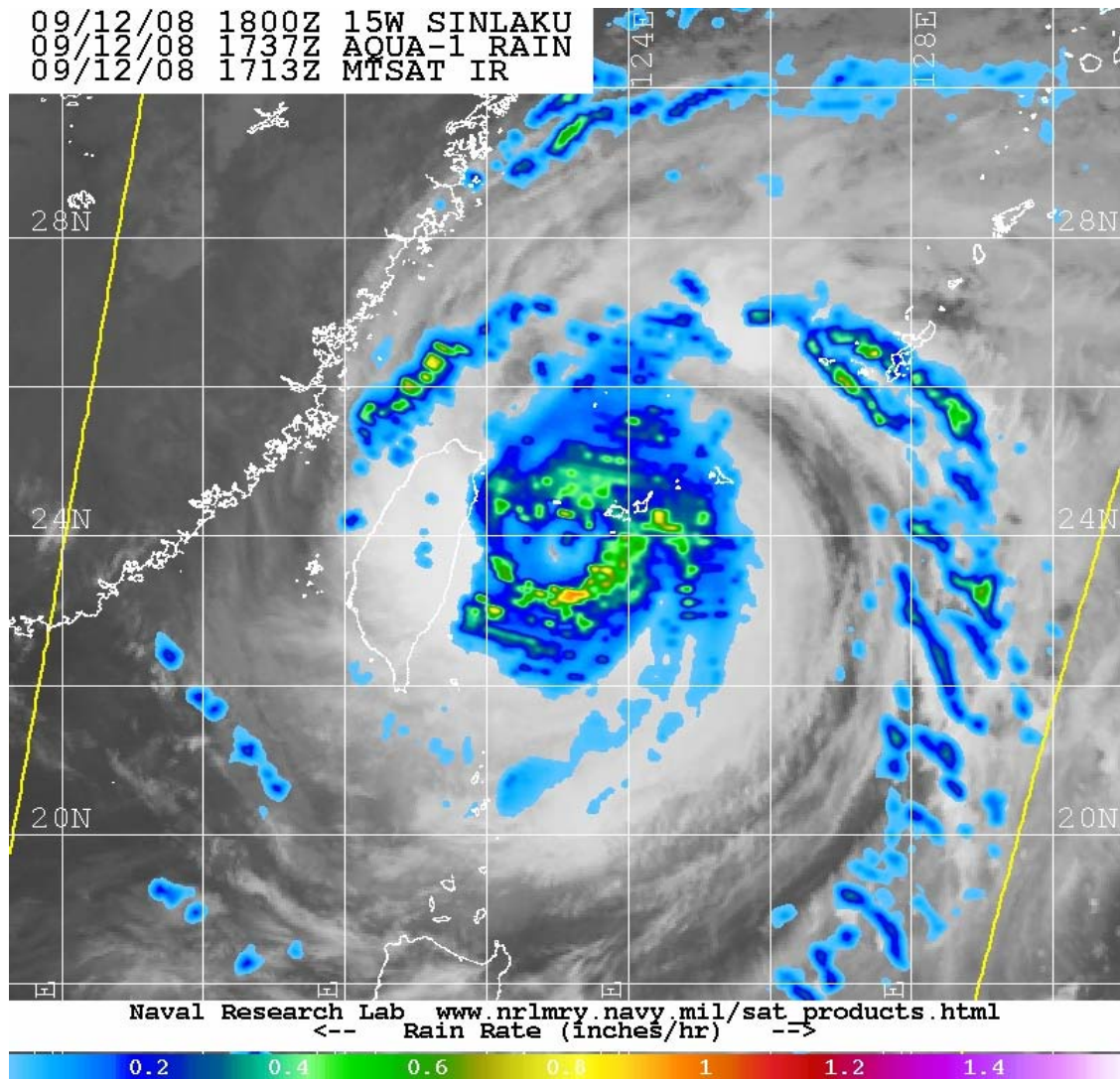
Figure 7.   An AMSR-E rain rate (mm h^{-1}) pass over TY Sinlaku at 1737 UTC
        12 Sep 2008 (Image available from http://www.nrlmry.navy.mil/TC.html).

B.   DATA MATCHING EACH SENSOR

Date and times of all satellite data were matched to identify those passes that were in close temporal proximity to SFMR data obtained during aircraft missions. To be selected, a satellite pass had to be within plus or minus three hours of the entire flight time. Although the generous three-hour window provided for a larger number of eligible satellite passes, it was not always representative of the conditions that may have been encountered by the aircraft. Therefore, a plus-or-minus one-hour window was also used

to define representative cases. If the satellite pass was within the flight period and matched the three-hour grace period, it was considered as a candidate for this project (Figures 8 and 9).
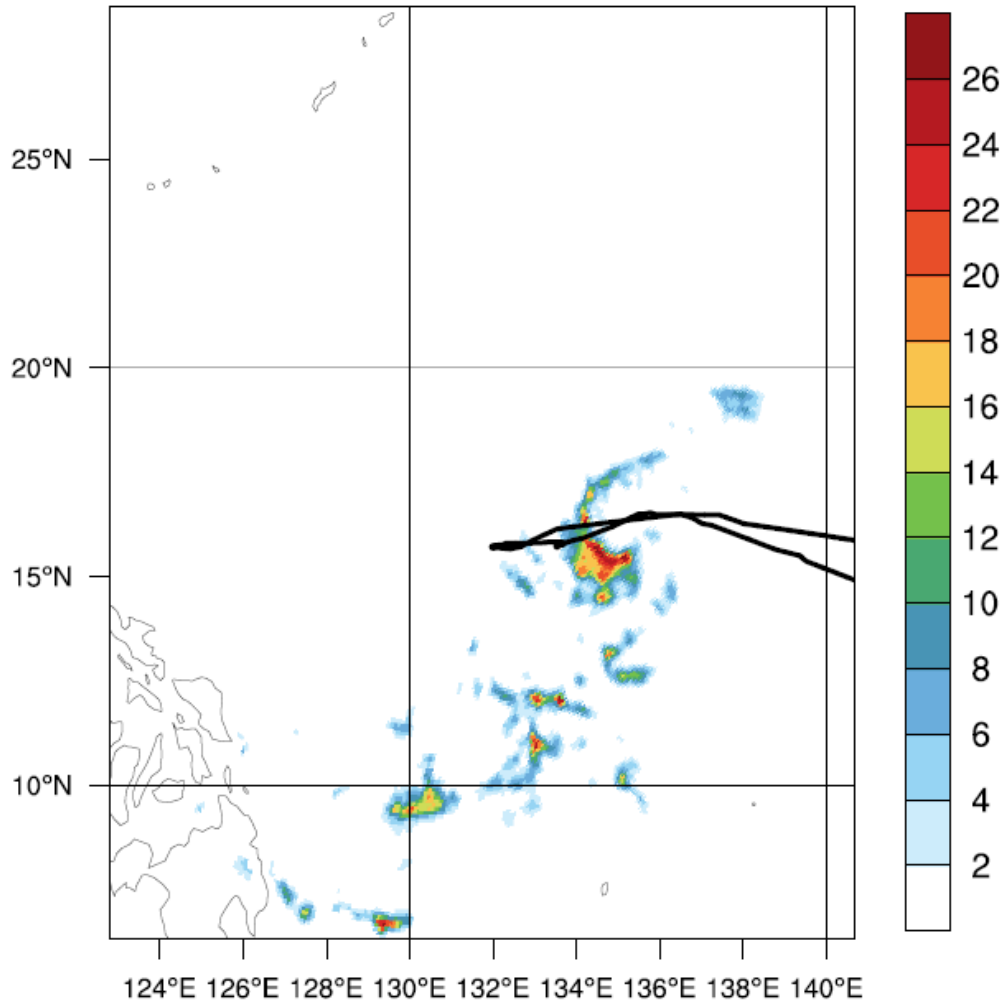
Figure 8.   An AMSR-E pass of TY Sinlaku precipitation rate (mm h^{-1}) at 1659 UTC 17 Aug 2008 with WC-130J flight path overlaid (black line).
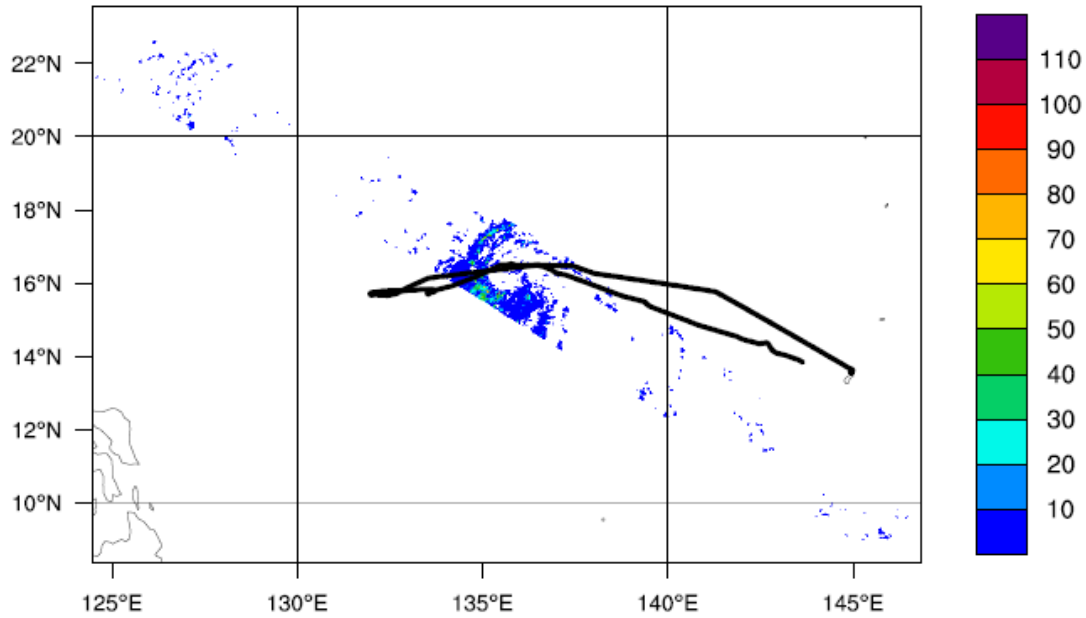
Figure 9.　　A TRMM PR pass of TY Sinlaku precipitation rate (mm h^{-1}) at
1553 UTC 17 Aug 2008 with WC-130J flight path
overlaid (black line).

The next step in this process was to check if the satellite pass went over the same geographical region as the flight path. This was done by overlaying individual flight paths onto the satellite imagery. If the satellite pass did not cross any of the flight paths, it was not considered as a potential candidate and removed from the database. Because of the narrow width of the TRMM PR swatch, few passes were accepted.

C.　　DATA PROCESSING

1.　　Storm-Relative Flight Tracks

To allow similar rain rate features in the satellite data and in the SFMR data to be compared, each data set was referenced to the typhoon center. This adjustment was made by utilizing JTWC best-track coordinates (JTWC 2012) for each event (Figures 10 and 11). Even though the best track is defined on a 6-h interval (00, 06, 12, 18 UTC), the motion of each TC was steady such that the 6-h time resolution was adequate. This storm-relative adjustment ensured the SFMR data were being defined at the same

geographical location as the gridded data from the satellites. To fill any SFMR data gaps and provide smoother rain rates, a three-point weighted running average (0.25, 0.5, 0.25) was applied to the precipitation data.
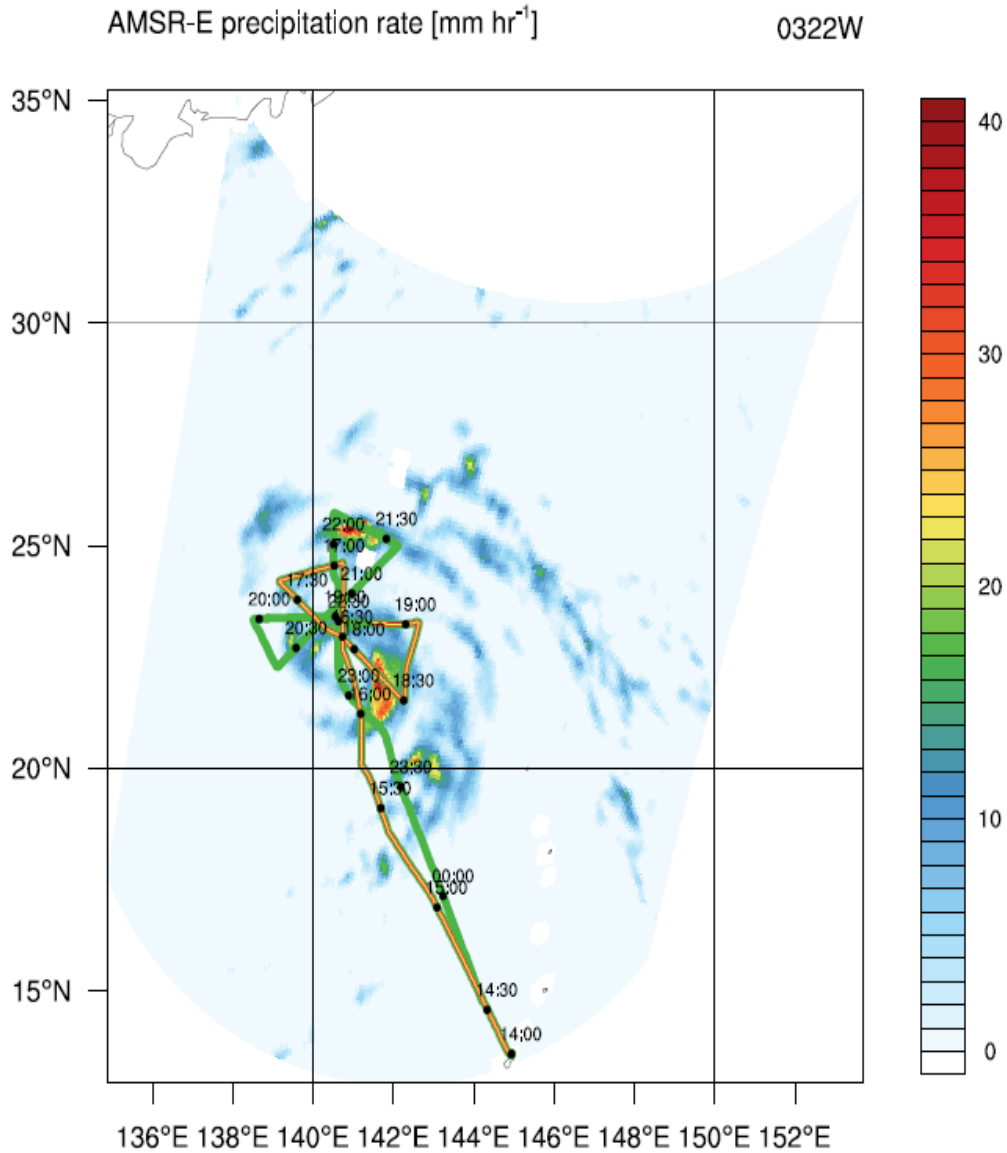
Figure 10.　　　An AMSR-E pass of TY Malakas at 1613 UTC 23 Sep 2010. The WC-130J flight tracks in Earth-relative coordinates are defined by the line. The times (hh:mm) along the track are defined at 30-minute intervals.
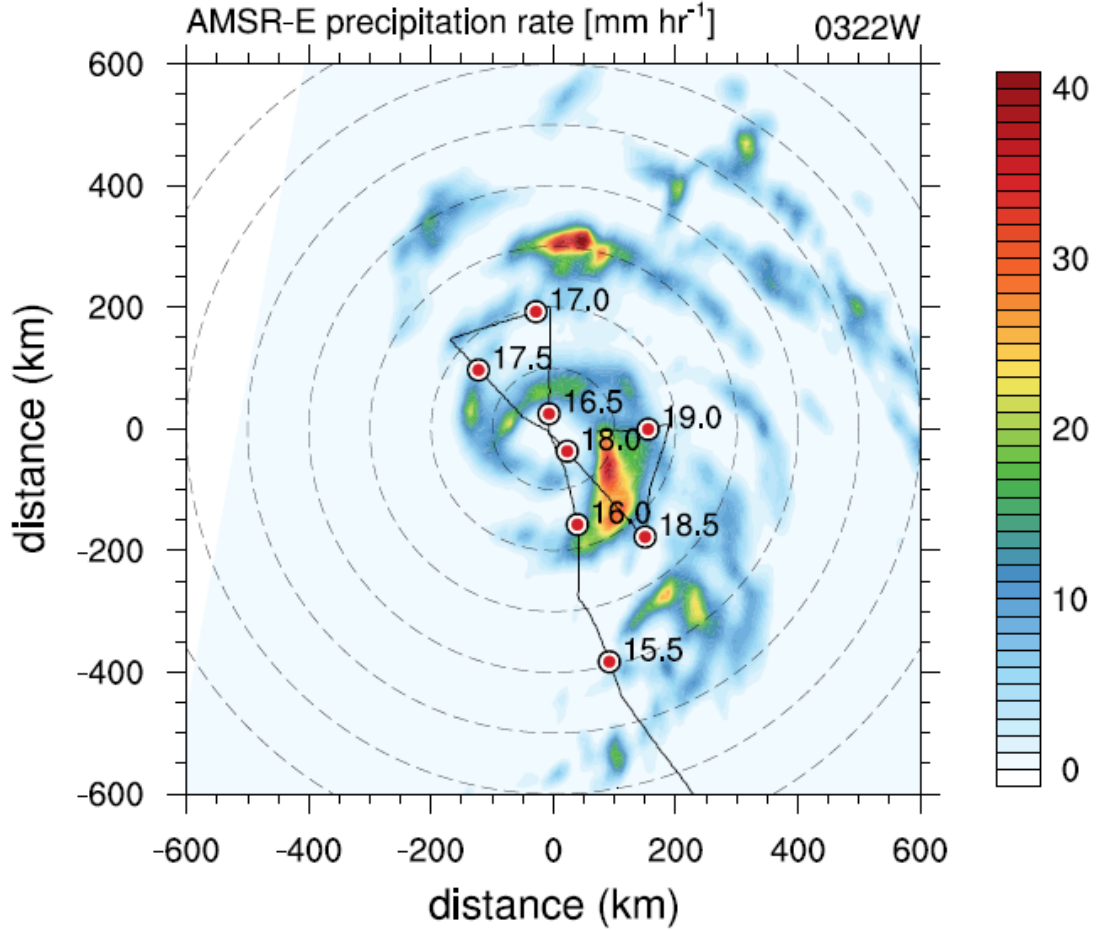
Figure 11.   Same AMSR-E pass as in Figure 10 with the storm-relative flight track included. Only the flight path within the three-hour grace period is displayed, and the times (hh:mm) are indicated.

2.   Spatial Interpolation

To correctly match the SFMR and satellite data, a weighted interpolation scheme was used to fit the satellite precipitation measurements onto the same latitude/longitude points as the storm-relative SFMR precipitation measurements (spatial interpolation). As a result of the interpolation process, precipitation measurements are defined along the WC-130J flight path. However, because the satellite pass does not cover the entire flight path, only regions where actual rain rate data were present from the satellite were incorporated into the interpolation process.

3. Defining a Reference Time

Even though it is possible spatially interpolate all data to a common reference, there is no plausible way to account for the temporal variations. The SFMR collects data both spatially and temporally. Since the satellite pass contains a very short temporal path (~10 minutes), it is considered to be an instantaneous measurement; however, the temporal path for the SFMR rain rates is several hours long. Even though the platforms cannot be interpolated temporally, they can be coordinated with a temporal reference point. The interpolation process ties the satellite data to the SFMR data by the flight path latitude/longitude points. Since the flight path has time markers, a temporal reference can be associated with the interpolated data to ensure both sets of data are the correct data points.

Each case has the reference date set to 0000 UTC on the day the flight originated (i.e., if the flight began at 1735 UTC 23 Sep 2008, the reference date was set to 0000 UTC 23 Sep 2008). The SFMR and satellite data are then referenced based on the number of hours since the reference date and time. To define the correct hours, the flight path times were manually matched to the satellite pass defined to be within the eligible time window of plus-or-minus three-hours or one-hour (Figures 12 and 13).
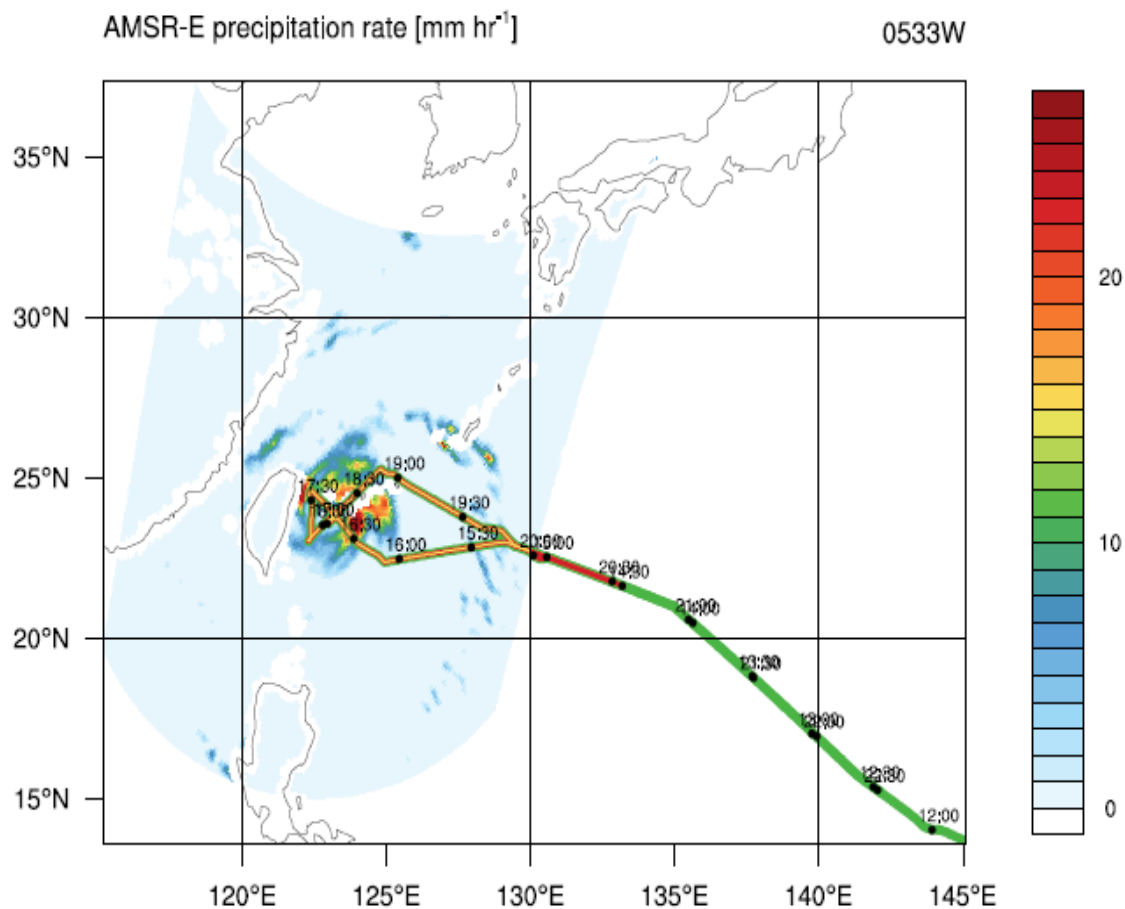
Figure 12.   AMSR-E precipitation rate (mm h^{-1})for the satellite pass at 1734 UTC 12 Sep 2008. The black line represents the entire flight path of a WC-130J mission that began at 1132 UTC 12 Sep 2008 and the red line represents the 3 h grace period for the satellite pass. The yellow line represents the portion of the flight path in which the satellite data are interpolated in space and time to the flight path.

21

Figure 13.   As in Figure 12, except for a TRMM PR precipitation rate (mm h^{-1}) satellite pass at 1944 UTC 12 Sep 2008.

4.   Database Creation

Once the appropriate spatial methodology and reference times were established, other atmospheric variables (Table 3) were also placed in the space-time reference frame. All of these variables were placed into a database for each storm.

Table 3.   List of database variables defined for each case. The values are either the
raw data that is given by the appropriate sensing platform, or it is
interpolated (or averaged).

DATABASE VARIABLES	
VARIABLE NAME	**INTERPOLATED / ACTUAL** **VARIABLE**
SFMR DATE AND TIME	**ACTUAL**
SFMR LATITUDE (DEG N)	**ACTUAL**
SFMR LONGITUDE (DEG E)	**ACTUAL**
SATELLITE PRECIPITATION RATE **(MM HR^{-1})**	**INTERPOLATED**
SFMR PRECIPITATION RATE RAW **(MM HR^{-1})**	**ACTUAL**
SFMR PRECIPITATION RATE AVG **(MM HR^{-1})**	**INTERPOLATED**
DELTA-T (HRS)	**INTERPOLATED**
SFMR SURFACE WINDS (KT)	**ACTUAL**
SFMR GEOPOTENTIAL HEIGHT (M)	**ACTUAL**
SFMR FLIGHT LEVEL WIND **DIRECTION (DEG)**	**ACTUAL**
SFMR FLIGHT LEVEL WIND SPEED **(KT)**	**ACTUAL**
SFMR FLIGHT LEVEL **TEMPERATURE (°C)**	**ACTUAL**
SFMR FLIGHT LEVEL DEW POINT **(°C)**	**ACTUAL**
SFMR FLIGHT LEVEL PRESSURE **(MB)**	**ACTUAL**
SFMR EXTRAPOLATED SURFACE **PRESSURE / D-VALUE (MB / M)**	**ACTUAL**

The database is conditioned upon the physical characteristics of the flight path environment, which is characterized as an inner-core region type if the flight penetrated the eye of the storm (Table 4). If the flight path was mainly in the outer rainbands of the storm and did penetrate the eye of the storm, it was classified as a mixed inner-core region / rainband type (Table 5). If the flight path stayed was entirely in the outer rainbands of the storm, it was classified as a rainband type (Table 6). Finally, the time difference between the time that the WC-130J was in the region and the satellite pass (delta-t), was used to partition the database.

Table 4.   List of named typhoons of inner-core region type observations of SFMR and satellite observations.

INNER CORE REGION TYPE		
STORM NAME W/ DATE AND TIME	DELTA-T	TOTAL HOURS OF DATA
TY SINLAKU 2008–09–09 / 04:54 UTC (AMSR-E)	-2.47 HRS TO 2.97 HRS	5.44 HRS
TY MALAKAS 2010–09–23 / 16:13 UTC (AMSR-E)	-2.02 HRS TO 2.96 HRS	4.98 HRS
TY SINLAKU 2008–09–12 / 17:34 UTC (AMSR-E)	-2.51 HRS TO 2.38 HRS	4.89 HRS
TY JANGMI 2008–09–27 / 04:42 UTC (AMSR-E)	-1.01 HRS TO 2.96 HRS	3.97 HRS
TY FANAPI 2010–09–17 / 04:41 UTC (AMSR-E)	-3.03 HRS TO 0.36 HRS	3.39 HRS

Table 5.   List of named typhoons of mixed inner-core region / rainband type observations of SFMR and satellite observations.

MIXED INNER CORE REGION / RAINBAND TYPE		
STORM NAME W/ DATE AND TIME	DELTA-T	TOTAL HOURS OF DATA
TY MEGI 2010–10–16 / 04:10 UTC (AMSR-E)	-3.03 HRS TO 1.98 HRS	5.01 HRS
TY SINLAKU 2008–09–18 / 04:51 UTC (AMSR-E)	-3.04 HRS TO 0.85 HRS	3.89 HRS
TY MEGI 2010–10–14 / 04:20 UTC (AMSR-E)	-3.02 HRS TO 0.76 HRS	3.78 HRS
TY MEGI 2010–10–17 / 17:05 UTC (AMSR-E)	-3.04 HRS TO 0.22 HRS	3.26 HRS
TY SINLAKU 2008–09–12 / 19:44 UTC (TRMM)	-3.05 HRS TO -0.54 HRS	2.51 HRS

Table 6.   List of named typhoons of rainband type observations of SFMR and satellite observations.

RAINBAND TYPE		
STORM NAME W/ DATE AND TIME	**DELTA-T**	**TOTAL HOURS OF DATA**
TY JANGMI 2008–09–24 / 16:24 UTC (AMSR-E)	**0.80 HRS TO 2.96 HRS**	**2.16 HRS**
TY MALAKAS 2010–09–22 / 03:12 UTC (TRMM)	**-1.28 HRS TO 0.58 HRS**	**1.86 HRS**
TY MEGI 2010–10–17 / 04:53 UTC (AMSR-E)	**-3.03 HRS TO -1.31 HRS**	**1.72 HRS**
TY MEGI 2010–10–13 / 01:42 UTC (TRMM)	**-3.02 HRS TO -2.13 HRS**	**0.89 HRS**
TY MEGI 2010–10–13 / 03:38 UTC (AMSR-E)	**-3.02 HRS TO -2.16 HRS**	**0.86 HRS**
TY SINLAKU 2008–09–17 / 21:40 UTC (TRMM)	**2.18 HRS TO 2.88 HRS**	**0.70 HRS**
TY MALAKAS 2010–09–22 / 03:21 UTC (AMSR-E)	**-0.92 HRS TO -0.27 HRS**	**0.65 HRS**
TY MALAKAS 2010–09–24 / 16:55 UTC (AMSR-E)	**1.01 HRS TO 1.58 HRS**	**0.57 HRS**
TY MEGI 2010–10–17 / 14:25 UTC (TRMM)	**2.38 HRS TO 2.92 HRS**	**0.54 HRS**
TY MALAKAS 2010–09–23 / 02:16 UTC (TRMM)	**0.53 HRS TO 0.93 HRS**	**0.40 HRS**

D.   STATISTICS

Even though the database was separated into three distinct groupings of observation types and time differences, initial analysis of the data indicated it needed to be refined even further for this project. This information would ensure the statistics would be representative of the TC environment.

1.   Data Classification

Several different areas needed to be addressed to have consistent SFMR and satellite data sets for this project.

a.   *TC Cases*

The environment surrounding a TC is very complex and has multiple factors that affect the strength and the translation speed and direction. The most important question concerning these factors is the location of the rainbands in relation to the flight track. The storm-relative flight path represents the inner-core cases well due to the relatively slow evolution of the eyewall provided the storm intensity is steady and storm motion is constant throughout the period that the aircraft is in the storm environment. Due to this consistency, the inner-core storm observations are the top choice to be used for this project.

The outer rainbands often evolve more rapidly than the features in the storm core. Even with the adjustment to a storm-relative coordinate system, the time differences between the satellite pass and the flight path over outer rainbands are too large to be considered as a representative measurement. That is, between the times of the SFMR and satellite observations, the outer rainbands may have either moved away from the region or completely dissipated. Because this situation is not deemed representative, none of the other TC cases will be considered in this project.

b.   *Aircraft Altitude*

The SFMR footprint changes depending on the altitude of the WC-130J along the flight path.   The SFMR will provide more representative rain rate measurements in the inner-core regions if the flight altitude is approximately 700 mb (~10,000 ft MSL). At this altitude, the SFMR footprint size is near the same footprint size of the satellite platforms. Even though it would introduce some error into the representativeness of the footprint, it was decided to restrict the data analysis to levels from 600 mb (~15,000 ft MSL) and below. This ensures the SFMR footprint size will be approximately the same for the satellite measurements and allows more representative comparisons for the inner-core cases.

c.   *Rain Rates*

Each platform has previously been evaluated (see references earlier in this chapter) to determine whether bias and errors are present in the measuring techniques. Many of these studies have been conducted using land-based platforms and buoy data at/near coastal regions. Since neither one of these platforms may be truly representative of the oceanic boundary layer and upper atmosphere, some of the error estimates from these studies may not be applicable for the atmospheric conditions considered here nor over the open sea regions. However, it is widely accepted that the smaller rain rates are not as accurate as the larger rain rates due to the capability to measure brightness temperatures and assumptions regarding cloud drop size distributions within the storm structure.

Smaller rain rates may also be contaminated with local surface-related noise within the observations. To lessen the effects of this surface noise, rain rates below 1 mm h^{-1} were not considered in the analysis.

2.   Case Classification

a.   Initial Comparisons

Due to the lack of comparisons of SFMR rain rates with TRMM and AMSR-E rain rates, the objective of this thesis is to establish general relationships between the rain rates from these platforms and to establish a baseline for further research.   The statistical analysis of the inner-core cases incorporate histograms, cumulative distribution functions, and Quantile-Quantile (Q-Q) plots to compare rain rates from each sensor. As a first step, the satellite-derived rain rate is compared directly to the TC SFMR data.

Since two of the three platforms measure brightness temperatures but all three measure attenuation parameters, it would be interesting to look at another parameter for inter-comparisons of the platforms. Each of the algorithms that calculate rain rates for the three platforms utilize Z-R relationships, which are logarithmic relationships between reflectivity (Z) and rain rate (R). Jorgensen and Willis (1982) suggested a general Z-R relationship for hurricanes to be $Z = 300R^{1.35}$. This relationship was used for many years until the Radar Operations Center released a new operations plan in 2008 that changed this relationship to $Z = 250R^{1.2}$ (ROC 2008).

Some discussion concerns the different Z-R relationships and the SFMR absorption model that is used in the algorithm. One impact is that the SFMR may be underestimating the rain rates from using these Z-R relationships (J. Carswell et al. 2012, unpublished manuscript). Building on the research of Jiang et al. (2006), the possibility of this underestimation has led to a proposed new algorithm for the SFMR rain rates that is $R_{adj} = (2.5*R_{orig})–5$ mm h^{-1}. This relationship will be evaluated using two approaches. The first compares both Z-R relationships utilizing the current SFMR absorption model. The second compares these relationships utilizing the suggested adjustment to the absorption model.

Also, a Kolmogorow-Smirnov (K-S) Test will be utilized. The K-S Test is a non-parametric test to determine whether two statistical distributions are equal in terms

of location and spread. This test assesses the maximum difference between the slopes of the cumulative distribution functions. In the application of the K-S test, the distribution of satellite- and aircraft-based rain rates are compared. The null hypothesis is that the two rain rates are from the same distribution. The alternative hypothesis is that they are from different distributions.

b.   TRMM PR Versus AMSR-E

A major disadvantage in using only inner-core cases was that only AMSR-E observations were available to compare the TC eyewall and surrounding structure during the periods of study. That is, these time differences for the AMSR-E were very minimal between the satellite pass and the flight times for eyewall penetration. By contrast, the TRMM PR passes were not appropriate because not many directly measured a TC eyewall pass. Also, the TRMM PR measurements of the inner core typically had time differences with the aircraft SFMR observations that were too large to be usable for this project. Therefore, only one TRMM PR case was considered.

The TRMM PR satellite pass over TC Sinlaku at 1944 UTC on 12 Sep 2008 occurred approximately two hours after the AMSR-E satellite pass that was included in the inner core cases. There were enough data points within the 3-h period for the TRMM PR pass to have an adequate comparison between the TRMM PR and the AMSR-E platforms within an eyewall region. Only the times when the two satellite passes coincided with the 3-h period were taken into consideration and used within the statistics. This comparison could be useful in further understanding the primary differences of how these two platforms remotely sense certain conditions within the atmosphere, but to also help determine if the algorithms used for calculating rain rates are doing so correctly.

III. ANALYSIS

Improved diagnosis of the dynamical structure of a TC (wind fields, rain rates, size, and shape) will allow improvements to techniques that are used to forecast TC impacts. Within the military hierarchy, this information can be extremely useful for providing leaders with a threat assessment concerning military operations and asset protection, whether it is by land, air, or sea.

This project examines aircraft-derived rain rates in relation to satellite-based rain rates during the T-PARC/TCS-08 and ITOP 2010 field campaigns. Two TCs were selected from T-PARC/TCS-08 and two TCs were selected from ITOP 2010. The primary satellite-based platform used in this project is the AMSR-E sensor. While each case has an AMSR-E pass over the TC center during the allowable time interval around the aircraft mission, one of the cases (TY Sinlaku on 12 Sep 2008) presents a unique opportunity to examine a combination of satellite-based platforms. The TRMM TMI/PR sensors passed over TY Sinlaku approximately two hours after the AMSR-E sensor pass.

A. AMSR-E, TRMM TMI/PR, AND SFMR COMPARISON

On 12 Sep 2008, the AMSR-E sensor passed over the eyewall of TY Sinlaku at approximately 1734 UTC (Figure 14a). The TRMM PR/TMI sensors recorded a pass over the eyewall at approximately 1944 UTC (Figure 14a). The WC-130J was operating within TY Sinlaku during both of these passes. This situation presented a unique opportunity to compare the different satellite-based platforms to the SFMR as both satellite passes occurred within the allowable time with respect to the WC-130J flight time.

1. Comparison of SFMR Rain Rates and Satellite-Based Rain Rates

a. SFMR Rain Rates and AMSR-E Rain Rates

The WC-130J began an alpha pattern near 1610 UTC 12 Sep, and encountered the southeastern part of the eyewall near 1625 UTC 12 Sep (Figure 14b).

While the agreement between the SFMR and AMSR-E rain rates is generally good (Figure 15), the SFMR rain rates exhibit a higher degree of variability than the AMSR-E rain rates. As the aircraft approached the first pass into the storm center between 1600 and 1630 UTC 12 Sep, the distribution of SFMR rain rates was a bit broader than the AMSR-E data. While in the eye of TY Sinlaku around 1700 UTC 12 Sep (Figures 14b, 15), the SFMR rain rates were near zero while the AMSR-E values become small but not zero, which is due to the data characteristics of the satellite-based rain rates. The aircraft passed through the northwestern portion of the eyewall between 1720 and 1740 UTC 12 Sep (Figure 14b). The AMSR-E and SFMR rain rates were smaller than those in the southeast portion of the eyewall (Figure 15). At the time of the maximum AMSR-E rain rates near 1730 UTC 12 Sep, the SFMR data were defined to be suspect, which was due to the aircraft turning at the northern-most portion of the alpha pattern (Figure 14b). During the north-to-south leg along the western portion of the alpha pattern, the rain rates from AMSR-E and SFMR were quite similar. Between 1810–1840 UTC 12 Sep, the aircraft passed through the northeast portion of the eyewall (Figure 14b). At this time, the rain rates for the SFMR and AMSR-E were again quite similar (Figure 15) until the aircraft flew along the outer portion of the eyewall where some large spikes in the SFMR rain rate occurred. These spikes may have been due to aircraft turns in the convective region because just after the large SFMR rain rate values near 1845 UTC 12 Sep, a near-30 minute period of SFMR data were flagged as suspect.

In general, the distributions of rain rate (Figure 16a) from the SFMR and AMSR-E exhibit shapes that are typical of rain rate data. The majority of values are near zero or near zero, which is indicative of numerous light rain rates. A long tail extends toward higher rain rates that are infrequent.

(a)

(b)
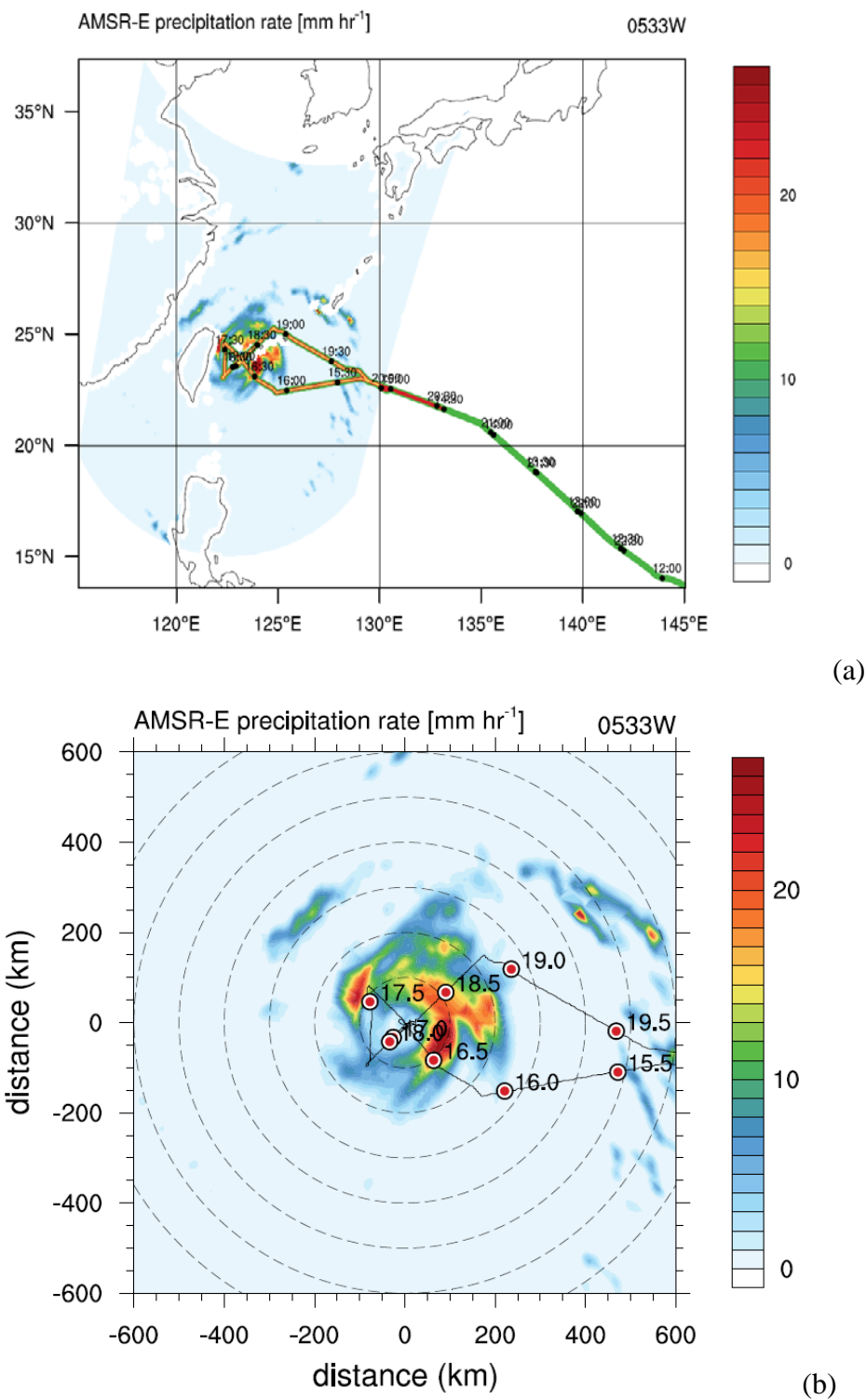
Figure 14.   As in Figures 10 and 11, except for the ASMR-E and (a) earth-relative
                  flight track and (b) storm-relative flight track for TY Sinlaku
                  on 12 Sep 2008.

Figure 15.   Rain rate (mm h^{-1}) from AMSR-E (red line), averaged SFMR rain rate
(blue line), and aircraft location in terms of radial distance (km) from
the storm center (green line) for TY Sinlaku on 12 Sep 2008. The lower x-axis
is the number of hours since the listed reference data and time. The upper x-axis
is the time difference of the satellite pass from the flight path times.

Whereas the SFMR rain rate histogram exhibits a fairly smooth decrease
in frequency toward higher rain rates, the AMSR-E histogram has two maxima in relative
frequency. The AMSR-E histogram has fewer values near 0 mm h^{-1} that were identified
as the rain rate values in the eye of TY Sinlaku (Figure 15). The decrease in frequency
near 0 mm h^{-1} is related to an increased frequency of rain rates just above 0 mm h^{-1}
(Figure 16a). The AMSR-E rain rates between 7–10 mm h^{-1} were also more frequent
than SFMR rain rates in this range. Then, the AMSR-E rain rates between 12–18 mm h^{-1}
were less frequent than the SFMR values. These same characteristics are identified in the
CDF plot (Figure 16b) and the Q-Q plot (Figure 16c). The SFMR and AMSR-E lower

rain rates have a similar distribution. Just under 10 mm h^{-1}, differences between the relative frequencies of rain rate values of the two sensors become evident by the change in the cumulative probability associated with the AMSR-E data (Figure 16b) and the deviations of the data from the diagonal line on the Q-Q plot (Figure 16c).

Based on the K-S test, the hypothesis that the SFMR and AMSR-E rain rates have the same distribution is rejected at a very high significance level. The rejection is based on the differences between the SFMR and AMSR-E CDFs that primarily occur from the medium intensity rain rates at 10–15 mm h^{-1} (Figure 16b).
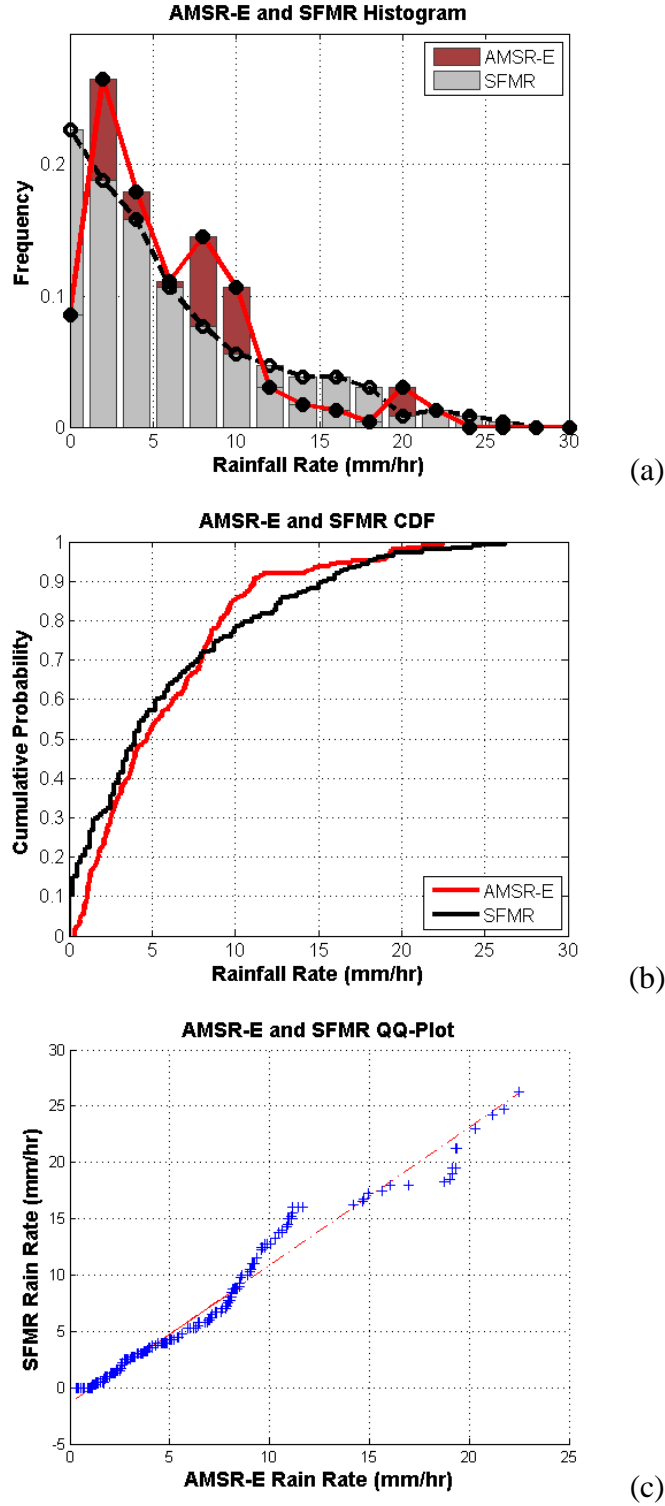
Figure 16.   Statistical characteristics of the SFMR and AMSR-E rain rates
                  for TY Sinlaku on 12 Sep defined as (a) rain rate frequencies,
            (b) cumulative distribution functions, and (c) quantile-quantile plots.

b.   *SFMR Rain Rates and TRMM PR Rain Rates*

The TRMM PR pass began as the aircraft completed the first transit through the eye of TY Sinlaku (Figure 17b). As with the AMSR-E rain rates, the changes in the SFMR and TRMM PR rain rates agree fairly well along the north-to-south portion of the alpha pattern between 1720 and 1745 UTC 12 Sep (Figure 18). However, the TRMM PR values are much larger than the SFMR data. During the second eye pass between 1800 and 1815 UTC 12 Sep, the TRMM PR rain rates are near zero, which matches the SFMR values. At the time of the pass through the northeast portion of the eyewall (Figure 17b), a very large maximum in the TRMM PR rain rates (Figure 18) occurs at the time when the aircraft data were flagged as suspect due to a turn in the aircraft path. Therefore, it is not possible to definitively compare the TRMM PR spike to the SFMR data. However, the TRMM PR values are generally higher than the SFMR data throughout the flight (Figure 18).

The large spike in the TRMM PR rain rate occurs in the enhanced convective regions within the eyewall. These extreme rain rates are usually considered to be a microscale feature rather than a mesoscale feature. Considering the geographical footprint of the TRMM PR, the 5 km by 5 km region would likely be too large to reliably measure that extreme rain rate. Therefore, another explanation must be sought to help explain the extreme rain rate value. Ikai and Nakamura (2003) describe known errors with the TRMM PR that occur in certain geographical regions. Two of the errors concern the western North Pacific. These errors are a combination of (1) inadequate Z-R relationships for convective and stratiform rain types and (2) possible inadequate estimation of the rain layer when it is convective. Even though this extreme rain rate value occurs in the region of the eyewall, it is a fairly large region of enhanced convection. These error characteristics could explain why this localized maximum occurred.

TRMM PR precipitation rate [mm hr⁻¹]   0533W

(a)

(b)

Figure 17.   As in Figures 10 and 11, except for the TRMM PR and (a) earth-relative
flight track and (b) storm-relative flight track for TY Sinlaku
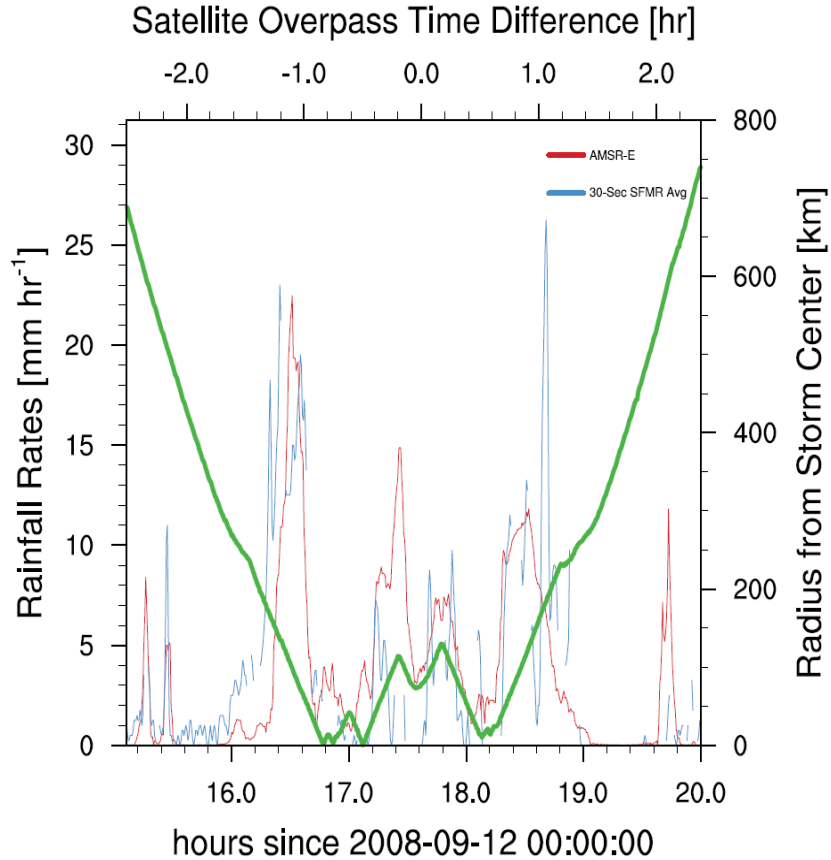on 12 Sep 2008.
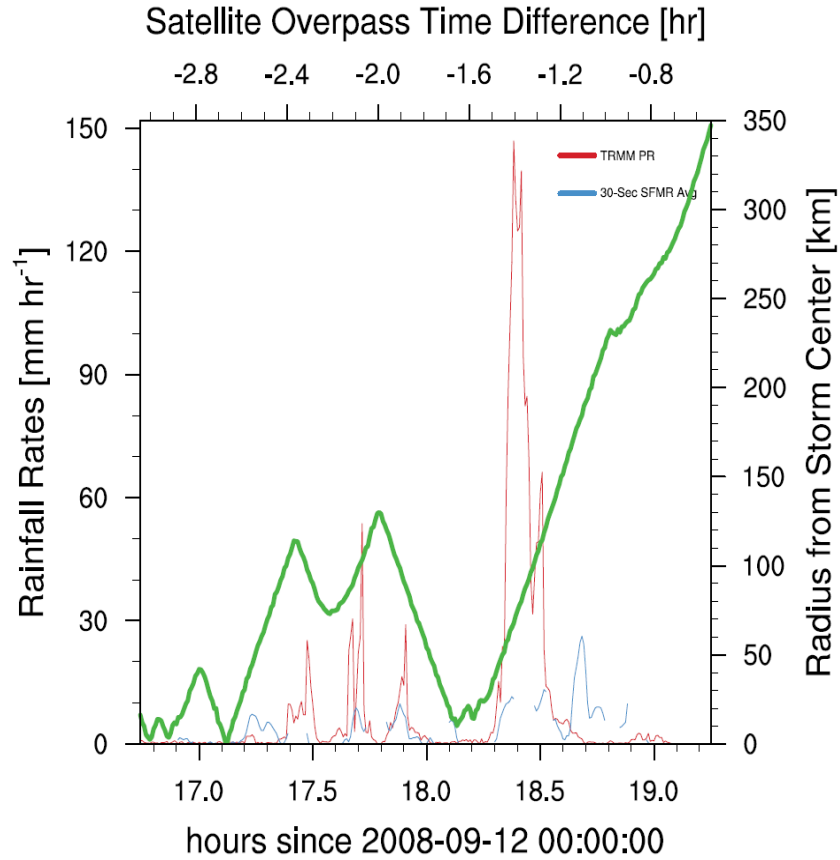
Figure 18.   As in Figure 15, except for the TRMM PR for TY Sinlaku
on 12 Sep 2008.

The overall statistical comparison of TRMM PR and SFMR rain rates is difficult because of the spikes in TRMM PR data. In addition, the TRMM PR rain rates differ significantly from the AMSR-E rain rates near zero mm h^{-1} (Figure 19a). Rain rates between 4–10 mm h^{-1} are more frequent with the SFMR. The CDF (Figure 19b) and the Q-Q plot (Figure 19c) are severely affected by the large values of TRMM PR rain rates. From the statistical characteristics of the TRMM PR data, it is clear that the two rain rate distributions are not equal, which was confirmed by the K-S Test. The null hypothesis that the SFMR and TRMM PR rain rate distributions were equal was rejected at a significance level of 0.05.

39

Figure 19.   Statistical characteristics of the SFMR and TRMM PR rain rates
for TY Sinlaku on 12 Sep defined as (a) rain rate frequencies,
(b) cumulative distribution functions, and
(c) quantile-quantile plots.

c.   ***SFMR Rain Rates and TRMM TMI Rain Rates***

The TRMM TMI pass began as the aircraft completed the first pass through the eye of TY Sinlaku (Figure 20b). As with the AMSR-E data, the time of the maximum TRMM TMI rain rates occurred near 1730 UTC 12 Sep. However, the SFMR data were flagged as suspect due to an aircraft turn. Some differences are noted between the SFMR-derived rain rates during the period of 6 mm h^{-1} TRMM TMI values near 1800 UTC 12 Sep (Figure 21). Also, the TRMM TMI data have three relative maxima at 1700, 1745, and 1800 UTC 12 Sep. At these times, the SFMR rain rates have been flagged as suspect so no direct comparison can be made. During the second eye pass between 1800 and 1815 UTC 12 Sep, the TRMM TMI rain rates are near zero, which matches the SFMR values. During the pass through the northeast portion of the eyewall between 1815 and 1845 UTC 12 Sep, the SFMR and AMSR-E rain rates matched fairly well, except for the large SFMR rain rate near 1840 UTC 12 Sep. As discussed above, this large SFMR maximum is suspect and it occurred just prior to a 30-minute period of data that were flagged due to aircraft turns.

Figure 20.   As in Figures 10 and 11, except for the TRMM TMI and (a) Earth-relative flight track and (b) storm-relative flight track for TY Sinlaku on 12 Sep 2008.
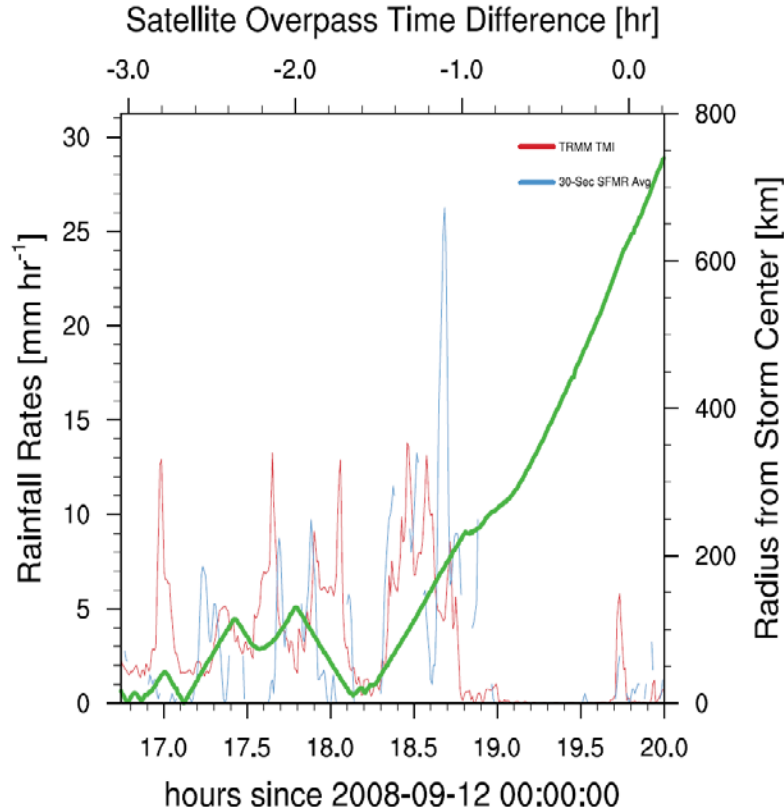
Figure 21.   As in Figure 15, except for TRMM TMI for TY Sinlaku
on 12 Sep 2008.

As was the case with the AMSR-E rain rates, the relative frequency of TRMM TMI rain rates near 0 mm h^{-1} (Figure 22a) is less than that of SFMR rain rates. This appears to be a fundamental difference with the TRMM PR distribution in which the relative frequency of near 0 mm h^{-1} rain rates is greater than SFMR. There is an increased frequency of TRMM TMI rain rates over SFMR between 2–5 mm h^{-1} (Figure 22a) and a decreased frequency at medium rain rates between 7 and 10 mm h^{-1}.

While the statistical characteristics of the TRMM TMI rain rates are not influenced by the extremely high values that were found in the TRMM PR data (Figures 19b, c), the distributions of the TRMM TMI and SFMR rain rates were found to not be statistically equal based on the K-S Test as the null hypothesis of equal distributions was rejected at a significance level of 0.05. The primary cause to reject the hypothesis is the difference in the relative frequencies in the interval of 7–10 mm h^{-1}.
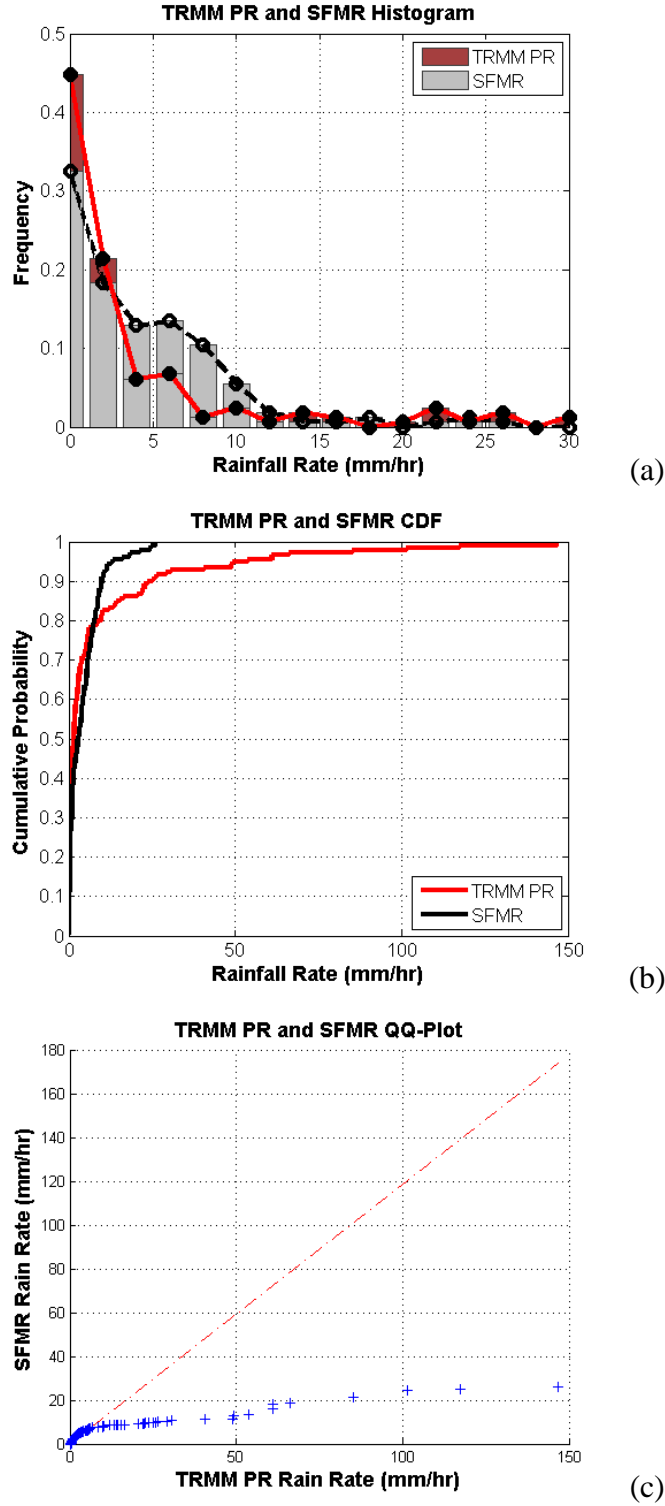
43
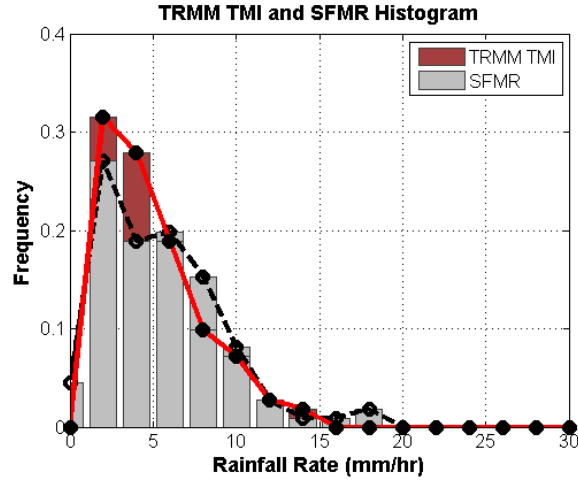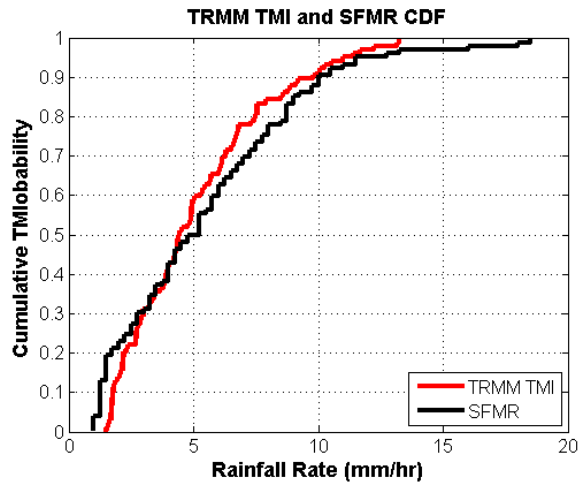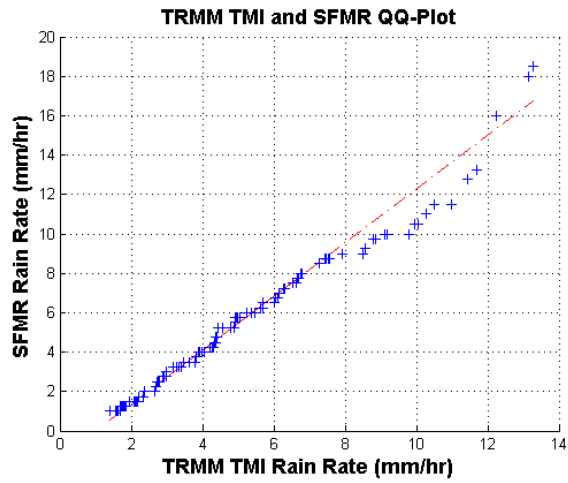
Figure 22.   Statistical characteristics of the SFMR and TRMM TMI rain rates
for TY Sinlaku on 12 Sep defined as (a) rain rate frequencies,
(b) cumulative distribution functions, and
(c) quantile-quantile plots.

2. AMSR-E Rain Rates and TRMM TMI Rain Rates

The availability of the AMSR-E and the TRMM TMI passes over TY Sinlaku provided an opportunity to directly compare these two passive microwave sensors. It is clear from the histograms of the two rain rates (Figure 23a) that the largest difference is due to the increase in frequency of AMSR-E rain rate intensities beyond 8 mm h^{-1} (Figure 23b, c). Recall that the increase in frequency of AMSR-E rain rates at ranges of 8–10 mm h^{-1} was the primary difference in the distribution of SFMR and AMSR-E rain rates. The differences between the rain rates defined by the two sensors are large enough that the null hypothesis of equal distribution was rejected by the K-S Test at a significance level of 0.05.

Figure 23.   Statistical characteristics of the AMSR-E and TRMM TMI rain rates
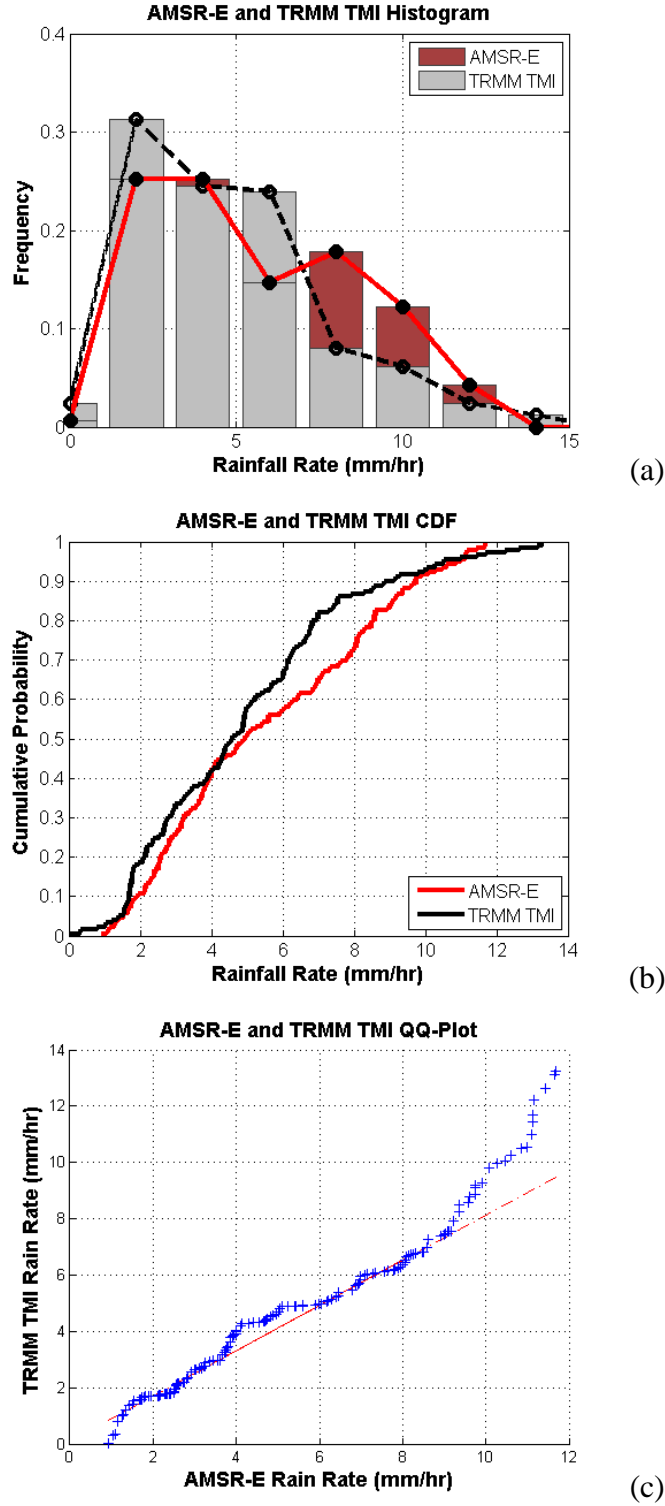for TY Sinlaku on 12 Sep defined as (a) rain rate frequencies,
(b) cumulative distribution functions, and
(c) quantile-quantile plots.

B. INDIVIDUAL STORM CASES

In this section, the SFMR and AMSR-E rain rates are examined for the remainder of the inner-core cases. For background information, the storm-relative flight tracks and satellite passes are examined in relation to the time series of SFMR and AMSR-E rain rates. However, the individual distributions, CDFs, and Q-Q plots are contained in the Appendix.

1. TY Malakas–23 Sep 2010

The AMSR-E sensor passed over the eyewall of TY Malakas at 1613 UTC 23 Sep 2010 (Figure 24a). The WC-130J began the butterfly pattern near 1550 UTC 23 Sep, and encountered the southern part of the eyewall near 1600 UTC 23 Sep (Figure 24b). While in the eye of TY Malakas around 1620 UTC and again around 1800 UTC 23 Sep, the AMSR-E rain rates are near zero while the SFMR values became small (Figure 25), but not zero, which is opposite to what was found in the TY Sinlaku case. The aircraft passed through the northern portion of the eyewall between 1630 and 1645 UTC 23 Sep (Figure 24b). The SFMR and AMSR-E rain rates were approximately equal to the rain rates experienced in the southern edge of the eyewall (Figure 25). The aircraft began a northwest-to-southeast leg around 1720 UTC 23 Sep. During this leg of the butterfly pattern, rain rates for the SFMR and AMSR-E were quite similar (Figure 25) until the aircraft flew along the southeastern portion of the eyewall (Figure 24b) where there was a large maximum in the SFMR rain rates. The occurrence of maximum SFMR rain rates at 1800 UTC 23 Sep compared to the maximum AMSR-E rain rates at 1830 UTC 23 Sep may be due to a time offset with the AMSR-E data. The time difference between the satellite and aircraft measurements is near two hours (Figure 25) and the convective characteristics may have changed in that time.

Figure 24.   As in Figures 10 and 11, except for the AMSR-E and
            (a) earth-relative flight track and (b) storm-relative flight track
                    for TY Malakas on 23 Sep 2010.

Figure 25.   As in Figure 15, except for the AMSR-E for TY Malakas
                              on 23 Sep 2010.

2.   TY Sinlaku–09 Sep 2008

The AMSR-E sensor passed over the eyewall of TY Sinlaku at 0454 UTC 09 Sep 2008 (Figure 26a). The WC-130J began the alpha pattern near 0420 UTC 09 Sep, and encountered the southern portion of the eyewall near 0445 UTC 09 Sep (Figure 26b). The SFMR and AMSR-E rain rates were approximately the same (Figure 27) as the aircraft passed through the southern portion of the eyewall near 0500 UTC 09 Sep. At 0600 UTC 09 Sep, the aircraft began a west-to-east leg across the storm center. This early portion of the leg was outside of any eyewall convection, which is defined very well in both the SFMR and AMSR-E rain rates that are approaching zero mm h^{-1} (Figure 27). The aircraft continues on this portion of the leg from 0600–0700 UTC 09 Sep. The SFMR and AMSR-E rain rates match very well through the western portion of the

eyewall between 0600–0630 UTC 09 Sep. However, there appears to be some offset between the SFMR and AMSR-E rain rates through the eastern portion of the eyewall. Time differences between the satellite and aircraft increased beyond two hours may account for these differences in rain rates.

(a)

(b)
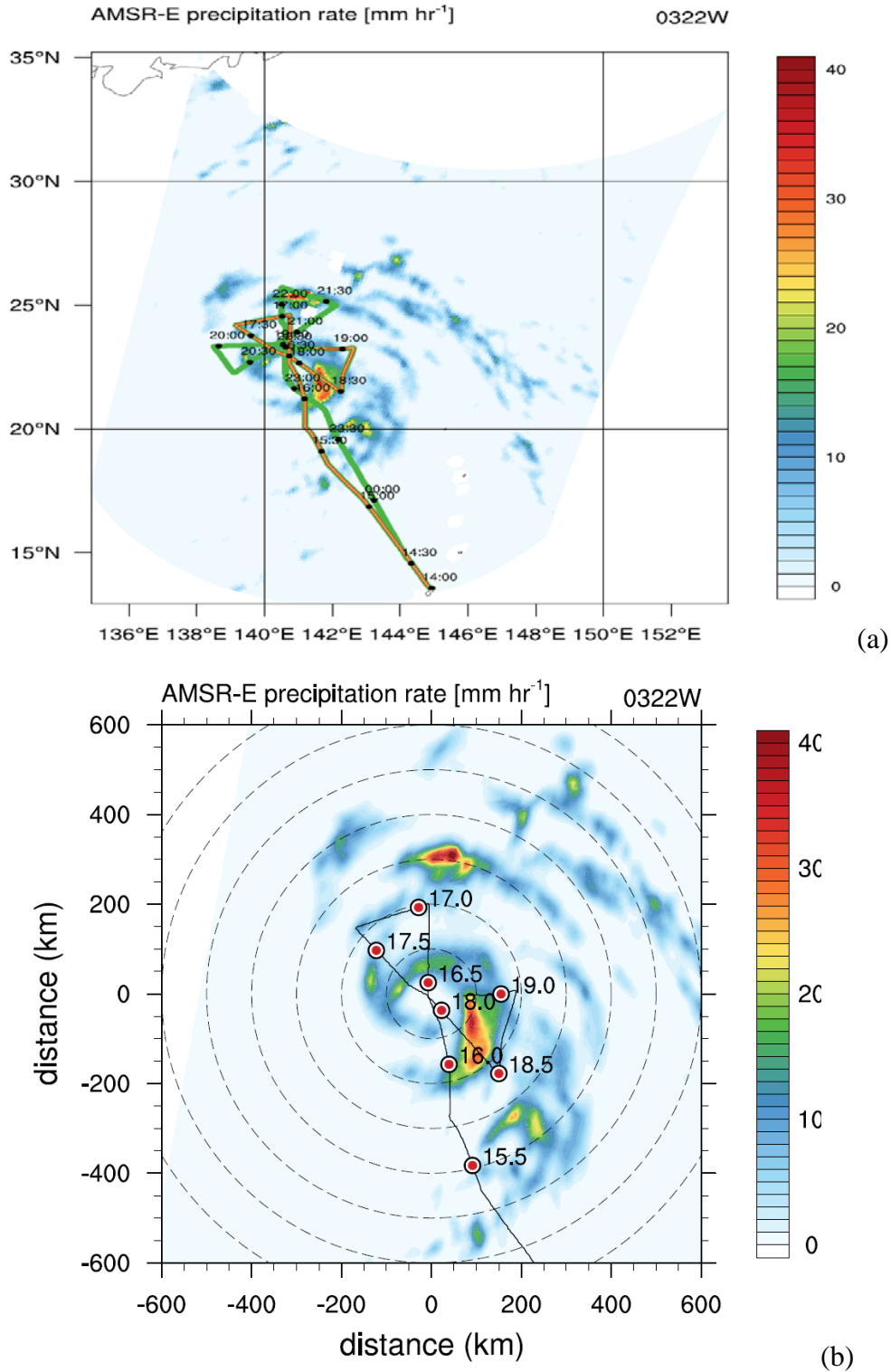
Figure 26.   As in Figures 10 and 11, except for the AMSR-E and
             (a) earth-relative flight track and (b) storm-relative flight track
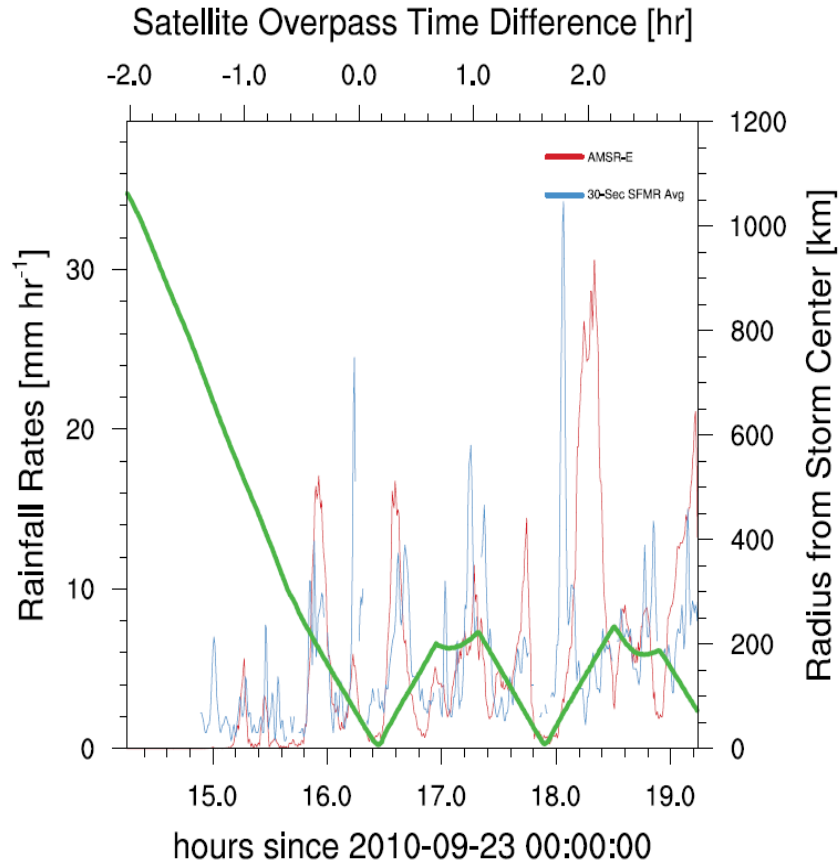   for TY Sinlaku on 09 Sep 2008.

Figure 27.   As in Figure 15, except for the AMSR-E for TY Sinlaku
on 09 Sep 2008.

3.   TY Jangmi–27 Sep 2008

The AMSR-E sensor passed over the eyewall of TY Jangmi at 0442 UTC 27 Sep 2008 (Figure 28a). The WC-130J began the alpha pattern near 0550 UTC 27 Sep and encountered the northeastern portion of the eyewall near 0600 UTC 27 Sep (Figure 28b). The aircraft began a northeast-to-southwest leg from 0600–0650 UTC 27 Sep and passed through the center of TY Jangmi at 0630 UTC 27 Sep (Figure 28b). However, due to multiple turns by the aircraft in the eye of TY Jangmi, the SFMR data were flagged as suspect and could not be compared to the AMSR-E rain rate data (Figure 29). The aircraft continued on toward the southwest portion of the eyewall and the SFMR and AMSR-E rain rates were approximately the same throughout this portion of the leg. The

aircraft began a south-to-north leg of the alpha pattern at 0730 UTC 27 Sep (Figure 28b). However, due to the limitations of the 3 h data period ending, the comparison of the SFMR data with the AMSR-E data had to be terminated at 0745 UTC 27 Sep.

(a)

(b)
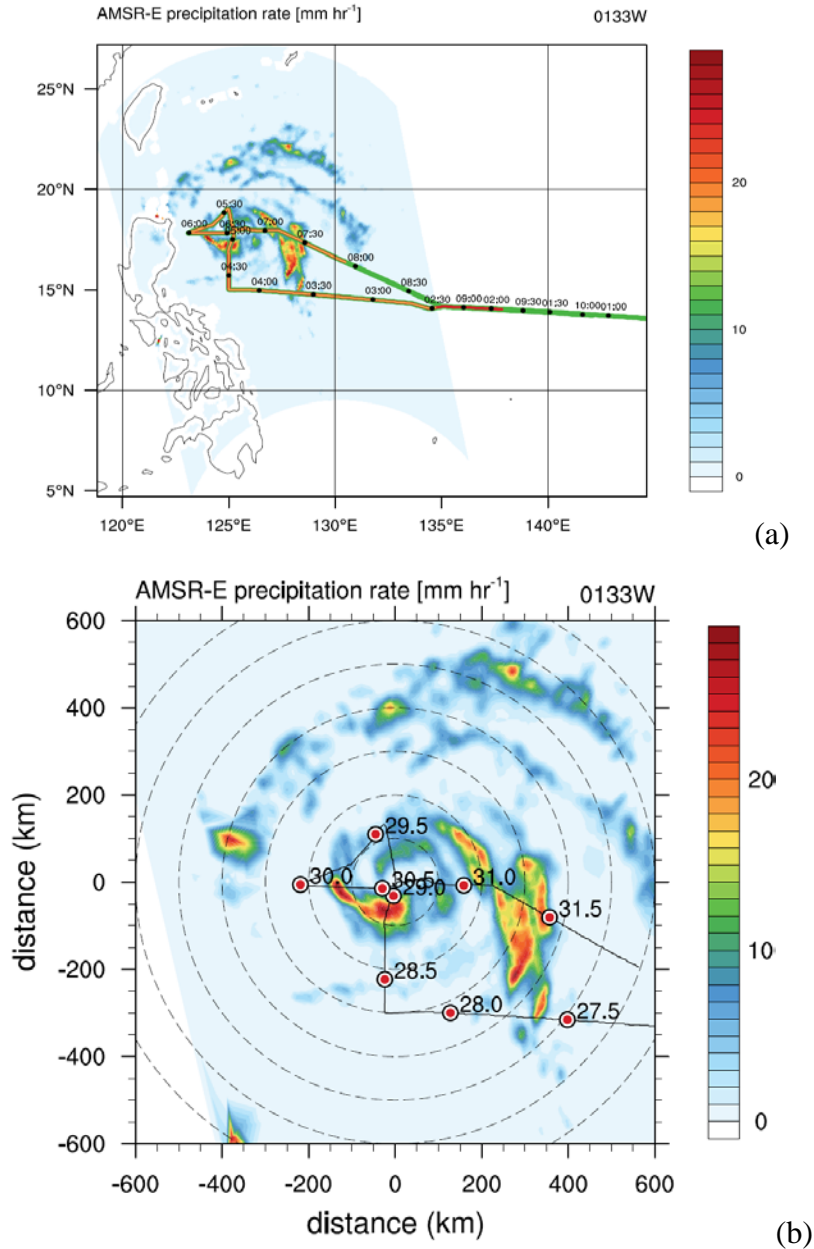
Figure 28.   As in Figures 10 and 11, except for the AMSR-E and (a) earth-relative flight track and (b) storm-relative flight track for TY Jangmi on 27 Sep 2008.
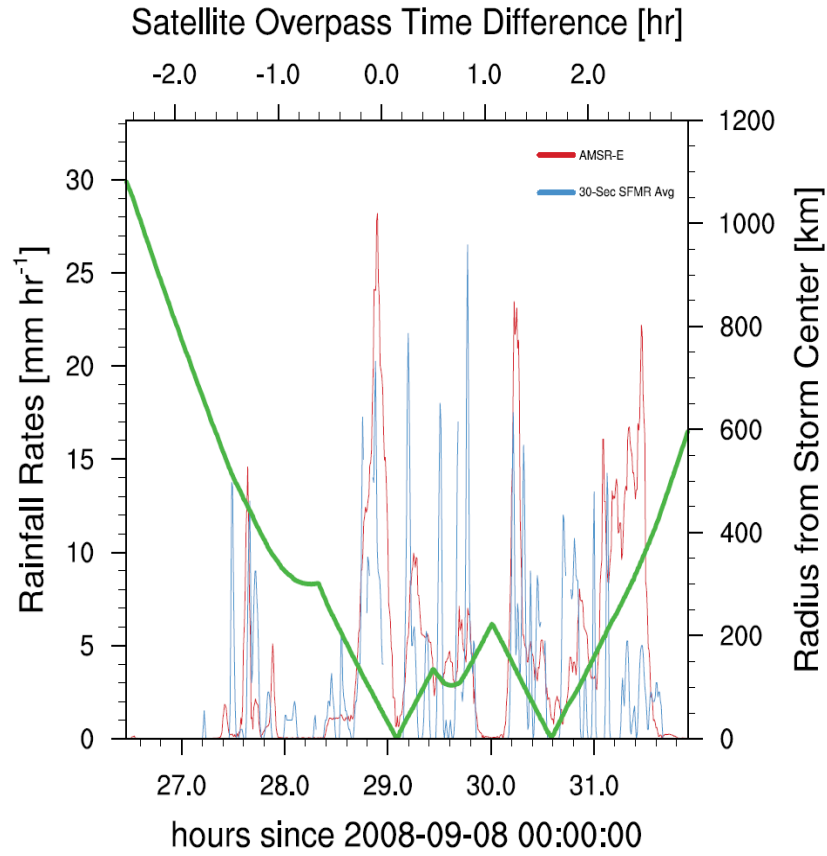
Figure 29.   As in Figure 15, except the AMSR-E for TY Jangmi
on 27 Sep 2008.

4.   TY Fanapi–17 Sep 2010

The AMSR-E sensor passed over the eyewall of TY Fanapi at 0445 UTC on 17 Sep 2010 (Figure 30a). The WC-130J began its alpha pattern (Figure 30b) well before the 3 h data period began. The AMSR-E data were not used until 0145 UTC 17 Sep. The aircraft began its last leg of the alpha pattern around 0215 UTC 17 Sep (Figure 30b), which became a northwest-to-southeast leg. The aircraft passed the northwest portion of the eyewall between 0220–0235 UTC 17 Sep (Figure 30b). The aircraft passed through the center of TY Fanapi at 0245 UTC 17 Sep. However, the AMSR-E rain rates contain a relative maximum at this time (Figure 31). The aircraft passed through the southeastern portion of the eyewall between 0250–0310 UTC 17 Sep (Figure 30b). During this flight leg, the time difference between the satellite and aircraft measurements was decreasing.

Consequently, the SFMR and AMSR-E rain rates matched very well (Figure 31). During this time, there were three separate peaks in SFMR rain rates (Figure 31). The individual maxima in the SFMR rain rates during this time may be explain by the sensitivities of the SFMR sensor to microscale features while the AMSR-E sensor resolution is more sensitive to mesoscale features. This period of near zero time differences between the satellite and aircraft that coincided with the well-defined physical structures of TY Fanapi resulted in the only individual case in which the hypothesis of equal distribution of SFMR and AMSR-E rain rates was not rejected (Figure 50c).
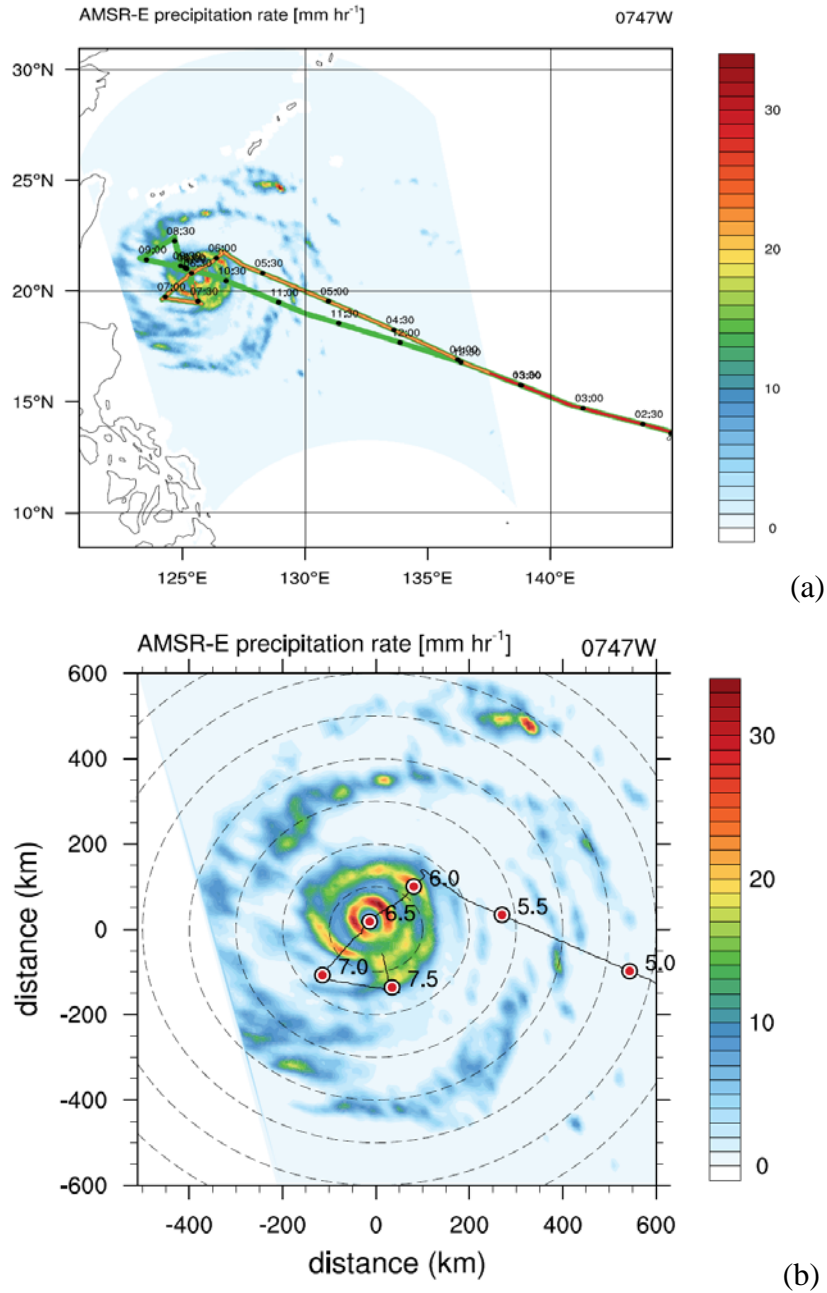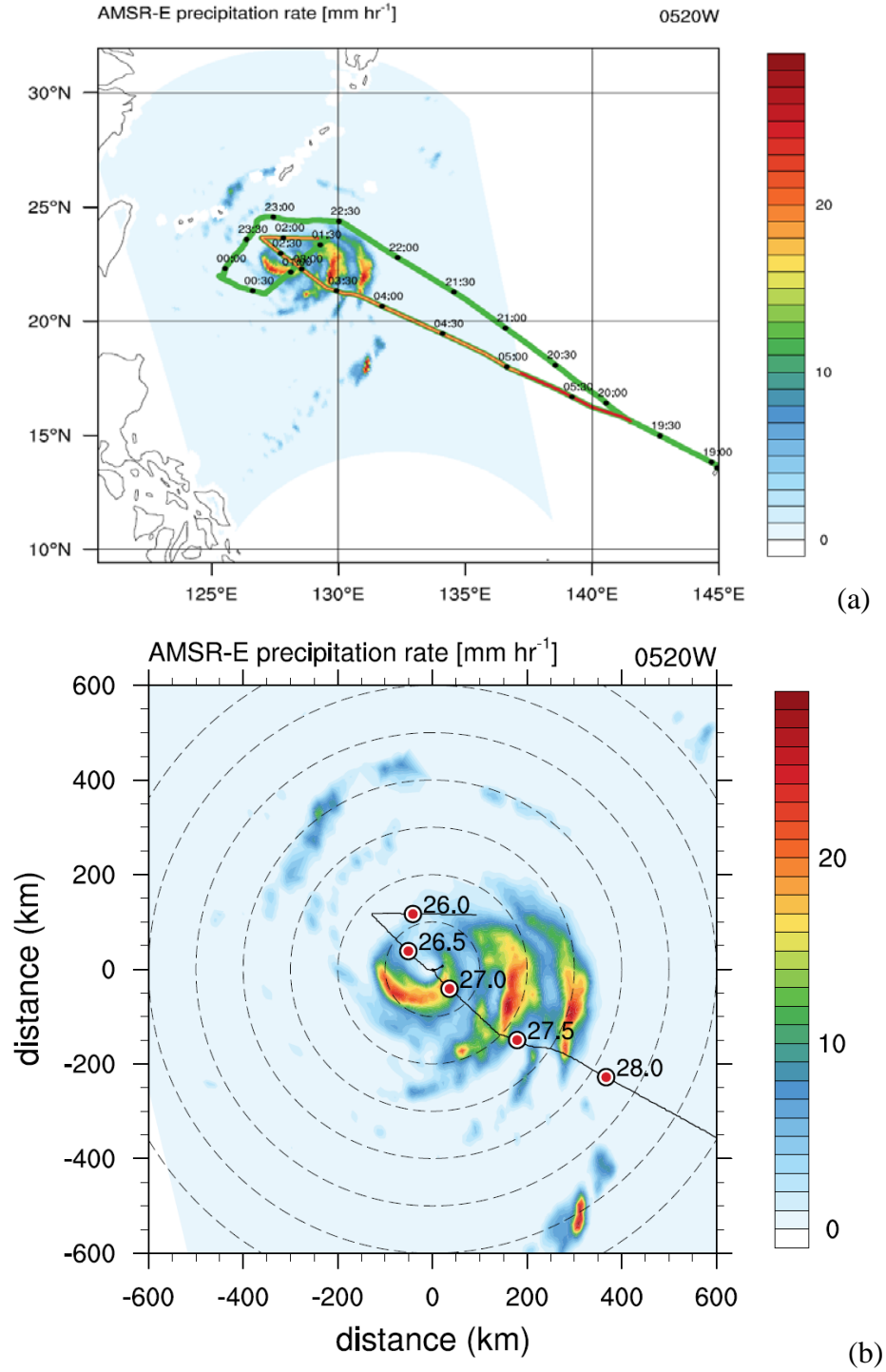
Figure 30.   As in Figures 10 and 11, except for the AMSR-E and
          (a) earth-relative flight track and (b) storm-relative flight track for
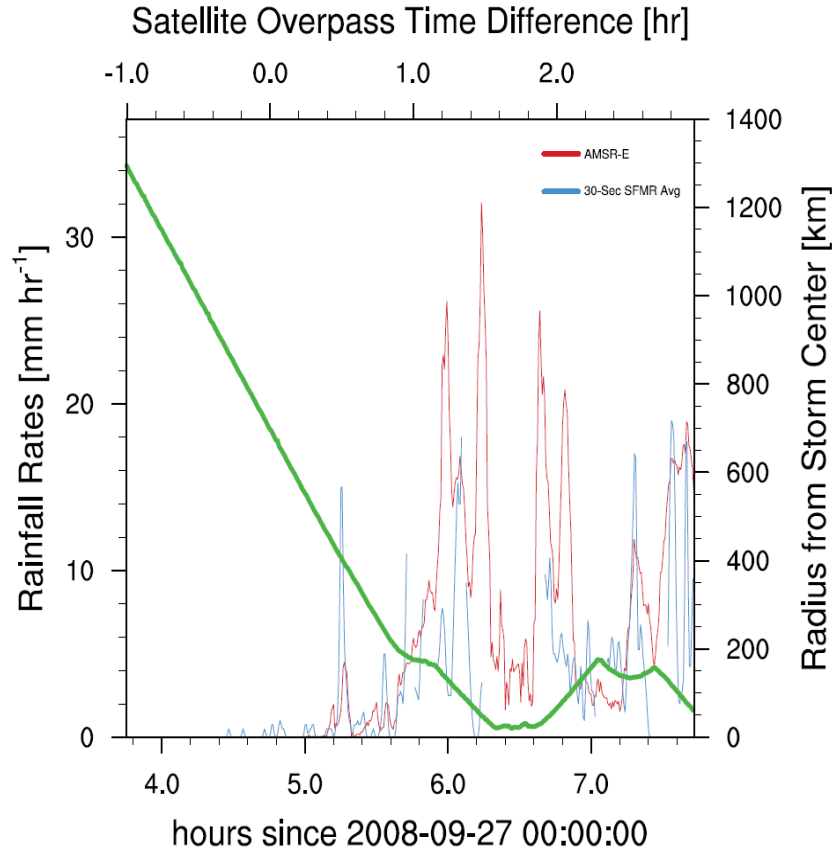   TY Fanapi on 17 Sep 2010.
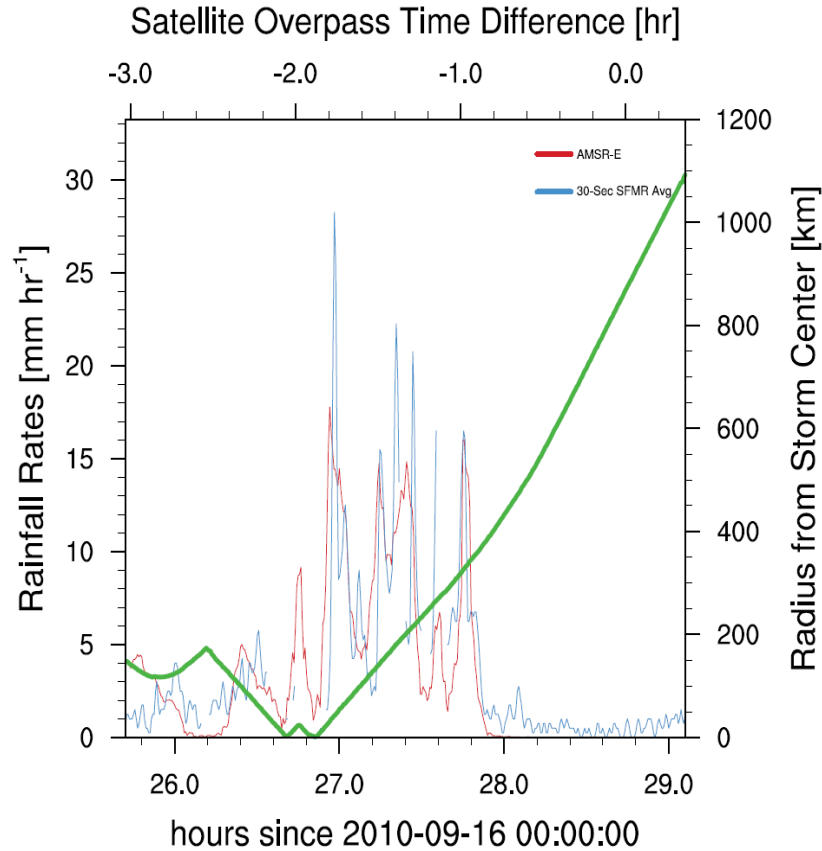
Figure 31.   As in Figure 15, except for the AMSR-E for TY Fanapi
on 17 Sep 2010.

5.   All Storms Combined

In this section, the statistical characteristics of sample of five individual cases defined above are examined.

a.   *SFMR Rain Rates and AMSR-E Rain Rates*

The less-frequent occurrence of AMSR-E rain rates near zero mm h^{-1} is clearly evident in Figure 32a. The reduced frequency of near zero mm h^{-1} rain rates may be related to the greater frequency of AMSR-E rain rates between 3 and 4 mm h^{-1}. The SFMR and AMSR-E have similar frequencies of rain rates between 5 and 10 mm h^{-1}. However, there are increased frequencies of AMSR-E rain rates between 12 and 15 mm h^{-1}. The impact of the low frequency of small rain rates in the AMSR-E is also

evident in the differences between the AMSR-E CDF and the SFMR CDF (Figure 32b). Because of these differences that increase toward higher rain rates, the K-S Test results in a rejection of the null hypothesis that the SFMR and AMSR-E distributions are equal.

Differences in the frequency of the SFMR and AMSR-E rain rates at higher rain rates (10–15 mm h^{-1}) are evident in the Q-Q plot (Figure 32c). These differences could be explained by the characteristics of the AMSR-E sensor. The AMSR-E platform remotely-senses microwaves coming from the atmosphere at different frequencies. The satellite measures up to six frequencies to calculate the water-based variables (i.e., water vapor, rain rates, drop size distribution). Depending on the frequency, other variables may be directly affected. For the 89 GHz frequency, which is the frequency being used in this project, brightness temperatures begin to drastically drop when rate rates begin to increase because the 89 GHz frequency band is sensitive to the scattering by ice particles suspended in high altitudes within deep convective regions. At lower frequencies (10.7 GHz and 18.7 GHz), which are closer to the measured frequencies for the SFMR, as rain rate increases, so does brightness temperature (Wilheit et al. 2003).

It is important to understand how the weighting functions applied to various frequencies impact the derivation of rain rates. For the AMSR-E platform, the oceanic precipitation is retrieved utilizing an algorithm that inputs the 1837, 36.5, and 89 GHz brightness temperatures (JAXA 2006). There are several depolarization methods that must be taken into account since the brightness temperatures are measured with dual-polarity. Once the depolarization is done, the algorithm gives twice the weight to the 89 GHz brightness temperature as it does for the 18.7 GHz. If the brightness temperature in the higher frequencies drops significantly (i.e., over a higher cloud top), this could introduce errors with higher rain rates that would be expected for such convective clouds. Based on the information in the QQ-plot, there is some evidence to suggest that the AMSR-E does not do well with rain rates that are higher than 20 to 25 mm h^{-1}. In terms of the average as a function of rain rates for the weight of each frequency, the higher rain rates are weighted more toward the 10.7 GHz channels (Jin et al. 2005).
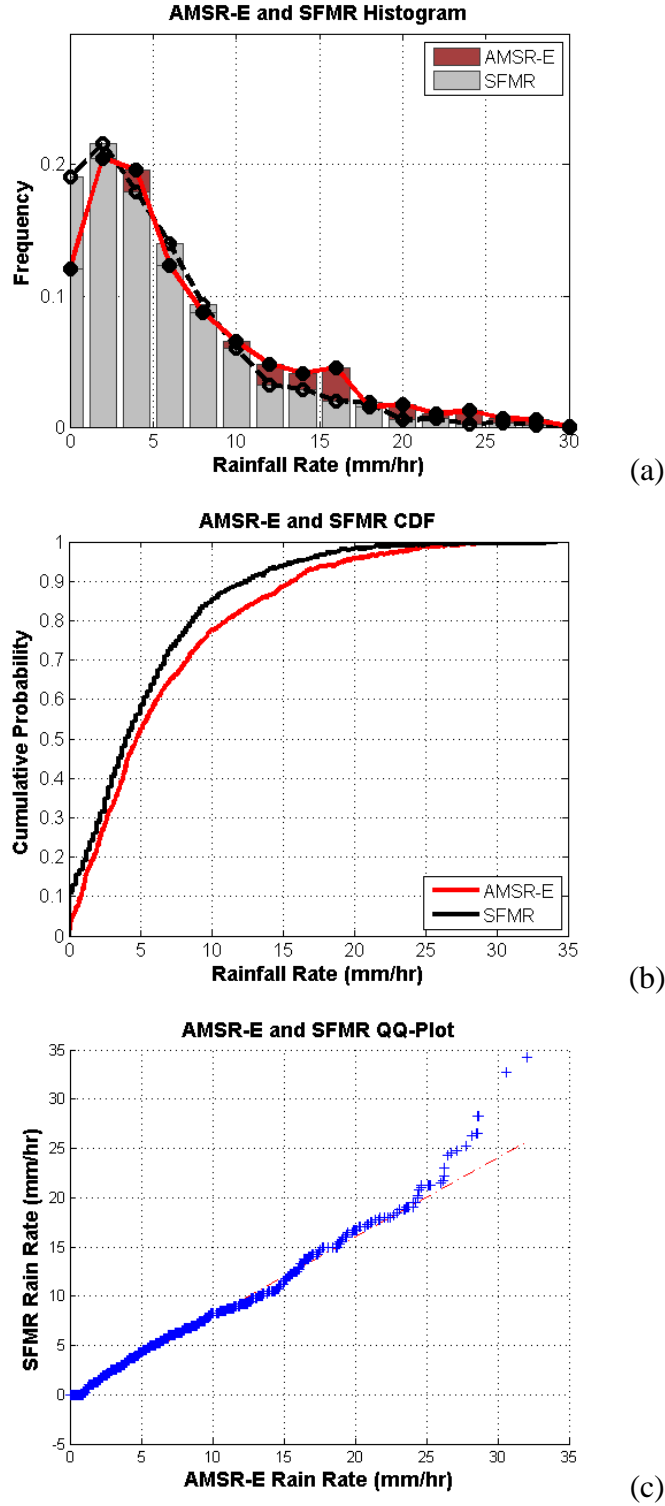
Figure 32.   Statistical characteristics of the SFMR and AMSR-E rain rates
            for combined inner-core cases defined as (a) rain rate frequencies,
                    (b) cumulative distribution functions, and
                        (c) quantile-quantile plots.

b.   *SFMR and AMSR-E dBZ*

i.   Jorgensen and Willis Z-R Relationship. The Jorgensen and Willis Z-R algorithm was applied to the SFMR and AMSR-E rain rate values for the combined data set.   The SFMR sensor has a higher frequency of observations near 35 dBZ (Figure 33a). This frequency peak can be related to the CDF (Figure 33b) as the SFMR and AMSR-E distribution functions separate around the 35 dBZ mark. There is also a small increase in the AMSR-E frequency between 40–45 dBZ (Figure 33a, b, c). The Q-Q plot identifies similar characteristics in that there is a large difference in distributions at the higher rain rates. At the lower rain rates, there is a difference due to the lower frequency of AMSR-E rain rates. The differences in the frequencies of rain rates at 35 dBZ contribute to the rejection of the K-S Test null hypothesis that the two distributions are the same.
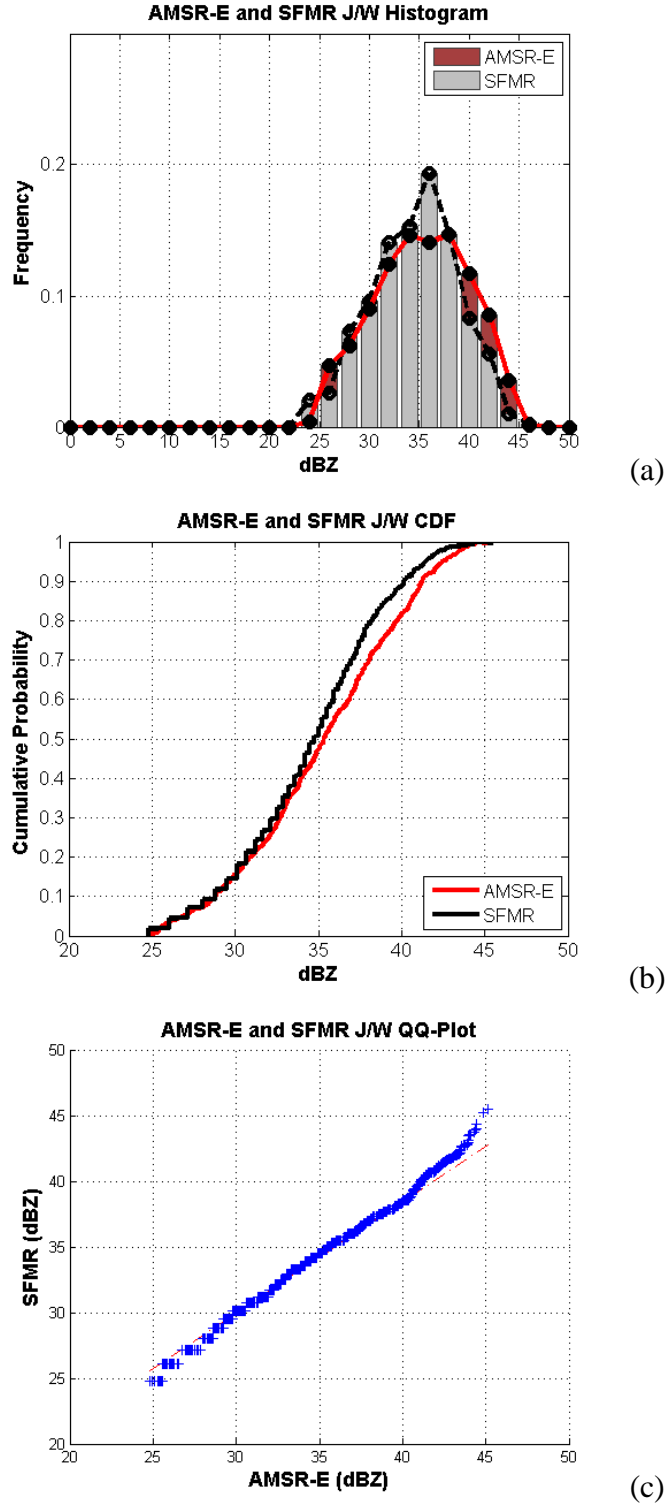
Figure 33. Statistical characteristics of the SFMR and AMSR-E J/W dBZ for combined inner-core cases defined as (a) rain rate frequencies, (b) cumulative distribution functions, and (c) quantile-quantile plots.

ii.   Carswell Z-R Relationship. The application of the Carswell Z-R relationship to the SFMR and AMSR-E rain rates produces similar results as with the Jorgensen and Willis relationship (Figure 34a). The CDF (Figure 34b) of the SFMR data lies above that of the AMSR-E throughout the range of dBZ values due to the increase in frequency of the SFMR observations below 30 dBZ (Figure 34a, c). Also, the increase in the frequency of AMSR-E observations above 35 dBZ in the Carswell Z-R relationship (Figure 34a) matches the same increase in the Jorgensen and Willis relationship (Figure 33a). These differences in both the upper and lower frequencies contribute to the rejection of the K-S test null hypothesis that the distributions are equal.
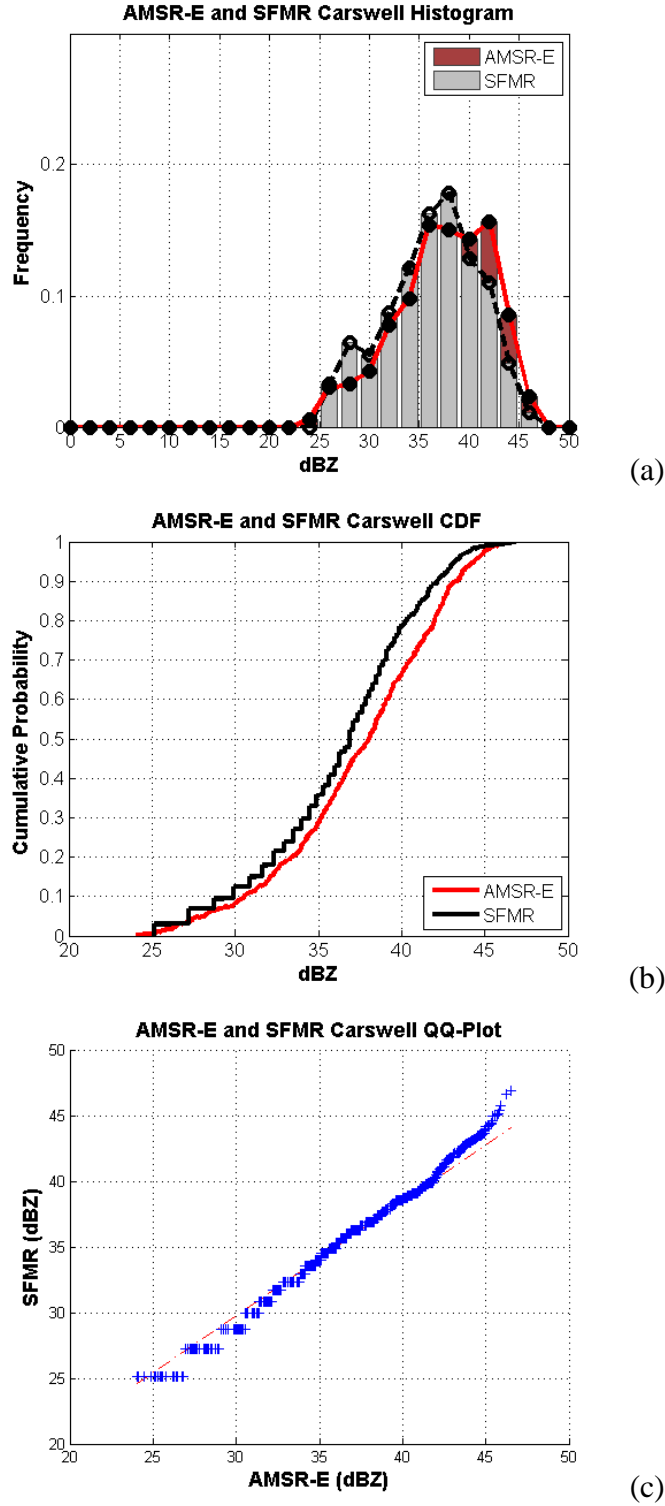
Figure 34.   Statistical characteristics of the SFMR and AMSR-E Carswell dBZ
                 for combined inner-core cases defined as (a) rain rate frequencies,
                 (b) cumulative distribution functions, and
                 (c) quantile-quantile plots.

IV. CONCLUSIONS

A. SUMMARY

Tropical cyclones are severe weather phenomena that occur throughout many oceanic regions and often impact shore- and land-based assets. TCs can disrupt normal, daily routines because of their high wind speeds, heavy rain fall, localized flooding, and even the possibility of tornadic activity. These conditions usually persist for one or more days, depending on the TC location and translation speed. Tropical cyclones affect not only the general public, but military operations across the globe. Therefore, being able to forecast the intensity and translation speed of a TC is an extremely important part of weather support for military operations. This improved information allows leaders to make better decisions based on risk management techniques that are directly affected by TC forecasts.

In this project, aircraft-derived rain rates acquired during T-PARC/TCS-08 and ITOP 2010 are examined in relation to satellite-based rain rates. A number of previous studies have shown that certain atmospheric parameters measured by aircraft instruments can be used to significantly improve the accuracy and forecast of TCs within the Atlantic basin. However, few studies have been conducted to examine these same atmospheric parameters over the tropical western North Pacific.

During these two field campaigns, scientists and technicians monitored and tracked multiple TCs throughout the western Pacific. Based on QC flags and specific atmospheric requirements, five of these storms were chosen for examination in this project. Each storm was analyzed individually for any particular trends that could be found, but most importantly, all of the data were combined to get an overall analysis of the statistical character. Multiple sensors were also compared during a particular event to see how they compared to one another.

1.   SFMR Rain Rates and AMSR-E Rain Rates

The frequency distribution of the SFMR rain rates is similar to that of the AMSR-E for rain rates between 2 and 10 mm h^{-1}. The frequency of AMSR-E derived rain rates between 10 and 20 mm h^{-1} was larger than the frequency of SFMR-derived rain rates. Based on the examination of the AMSR-E oceanic precipitation algorithm, this satellite instrument may be under-estimating the rain rates. This discrepancy is primarily due to the higher rain rates are shifted toward the lower frequencies that are being sampled by the SFMR. However, the SFMR onboard the aircraft is actually within the clouds and therefore may be better resolving the brightness temperatures associated with the heavier rain rates. Also, a slight bias toward reduced frequencies of near zero rain rates was identified with the AMSR-E.

2.   SFMR Z-R Relationships and AMSR-E Z-R Relationships

Overall, there was good agreement in the Z-R relationships for both sensors within the mid-level range of dBZ values. However, the same errors in the measurements of smaller and larger rain rates are apparent in the smaller and larger dBZ values. Both Z-R algorithms identified similar differences between SFMR and AMSR-E at high dBZ values. However, there is a larger amount of variability in the lower dBZ values using the Carswell Z-R relationship rather than the Jorgensen and Willis relationship.

3.   SFMR Rain Rates and TRMM PR Rain Rates

Due to the inherent differences in the remote-sensing capabilities of these two instruments, the amount and quality of data examined did not allow for specific conclusions as to the rain rate differences.

4.   SFMR Rain Rates and TRMM TMI Rain Rates

One case allows a different comparison of SFMR and TRMM TMI rain rates. For this particular case, the TRMM TMI did not record very high rain rates. The sources of bias are not known. However, if this bias can be rectified, the TRMM TMI data should model the SFMR and the AMSR-E quite well.

5. AMSR-E Rain Rates and TRMM TMI Rain Rates

As was found in the comparisons between SFMR and AMSR-E rain rates, the frequency of AMSR-E-derived medium range rain rates of 8–15 mm h^{-1} was larger than the frequency of TRMM TMI values in this range. At lower rain rates, the frequency distributions of the AMSR-E and TRMM TMI rain rates were similar.

B. RECOMMENDATIONS

Tropical cyclone dynamics and structure changes are constantly being investigated to develop new methods to generate accurate and timely forecasts. Due to the increasing focus of military operations throughout the data-sparse western Pacific basin, new observing systems need to be continually investigated to determine if methods developed in other regions of the world would be a benefit in the Pacific basin. This project has described the variability of brightness temperatures when dealing with differing frequencies of a particular sensor. This approach becomes significant since multiple sensors may ensure the best data is being obtained. If these instruments are trying to measure the same variable but errors and biases are identified, the quality of the data that are being collected is drastically degraded. It is important for forecasters, researchers, and military leaders to have to best quality, current, and up-to-date atmospheric data to ensure the most accurate and best decisions can be made to minimize cost and maximize mission effectiveness.

This project has examined a very small sample of data that may be used to further the research of TCs. Due to the limitations of this project using the TRMM PR sensor, further investigation needs to be done utilizing the TRMM TMI that has remote sensing frequencies similar to that of the AMSR-E and SFMR instruments. Instead of focusing solely on rain rates or Z-R relationships, variables such as attenuation versus brightness temperature may be used to derive not only rain rates but also wind speeds, temperature flux, and vertical motion. This investigation could lead to further analysis to determine whether or not the algorithms currently used for remote-sensing instruments are correctly observing the atmospheric parameters. Lastly, other remote-sensing platforms need to be utilized to ensure the data are accurate and effective. Aircraft radar data can be compared

to the SFMR data (as well as the TRMM PR sensor) to determine whether or not specific spikes in the SFMR data are due to localized convective enhancement (microscale versus mesoscale). Whereas only two procedures were examined within this project, analyses utilizing other platforms and/or procedures may further increase understanding and result in better quality of data for the forecasting of TC activity in data-sparse regions.
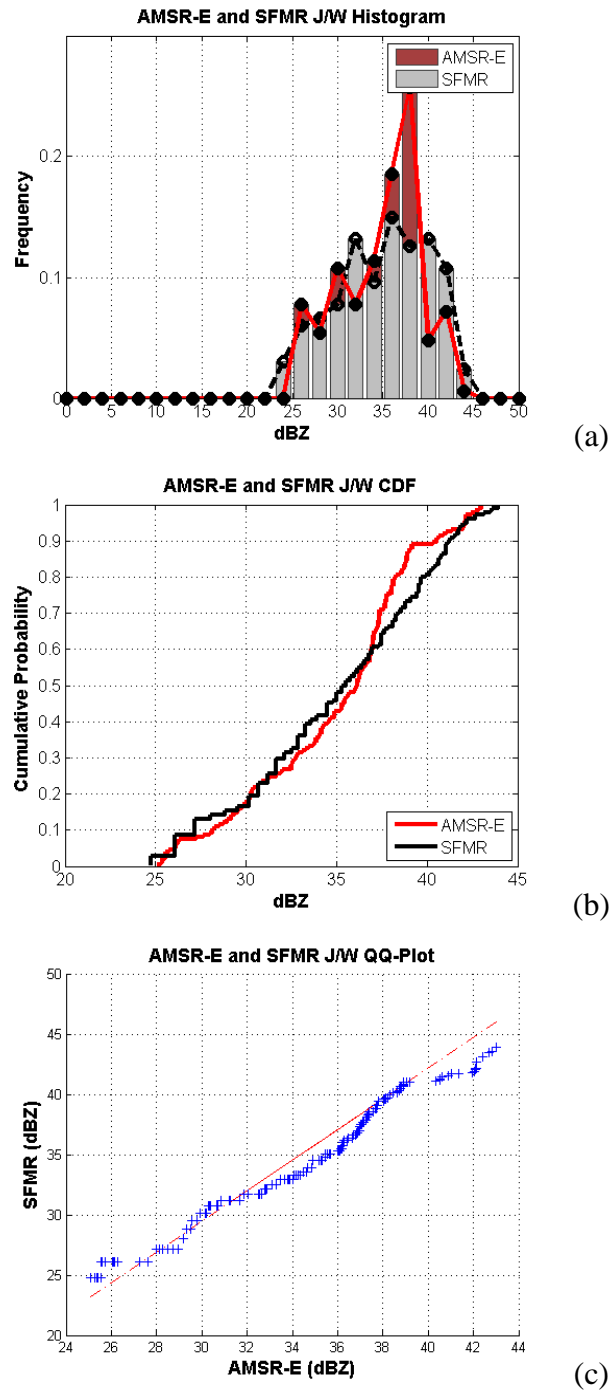
APPENDIX

(a)

(b)

(c)

Figure 35. Statistical characteristics of the SFMR and AMSR-E J/W dBZ for TY Sinlaku on 12 Sep defined as (a) rain rate frequencies, (b) cumulative distribution functions, and (c) quantile-quantile plots.
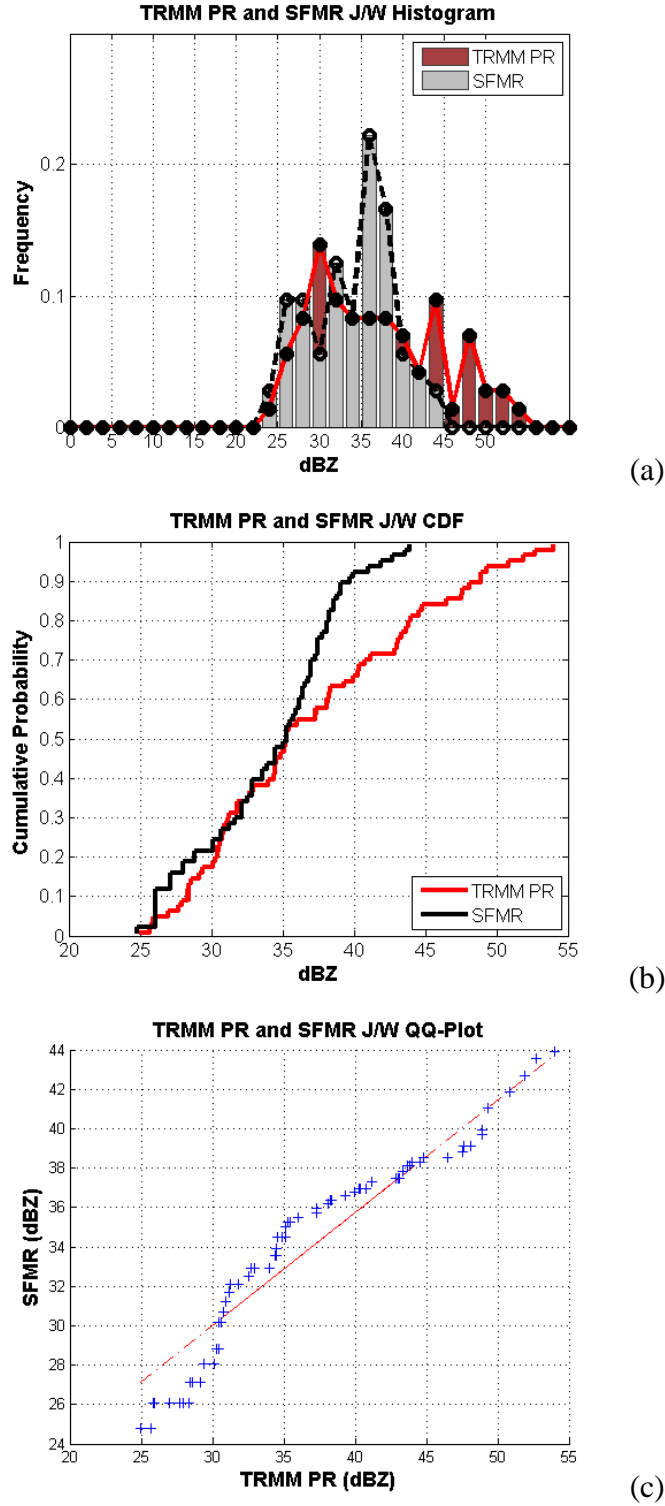
Figure 36. Statistical characteristics of the SFMR and TRMM PR J/W dBZ for TY Sinlaku on 12 Sep defined as (a) rain rate frequencies, (b) cumulative distribution functions, and (c) quantile-quantile plots.
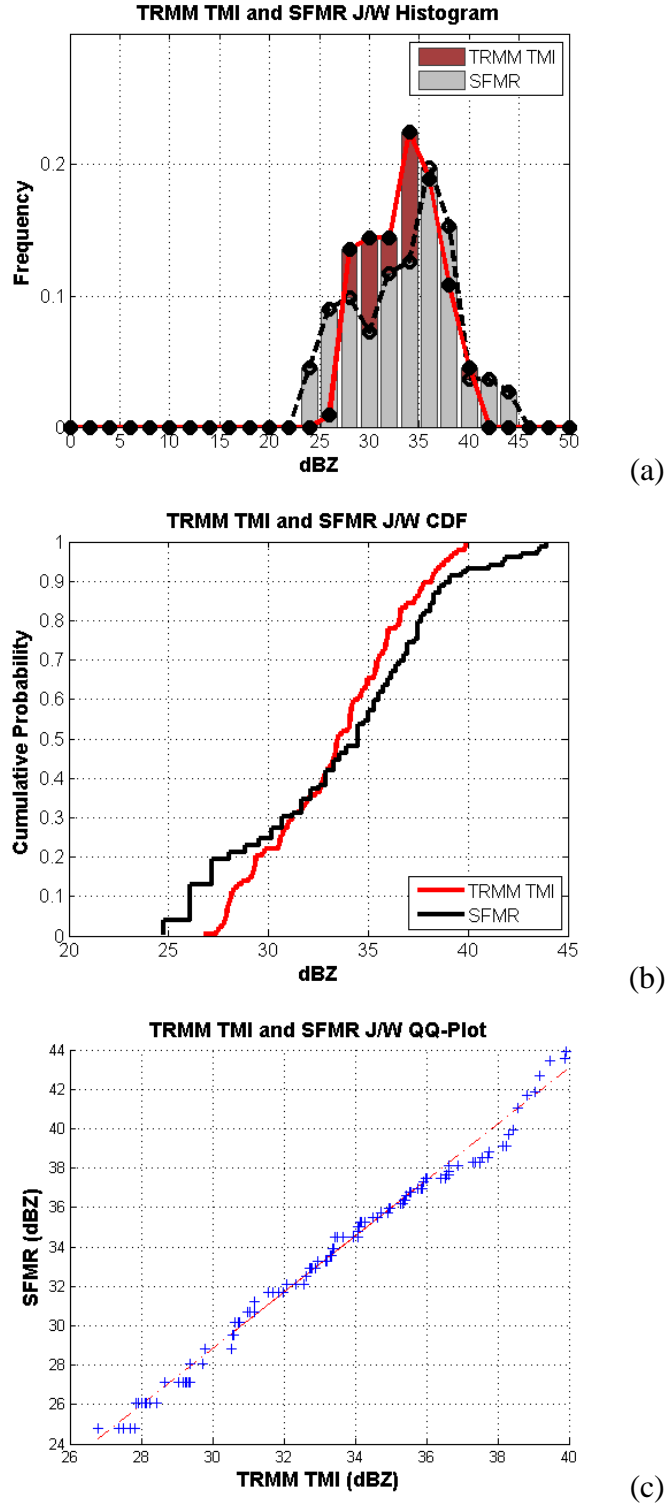
Figure 37.   Statistical characteristics of the SFMR and TRMM TMI J/W dBZ for TY Sinlaku on 12 Sep defined as (a) rain rate frequencies, (b) cumulative distribution functions, and (c) quantile-quantile plots.
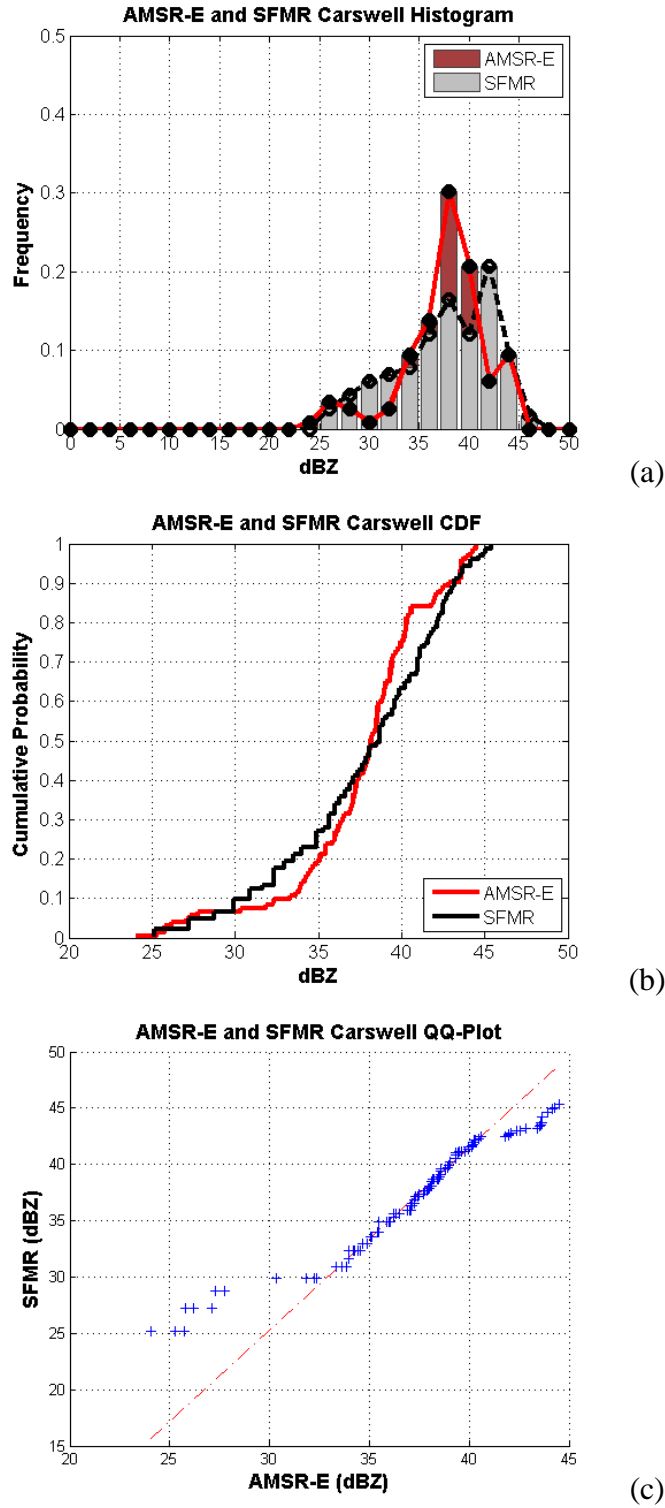
Figure 38. Statistical characteristics of the SFMR and AMSR-E Carswell dBZ for TY Sinlaku on 12 Sep defined as (a) rain rate frequencies, (b) cumulative distribution functions, and (c) quantile-quantile plots.
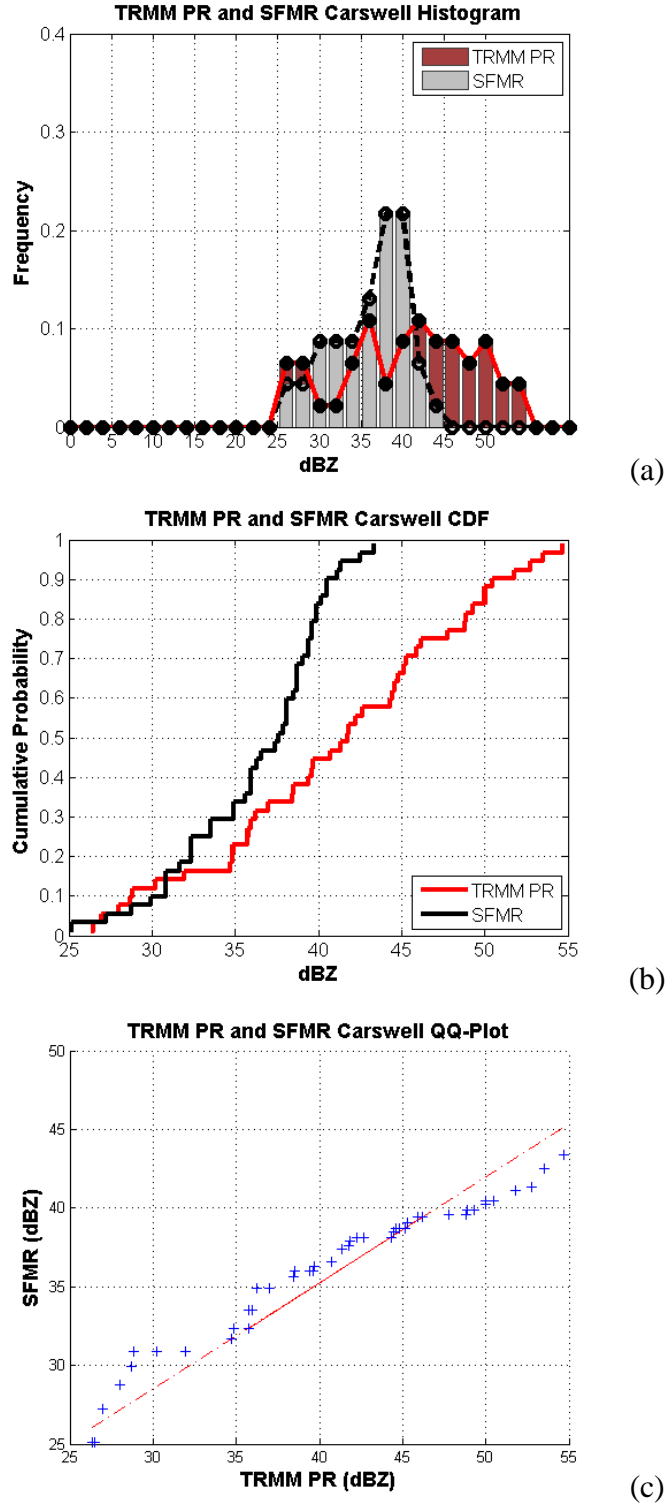
Figure 39. Statistical characteristics of the SFMR and TRMM PR Carswell dBZ for TY Sinlaku on 12 Sep defined as (a) rain rate frequencies, (b) cumulative distribution functions, and (c) quantile-quantile plots.
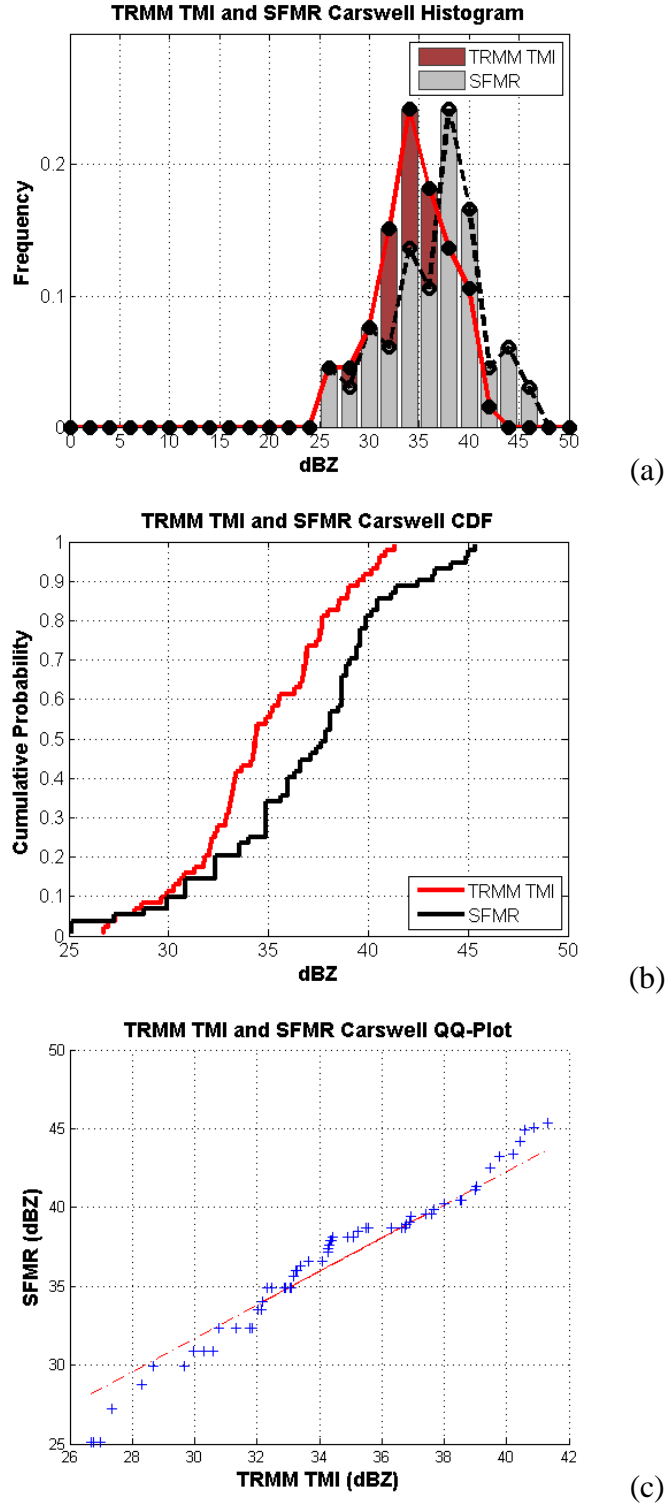
Figure 40.　　　Statistical characteristics of the SFMR and TRMM TMI Carswell dBZ for TY Sinlaku on 12 Sep defined as (a) rain rate frequencies, (b) cumulative distribution functions, and (c) quantile-quantile plots.
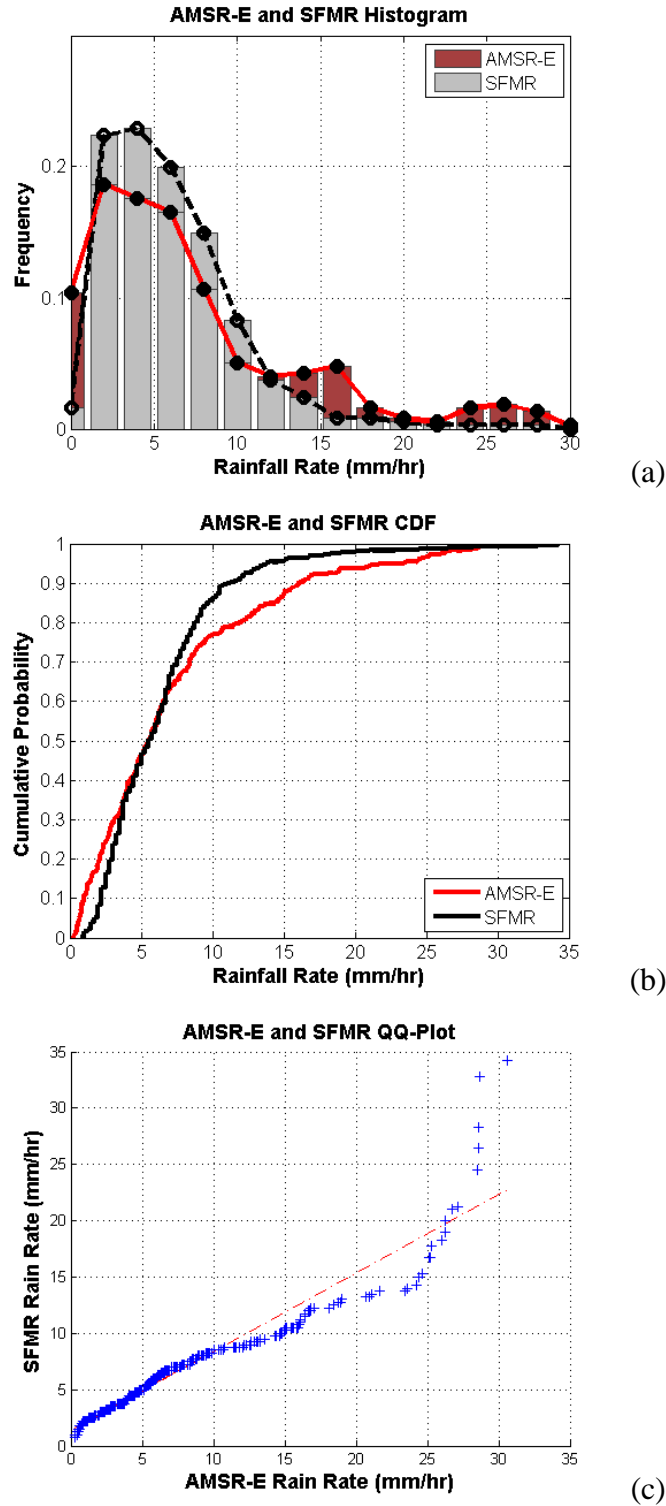
Figure 41.   Statistical characteristics of the SFMR and AMSR-E rain rates for TY
Malakas on 23 Sep defined as (a) rain rate frequencies, (b) cumulative distribution
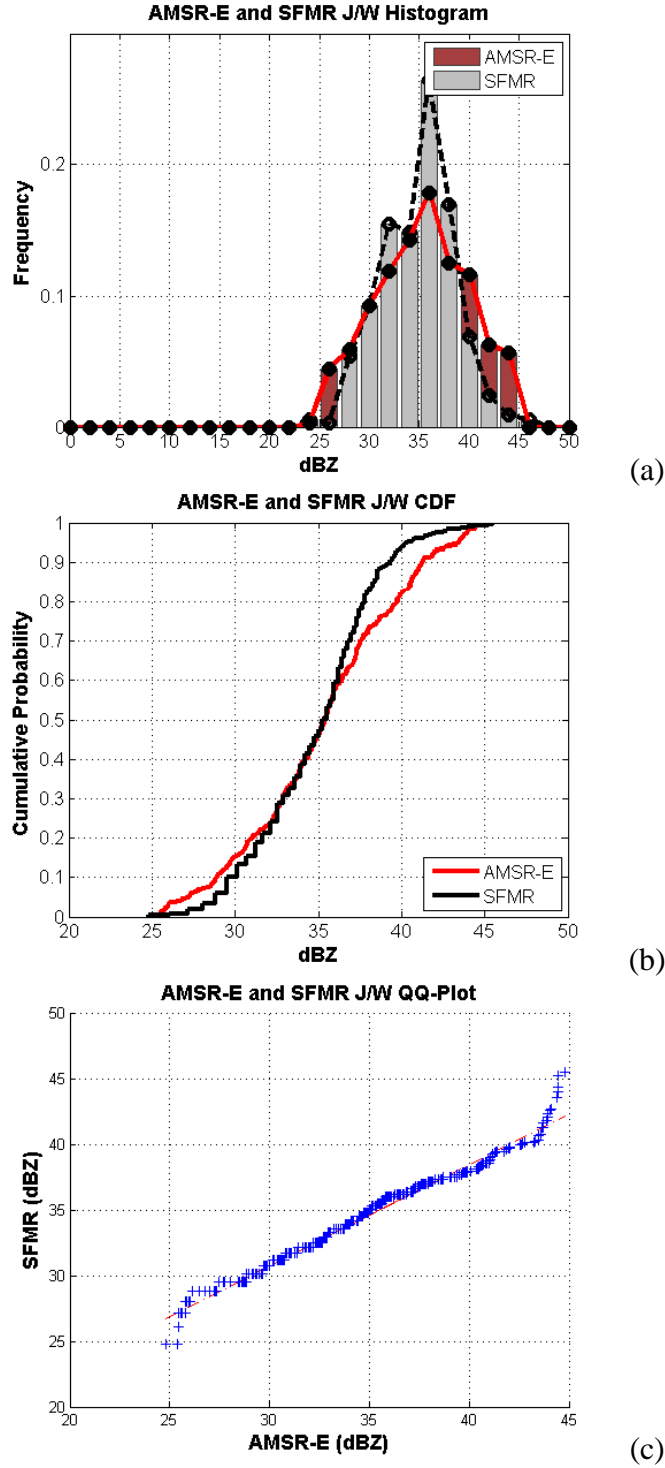functions, and (c) quantile-quantile plots.

Figure 42.   Statistical characteristics of the SFMR and AMSR-E J/W dBZ for TY
Malakas on 23 Sep defined as (a) rain rate frequencies, (b) cumulative distribution
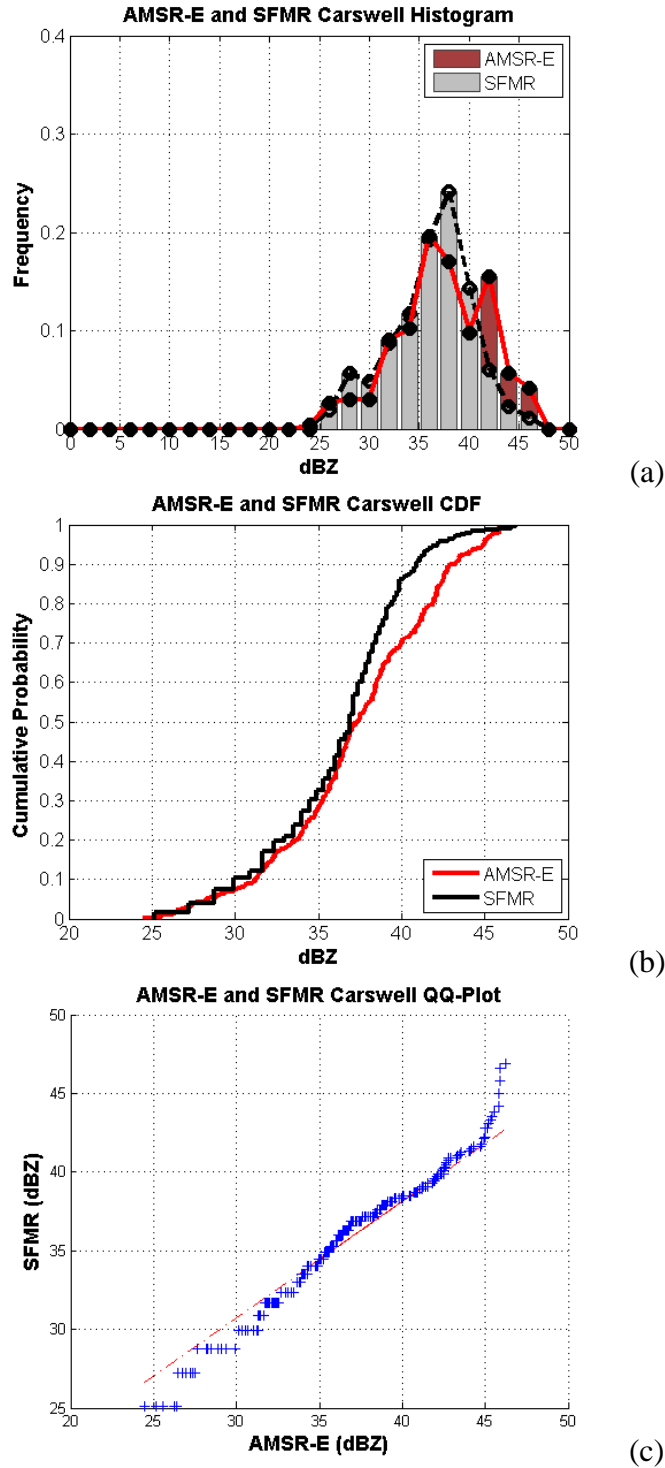functions, and (c) quantile-quantile plots.

Figure 43.   Statistical characteristics of the SFMR and AMSR-E Carswell dBZ for TY Malakas on 23 Sep defined as (a) rain rate frequencies, (b) cumulative distribution functions, and (c) quantile-quantile plots.
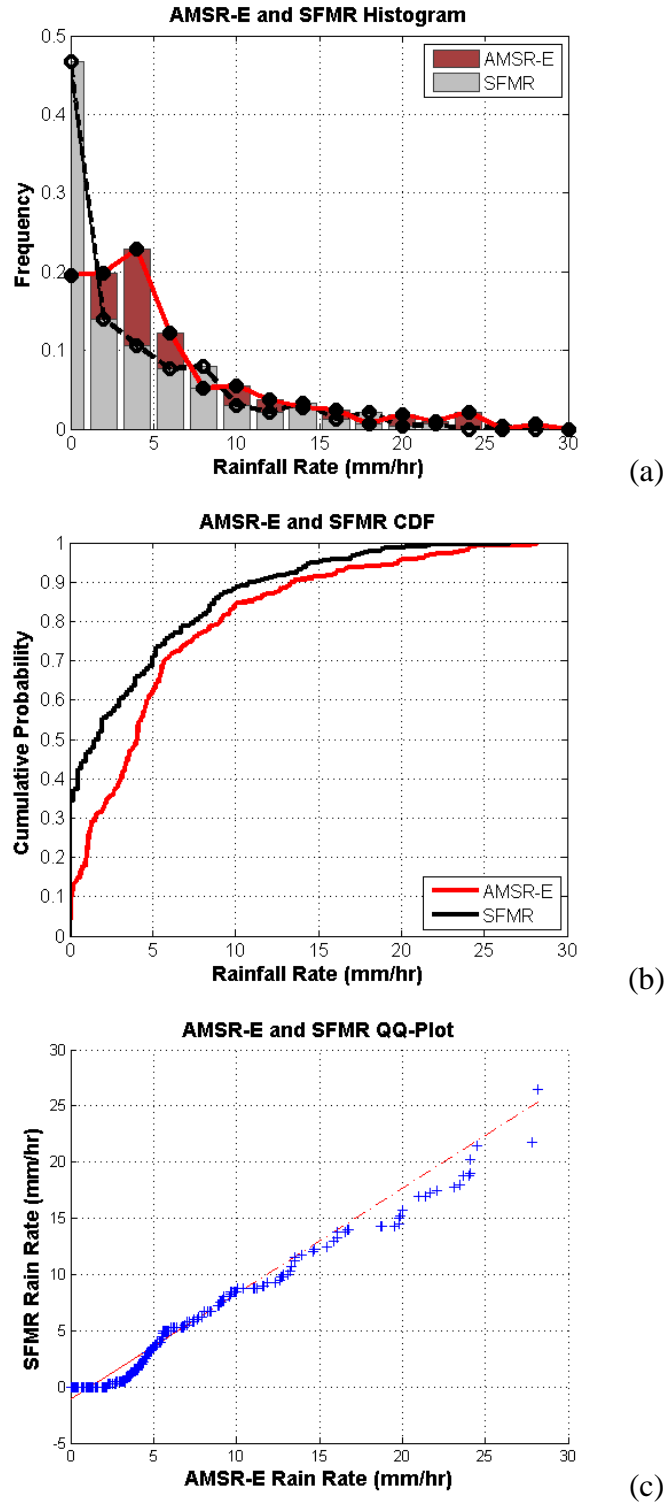
Figure 44.   Statistical characteristics of the SFMR and AMSR-E rain rates for TY Sinlaku on 09 Sep defined as (a) rain rate frequencies, (b) cumulative distribution functions, and (c) quantile-quantile plots.
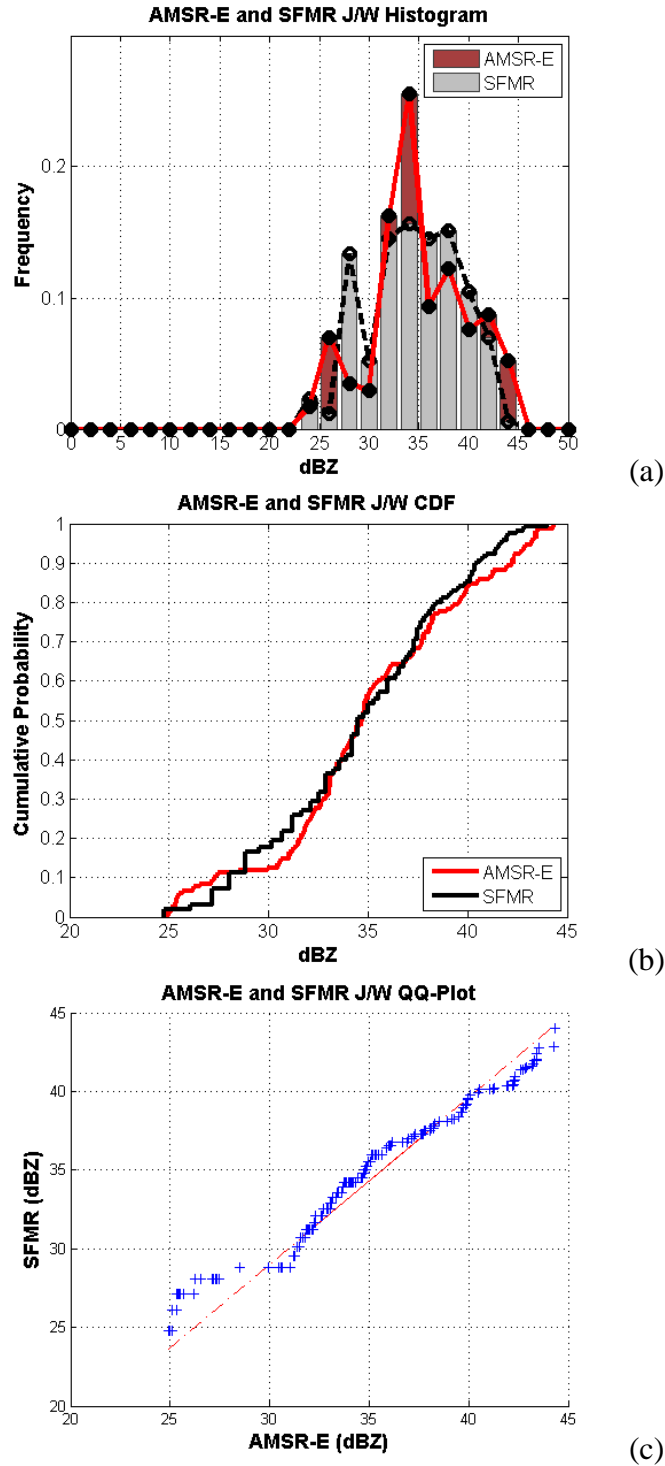
(a)

(b)

(c)

Figure 45.   Statistical characteristics of the SFMR and AMSR-E J/W dBZ for TY Sinlaku on 09 Sep defined as (a) rain rate frequencies, (b) cumulative distribution functions, and (c) quantile-quantile plots.

Figure 46.   Statistical characteristics of the SFMR and AMSR-E Carswell dBZ for TY
                Sinlaku on 09 Sep defined as (a) rain rate frequencies, (b) cumulative distribution
                functions, and (c) quantile-quantile plots.

Figure 47.   Statistical characteristics of the SFMR and AMSR-E rain rates for TY Jangmi on 27 Sep defined as (a) rain rate frequencies, (b) cumulative distribution functions, and (c) quantile-quantile plots.

(a)

(b)

(c)

Figure 48.   Statistical characteristics of the SFMR and AMSR-E J/W dBZ for TY Jangmi
on 27 Sep defined as (a) rain rate frequencies, (b) cumulative distribution
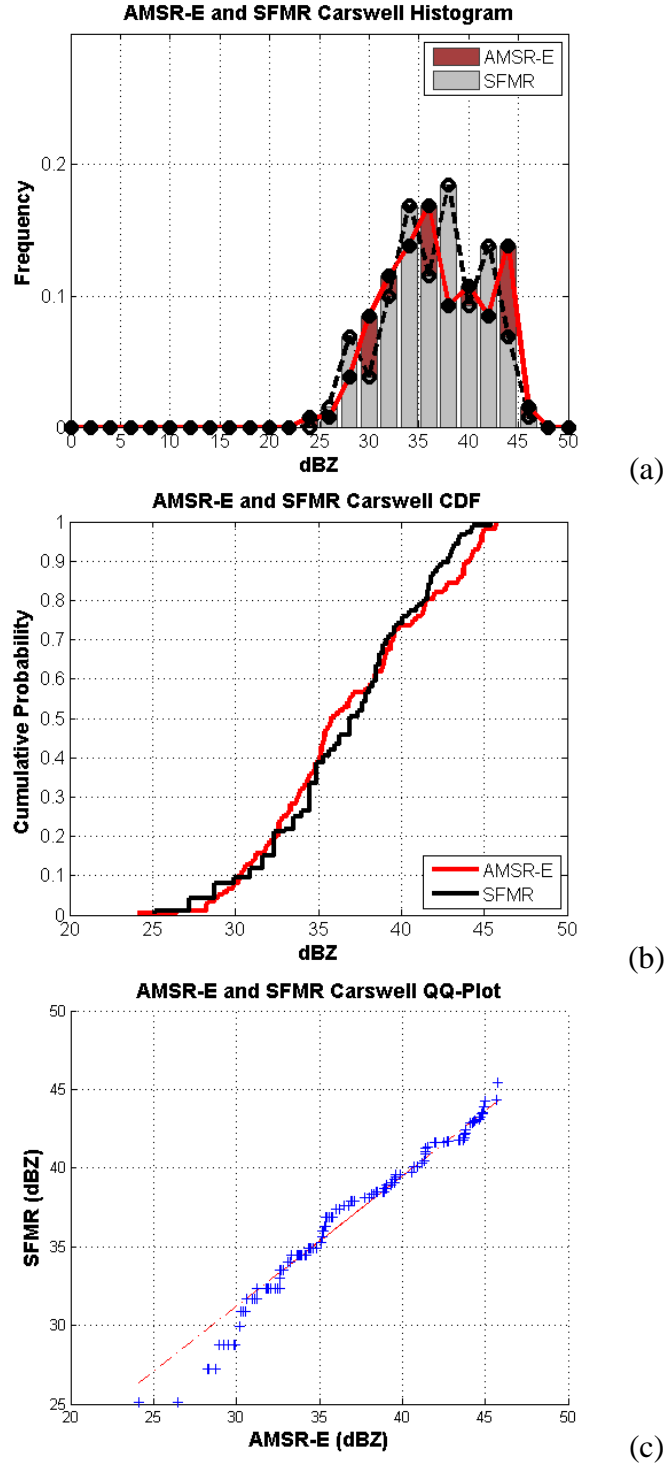functions, and (c) quantile-quantile plots.

(a)

(b)

(c)
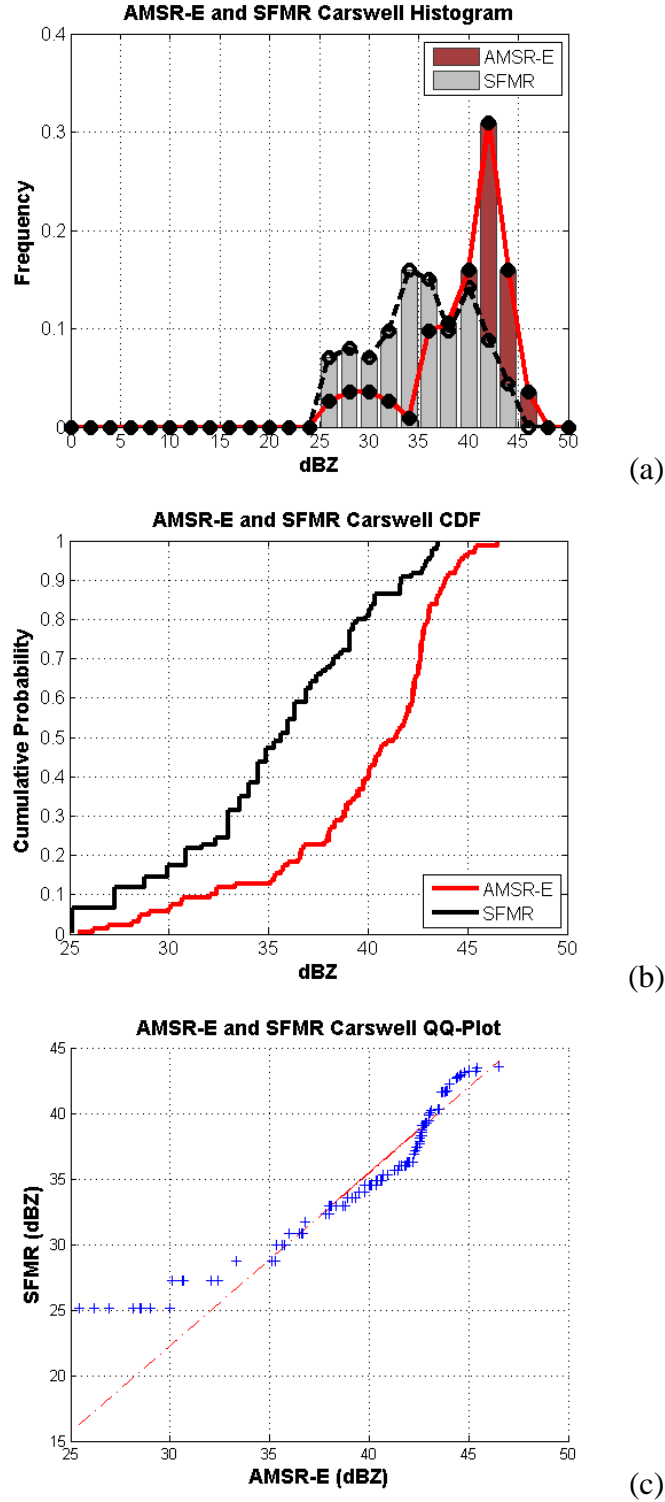
Figure 49.   Carswell Statistical characteristics of the SFMR and AMSR-E Carswell dBZ
for TY Jangmi on 27 Sep defined as (a) rain rate frequencies, (b) cumulative
distribution functions, and (c) quantile-quantile plots.

AMSR-E and SFMR Histogram

AMSR-E and SFMR CDF
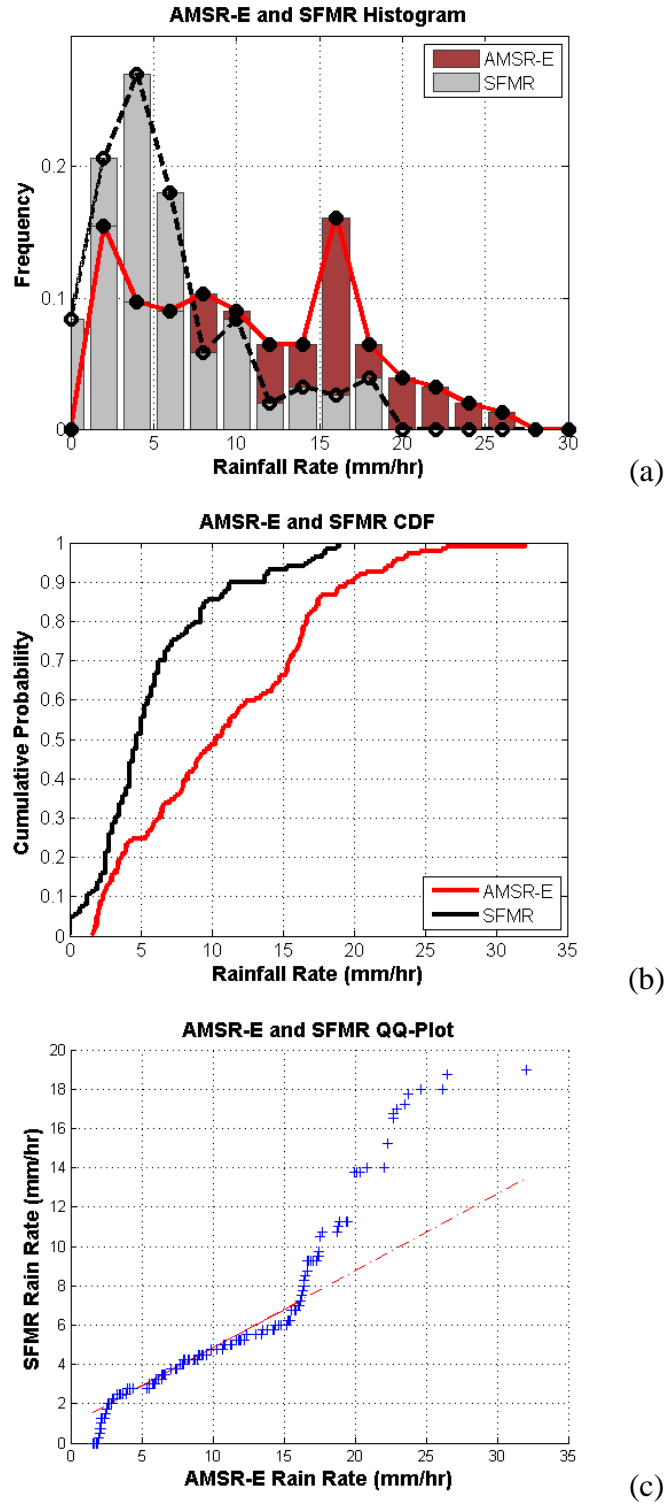
AMSR-E and SFMR QQ-Plot

(a)

(b)

(c)
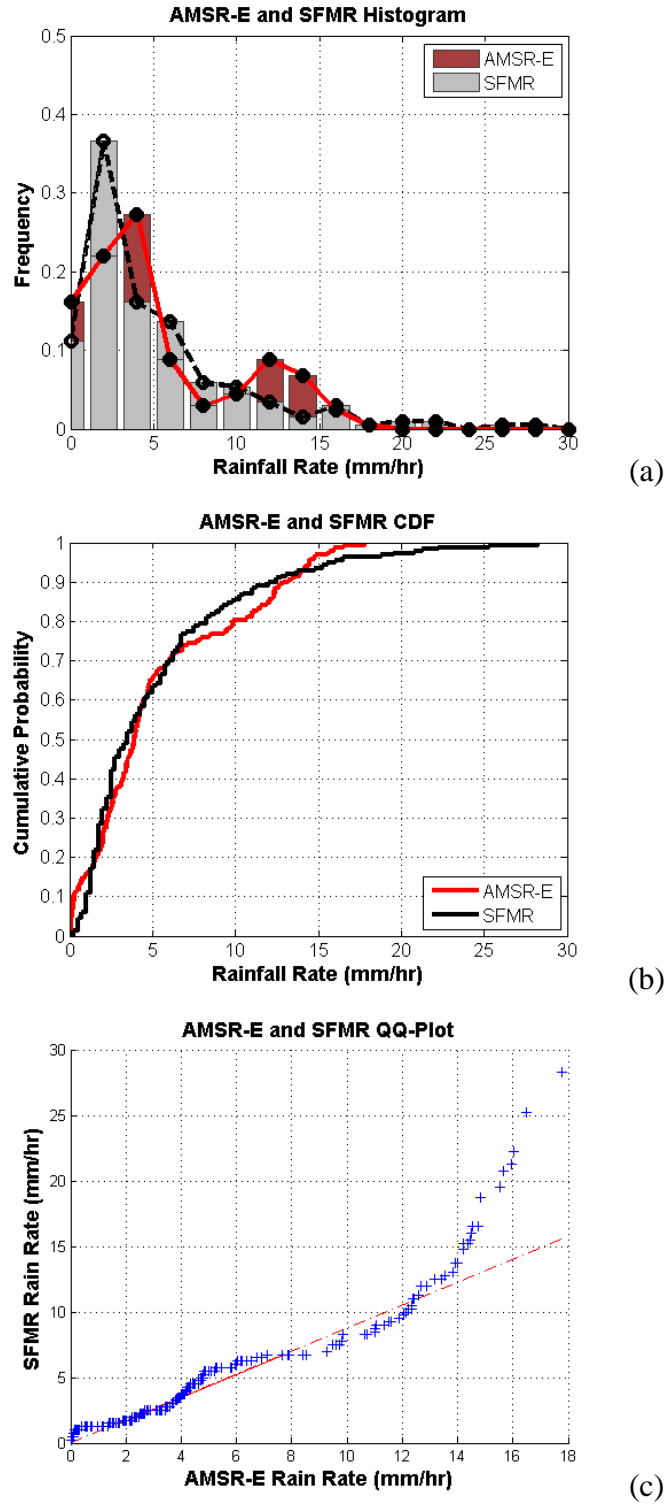
Figure 50.   Statistical characteristics of the SFMR and AMSR-E rain rates for TY Fanapi on 27 Sep defined as (a) rain rate frequencies, (b) cumulative distribution functions, and (c) quantile-quantile plots.
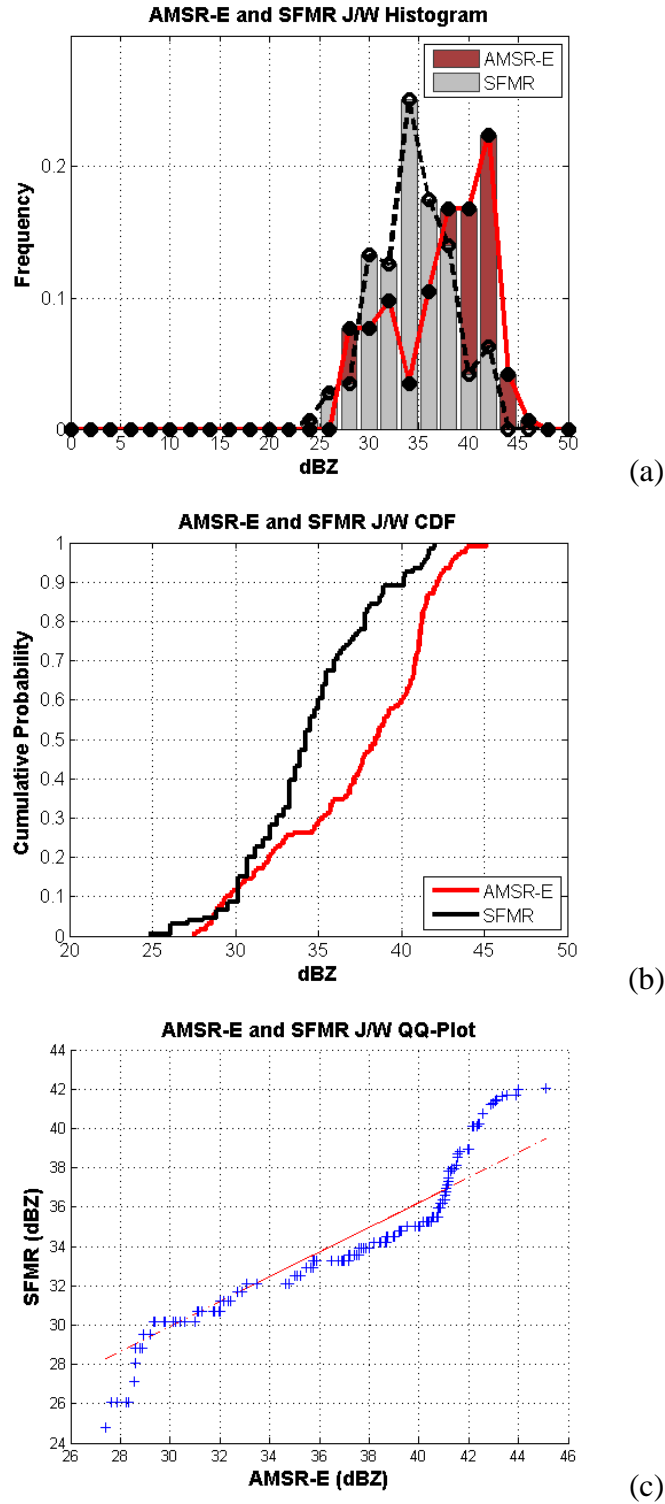
Figure 51.   Statistical characteristics of the SFMR and AMSR-E J/W dBZ for TY Fanapi on 17 Sep defined as (a) rain rate frequencies, (b) cumulative distribution functions, and (c) quantile-quantile plots.

83

AMSR-E and SFMR Carswell Histogram

(a)

AMSR-E and SFMR Carswell CDF

(b)

AMSR-E and SFMR Carswell QQ-Plot

(c)

Figure 52.   Statistical characteristics of the SFMR and AMSR-E Carswell dBZ for TY Fanapi on 17 Sep defined as (a) rain rate frequencies, (b) cumulative distribution functions, and (c) quantile-quantile plots.
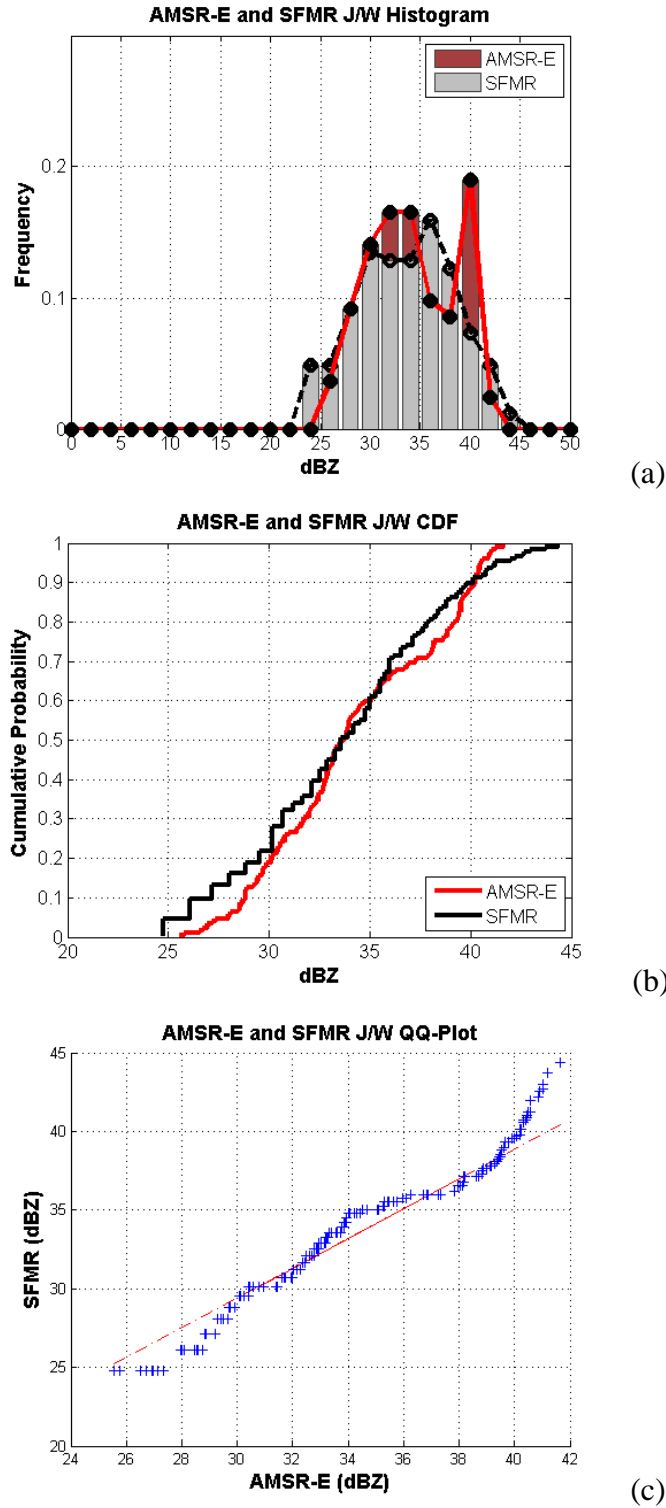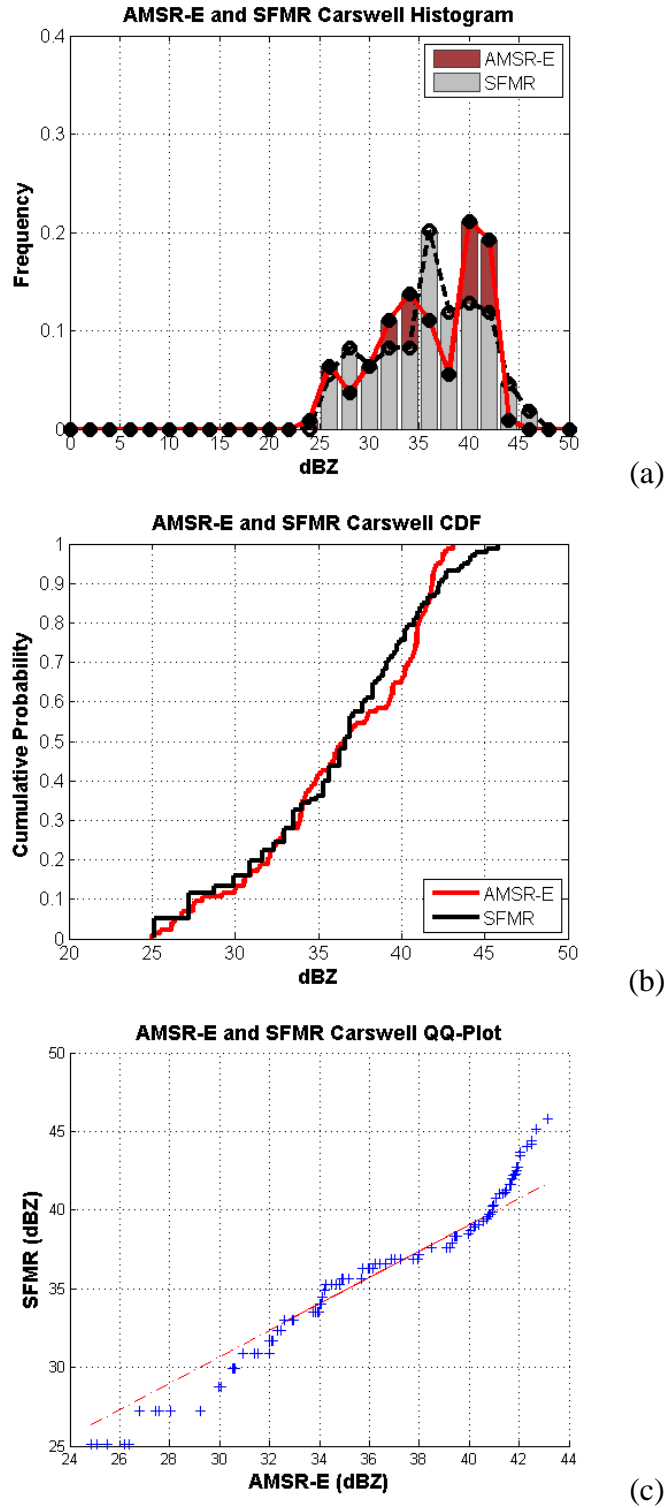
LIST OF REFERENCES

Durden, S. L., Z. S. Haddad, A. Kitiyakara, and F. K. Li, 1998: Effects of nonuniform beam filling on rainfall retrieval for the TRMM precipitation radar. *J. Atmos. Oceanic Technol.*, **15**, 635–646.

Elsberry, R. L., and P. A. Harr, 2008: Tropical cyclone structure (TCS08) field experiment: Science basis, observational platforms, and strategy. *Asian Pacific J. Atmos. Sci.*, **44**, 209–231.

Harrington, R. F., 1980: The development of a stepped frequency microwave radiometer and its application to remote sensing of the earth. NASA Tech. Rep. TM-81847, 169 pp.

Havel, P. J., 2009: Surface wind field analysis of tropical cyclones during TCS-08: Relative impacts of aircraft and remotely-sensed observations. M.S. thesis, Dept. of Meteorology, Naval Postgraduate School, 77 pp.

Iguchi, T., T. Kozu, R. Meneghini, J. Awaka, and K. Okamoto, 2000: Rain-profiling algorithm for the TRMM precipitation radar. *J. Appl. Meteor.*, **39**, 2038–2052.

Ikai, J., and K. Nakamura, 2003: Comparison of rain rates over the ocean derived from TRMM microwave imager and precipitation radar. *J. Atmos.Oceanic Technol.*, **20**, 1709–1726.

Japanese Aerospace Exploration Agency (JAXA), cited 2006: AMSR-E Data Users Handbook. [Available online at http://www.eorc.jaxa.jp/en/hatoyama/amsr-e/amsr-e_handbook_e.pdf.]

____, cited 2011: AMSR-E Sensor Information. [Available online at http://sharaku.eorc.jaxa.jp/AMSR/ov_amsre/sensor.html.]

____, cited 2012: AMSR/AMSR-E Typhoon Database. [Available online at http://sharaku.eorc.jaxa.jp/ADEOS2/TYPHOON_DB/index.shtml.]

Jiang, H., P. G. Black, E. J. Zipser, F. D. Marks, and E. W. Uhlhorn, 2006: Validation of rain-rate estimation in hurricanes from the stepped frequency microwave radiometer: Algorithm correction and error analysis. *J. Atmos. Sci.*, **63**, 252–267.

____, C. Liu, and E. J. Zipser, 2011: A TRMM-based tropical cyclone cloud and precipitation feature database. *J. Appl. Meteor. Climatol.*, **50**, 1255–1274.

Jin, K-W., S-W. Hong, R. Weitz, and T. Wilheit, 2005: Improved physically-based AMSR-E oceanic rainfall algorithm. *IEEE Trans. Geosci. Remote Sens.*, **45**, 3462–3465.

Joint Typhoon Warning Center (JTWC), cited 2008: JTWC Annual Tropical Cyclone Report for 2008. [Available online at http://www.usno.navy.mil/NOOC/nmfc-ph/RSS/jtwc/atcr/2008atcr.pdf.]

____, cited 2010: JTWC Annual Tropical Cyclone Report for 2010. [Available online at http://www.usno.navy.mil/NOOC/nmfc-ph/RSS/jtwc/atcr/2010atcr.pdf.]

____, cited 2012: JTWC Tropical Cyclone Best Track Data Site. [Available online at http://www.usno.navy.mil/NOOC/nmfc-ph/RSS/jtwc/best_tracks.]

Jorgensen, D. P., and P. T. Willis, 1982: A Z-R relationship for hurricanes. *J. Appl. Meteor.*, **21**, 356–366.

National Aeronautics and Space Administration (NASA), cited 2011a: NASA TMI Information. [Available online at http://pmm.nasa.gov/TRMM/TMI.]

____, cited 2011b: GES DISC TRMM Information. [Available online at http://disc.sci.gsfc.nasa.gov/precipitation/documentation/TRMM_README.]

____, cited 2011c: NASA PR Information. [Available online at http://pmm.nasa.gov/TRMM/PR]

____, cited 2011d: NASA Aqua Project Science Information. [Available online at http://aqua.nasa.gov/index.php.]

National Hurricane Center (NHC), cited 2011: NHC main website. [Available online at http://www.nhc.noaa.gov/aboutintro.shtml.]

Naval Research Laboratory (NRL), cited 2011: NRL Tropical Cyclone SSM/I Information. [Available online at http://www.nrlmry.navy.mil/sat_training/tropical_cyclones/ssmi/85h/index.html.]

Naval Postgraduate School (NPS), cited 2008: T-PARC main website. [Available online at http://met.nps.edu/~tparc/index.html.]

Olsen R. L., D. V. Rogers, and D. B. Hodge, 1978: The aR^b relation in the calculation of rain attenuation. *IEEE Trans. Antennas Propagat.*, **AP-26**, 318–329.

Pun, I., Y. Chang, I. I. Lin, T. Y. Tang, and R. C. Lien, 2011: Typhoon-ocean interaction in the western North Pacific, Part 2. *Oceanography*, **24**, 32–41.

Radar Operations Center (ROC), cited 2008: WSR-88D TC Op Plan. [Available online at http://www.ofcm.gov/nhop/wsr-88d/nat_trop_cyc_wsr-88d_ops_plan_B9.pdf.]

Uhlhorn, E. W., and P. G. Black, 2003: Verification of remotely sensed sea surface winds in hurricanes. *J. Atmos. Oceanic Technol.*, **20**, 99–116.

____, P. G. Black, J. L. Franklin, M. Goodberlet, J. Carswell, and A. S.   Goldstein, 2007: Hurricane surface wind measurements from an operational   stepped frequency microwave radiometer. *Mon. Wea. Rev.*, **135**, 3070–3085.

Wilheit, T. T., C. D. Kummerow, and R. Ferraro, 2003: Rainfall algorithms for AMSR-E. *IEEE Trans. Geosci. Remote Sens.*, **41**, 204–214.

THIS PAGE INTENTIONALLY LEFT BLANK

INITIAL DISTRIBUTION LIST

1. Defense Technical Information Center
    Ft. Belvoir, Virginia

2. Dudley Knox Library
    Naval Postgraduate School
    Monterey, California

3. Dr. Patrick A. Harr
    Naval Postgraduate School
    Monterey, California

4. Dr. Russell L. Elsberry
    Naval Postgraduate School
    Monterey, California

5. Dr. Peter Black
    Naval Research Laboratory
    Monterey, California

6. Mr. Jeffrey Hawkins
    Naval Research Laboratory
    Monterey, California

7. Capt. Ryan S. Willis
    United States Air Force